Università degli Studi di Bologna

Facoltà di Scienze Matematiche Fisiche e Naturali
Dottorato di Ricerca in Fisica, **XV** Ciclo

Automatic scanning of emulsion films for the OPERA experiment

Gabriele Sirri

Advisors:
Prof. **Giorgio Giacomelli**
Dr. **Gianni Mandrioli**

PhD Coordinator:
Prof. **Giovanni Venturi**

Bologna, 2003

Contents

Introduction **1**

1 Neutrino oscillations **3**
1.1 A brief history of neutrinos . . . 3
1.2 Neutrino in the Standard Model . . . 5
1.3 Neutrino mixing . . . 7
1.4 Neutrino oscillations . . . 10
1.5 Neutrino oscillations in matter . . . 12
1.6 Neutrino oscillation phenomenology . . . 14

2 Experimental status **17**
2.1 Direct measurements of neutrino mass . . . 17
2.2 The solar neutrino problem . . . 18
2.3 Atmospheric neutrino oscillation experiments . . . 21
2.4 Long-baseline oscillation experiments . . . 27
2.5 Oscillation experiments at high Δm^2 . . . 29

3 The OPERA Experiment **31**
3.1 Introduction . . . 31
3.2 The CNGS neutrino beam . . . 32
3.3 Detector structure and operation . . . 34
3.3.1 Target . . . 34
3.3.2 Electronic detectors in the target modules . . . 36
3.3.3 Muon spectrometers . . . 38
3.4 Physics performances . . . 39
3.4.1 τ detection . . . 39
3.5 Efficiencies, background and sensitivity of the experiment . . . 42

4 Nuclear Emulsions **45**
4.1 Basic properties of emulsions . . . 45
4.2 The photographic processes . . . 46
4.2.1 Formation of the latent image . . . 46
4.2.2 Development . . . 47
4.2.3 Fixation . . . 48
4.3 Processed emulsion . . . 49
4.3.1 The "fog" . . . 49
4.3.2 Track visibility . . . 49
4.3.3 Shrinkage factor . . . 50
4.3.4 Distortions . . . 50
4.4 OPERA Emulsion films . . . 52

5 The automatic system for emulsion scanning **59**
5.1 Introduction . . . 59
5.2 The principle of automatic scanning of emulsions . . . 60
5.3 Image handling . . . 62
5.4 Track Recognition . . . 65
5.5 Track Postprocessing . . . 67
5.6 The prototype in Bologna . . . 68

6 The set-up of the optical system **73**
6.1 The requirements for scanning emulsion sheets . . . 73
6.1.1 Objective . . . 73
6.1.2 Substage condenser . . . 75
6.2 The design choice . . . 76
6.2.1 Magnifying Power . . . 77
6.2.2 Other specifications of the objective . . . 77
6.2.3 The Camera . . . 78
6.2.4 The condenser . . . 79
6.2.5 Illumination . . . 79
6.2.6 The light source . . . 80
6.3 Tests of the quality of optics . . . 80
6.3.1 Field curvature and geometrical distortions . . . 80
6.3.2 Chromatic aberrations . . . 81
6.3.3 Achromatic aberrations . . . 82
6.3.4 Condenser and diffuse light inside the optical tube . . . 83

6.4 Evaluation of the magnification error 83
6.5 The alignment of the optical axis 84

7 Preliminary results **87**
7.1 The test beam setup 87
7.2 DAQ software 89
7.3 The SySal acquisition software 89
7.4 Quality tests of the scanning system 91
7.4.1 Mechanical tests 91
7.4.2 Illumination checks 92
7.4.3 Acquisition uniformity 95
7.4.4 Track reconstruction 96

Conclusions **105**

Bibliography **107**

Introduction

In recent years, neutrino physics, and in particular neutrino oscillations, have become an important topic in the field of high energy physics. The existence of neutrino oscillations would require an extension of the subnuclear phenomena description beyond the Standard Model of the electroweak and strong interactions. Interest in this fields has been revived by several experimental results, which strongly support the neutrino oscillation hypothesis.

Many experiments studying solar neutrinos with different detection techniques measured solar electron neutrino fluxes significantly lower than the predictions. Moreover, results from the SNO experiment gave a model independent strong indication of the presence of ν_μ and ν_τ in the flux of solar neutrinos on Earth.

The Soudan2, MACRO and SuperKamiokande experiments studying atmospheric neutrinos, produced in the decay of secondary particles created in the interactions of primary cosmic rays with the nuclei of the Earth atmosphere, found strong indications for muon neutrino oscillations.

A definitive demonstration that the observed atmospheric ν_μ anomaly is due to ν_μ oscillations would require an appearance experiment. The OPERA experiment in the CNGS project (CERN Neutrinos to Gran Sasso) will search for ν_τ appearance at a distance of 732 km in a pure ν_μ beam from the 450 GeV SPS at CERN to the Gran Sasso Laboratory.

OPERA should directly measure the τ kink in space, as determined by track segments measured with very high precision using nuclear emulsions. The emulsion detector, consists of two 42 μm emulsion layers coated on each side of a 200 μm plastic foil and are arranged in a lead-emulsion sandwich structure (the so-called brick); this technique is quite similar to that used in the first detection of ν_τ interactions by the DONUT experiment at Fermilab.

Emulsions have excellent spatial resolution, providing an angle measurement accuracy of about 4 mrad. This allows to detect kink angles in the

range 20÷500 mrad with an efficiency above 80%.

Because of the very large emulsion load of the OPERA experiment, an automatic scanning system is required for finding and measure tracks coming from neutrino interactions.

A microscope for automatic emulsion scanning consists of a computer driven mechanical stage, appropriate optical system, a camera and its associated readout.

A prototype of the automatic scanning system has been realized at the Bologna Laboratory.

In order to measure with high accuracy and high speed, very strict constraints must be satisfied in term of mechanical precisions, camera speed, image processing power. In particular, the quality of the set-up of the optical system is critical.

Checks of mechanical performance and preliminary results, using emulsion sheets exposed at CERN pion beam, are presented.

In this thesis I shall briefly discuss neutrino oscillations in Chap. 1 e 2, the OPERA experiment in Chap. 3 and the emulsion technique in Chap.4. In Chap. 5 and 6 will be described in detail the automatic scanning system and its optical components. Preliminary results are discussed in Chap. 7.

Chapter 1

Neutrino oscillations

1.1 A brief history of neutrinos

The existence of neutrinos was proposed by W. Pauli in 1930 as an attempt to explain the continuous spectrum of β-decay and the problems of spin and statistics of nuclei : "*... I have hit upon a desperate remedy to save the exchange theorem*[1] *of statistics and the law of conservation of energy. Namely, the possibility that there could exist in the nuclei electrically neutral particles, that I wish to call neutrons, which have spin 1/2 and obey the exclusion principle and which further differ from light quanta in that they do not travel with the velocity of light. The mass of the neutrons should be of the same order of magnitude as the electron mass and in any event not larger than 0.01 proton masses...*" [1].

In 1932 Chadwick discovered the neutron and solved the problem of spin and statistics of the nuclei; but neutrons are heavy and could not correspond to the particle imagined by Pauli. In 1933-34 Fermi introduced the name *neutrino* in his four-fermion theory of β-decay, formulated in analogy with QED.

Until the end of the forties, physicists tried to measure the recoil of the nucleus during its beta decay. All the measurements were compatible with the hypothesis of only one neutrino emitted with the electron. It became clear that a very abundant source of neutrinos and a very sensitive and huge detector were needed to detect the neutrinos.

[1] That reads: exclusion principle (Fermi statistics) and half-integer spin for an odd number of particles; Bose statistics and integer spin for an even number of particles.

The experimental discovery of the neutrino is due to Cowan and Reines in 1956 [2]; the experiment consisted in a target made of around 400 liters of a mixture of water and cadmium chloride: the electron anti-neutrinos coming from the nuclear reactor interact with protons of the target matter, giving a positron and a neutron (inverse β decay) $\overline{\nu}_e + p \rightarrow n + e^+$.

Following the experimental discovery of the neutrino, neutrinos were first shown to always have negative helicity (i.e. the spin and momentum are aligned in opposite directions) by measuring the helicity of gamma-rays produced in the radioactive decay of Europium-152 (knowing the nuclear spin states of the parent and daughter nuclei in the decay, the helicities of the photon and of the neutrino must match).

Later it was established that there were two different types of neutrino, one associated with the electron and one with the muon. A muon neutrino beam was made using the $\pi \rightarrow \mu\nu_\mu$ decays. The ν_μ interacted in a target producing muons and not electrons $\nu_\mu p \rightarrow n\mu^-$[3].

These experiments, along with many others, have experimentally established that ν_e and ν_μ are the neutral partners of the charged leptons (muon and lepton) and helped to shape our understanding of weak interactions in the Standard Model.

In e^+e^- collisions at SLAC was later found evidence for a third type of lepton τ^- to which was associated a third neutrino ν_τ.

During the sixties and seventies, electron and muon neutrinos of high energy were used to probe the composition of nucleons. The experiments gave evidence for quarks and established their properties.

In 1970, Glashow, Illiopoulos and Maiani made the hypothesis of the existence of a second quark family, which should correspond to the second family of leptons; this hypothesis was confirmed by american experiments at the end 1974.

In 1973 neutral currents (neutrino interaction with matter where neutrino is not transformed into an other particle like muon or electron) were discovered at CERN and confirmed at Fermilab.

In 1977 the b quark, that is one quark of the third quarks family, was discovered at Fermilab, almost at the same time that Martin Perl discovered the τ lepton at SLAC. The corresponding neutrino ν_τ was finally observed experimentally only in 2001 at Fermilab by the E872 experiment (a.k.a. DONUT).

A complete knowledge of weak interactions came after the discoveries of the W and the Z bosons in 1983; in 1989 the study of the Z boson

width allowed to show that only three lepton families (and then three type of neutrinos) exist.

Precision confirmations of the validity of the Standard Model at low and high energy were experimentally given in the 90's at LEP. Even so, the high energy physics community started turning towards the search for physics beyond the Standard Model, in particular for a non zero neutrino mass and on neutrino oscillations.

1.2 Neutrino in the Standard Model

The Glashow-Weinberg-Salam theory of the electroweak interaction, combined with Quantum Chromo-Dynamics (QCD) is now called the Standard Model (SM) of particle physics, it is one of the greatest achievements of the 20^{th} century [4].

Quarks

$-\frac{1}{3}$ **d** 1.5−4.5 MeV	$-\frac{1}{3}$ **s** 80−155 MeV	$-\frac{1}{3}$ **b** 4.0−4.5 GeV
$+\frac{2}{3}$ **u** 5−8.5 MeV	$+\frac{2}{3}$ **c** 1.0−1.4 GeV	$+\frac{2}{3}$ **t** 174±5 GeV

Gauge bosons

$g_{em} = 0.30$ 0 γ 0 eV	g= 0.65 ±1 **W** 80.4 GeV
$g_s = 1.22$ 0 **g** 0 eV	g'= 0.36 0 **Z** 91.2 GeV

Leptons

−1 **e** 0.511 MeV	−1 μ 105.66 MeV	−1 τ 1.777 GeV
0 ν_e <3 eV	0 ν_μ <0.19 MeV	0 ν_τ <18.2 MeV

Higgs

0 **H** >114.3 MeV

Table 1.1: Fundamental fermions and gauge bosons the Standard Model. Particle masses and charges are shown. The particles are grouped into the fundamental fermions (quarks and leptons) and fundamental bosons; the fermions are further grouped into three families.

The particle content, properties and couplings are shown in Tab. 1.1. The fundamental fermions (quarks and leptons) are grouped into three generations of increasing mass. Particle interactions in the Standard Model are mediated by gauge bosons: the photon for electromagnetic interaction, the $W^{\pm}$ and Z^0 bosons for the weak interaction and gluons for the strong force.

All the prediction of the SM have been confirmed by many precise experiments: the charmed particles, the b and t quarks, the weak neutral current, the mass of the vector bosons $W^{\pm}$ and Z^0 are all well known.

However, the SM cannot be considered the final theory of elementary particles: in this theory gravity is not included, more than 20 arbitrary fundamental parameters (masses of quarks and leptons, coupling constants, ...) remain to be explained, it lacks any explanations of why in nature there exist three generations of quarks and leptons, etc . More general models have been proposed (GUT, Supersymmetry, Superstrings, ...); many experimental searches for new physics beyond the SM have been performed. At present the only new physics beyond the SM was found by neutrino oscillation experiments.

In the SM, neutrinos are massless, electrically neutral, spin 1/2 particles and do not couple to gluons. They only couple to other Standard Model particles via weak interactions mediated by $\mathrm{W}^{\pm}$ and Z^0 bosons.

There are three species (or flavours) of light neutrinos, ν_e, ν_μ and ν_τ, which are left handed; their antiparticles $\bar{\nu}_e$, $\bar{\nu}_\mu$ and $\bar{\nu}_\tau$ are right handed. Electron-type neutrinos and antineutrinos are produced in nuclear $\beta^{\pm}$ decay, in particular in the neutron decay $n \to p + e^- + \bar{\nu}_e$. They are also produced in muon decays $\mu^{\pm} \to e^{\pm} + \bar{\nu}_\mu(\nu_\mu) + \nu_e(\bar{\nu}_e)$, and as a subdominant mode, in pion decays $\pi^{\pm} \to e^{\pm} + \nu_e(\bar{\nu}_e)$ and in some other decays and reactions. The elementary processes responsible for nuclear beta decays or pion decays are actually the quark transitions $u \to d + e^+ + \nu_e$ and $d \to u + e^- + \bar{\nu}_e$.

Muon neutrinos and antineutrinos are produced in muon decays $\mu \to \nu_\mu e \nu_e$, pion decays $\pi^{\pm} \to \mu^{\pm} + \nu_\mu(\bar{\nu}_\mu)$ and some other processes. Neutrinos of the third type, tau, are produced in $\tau^{\pm}$ decays. They have recently been experimentally detected by the DONUT experiment at Fermilab.

Neutrinos of each flavour participate in reactions in which the charged lepton of the corresponding type are involved; these reactions are mediated by $W^{\pm}$ bosons. Thus, these so-called charged current reactions involve the processes $W^{\pm} \to l_a^{\pm} + \nu_a(\bar{\nu}_a)$ where $a = e,\ \mu$ or τ, or related processes. Neutrinos can also participate in neutral current reactions mediated by Z^0 bosons; these are elastic or quasielastic scattering processes and decays $Z^0 \to \nu_a \bar{\nu}_a$.

Neutrinos from the Z^0 decays are not detected, and therefore the difference between the measured total width of the Z^0 boson and the sum of its partial widths of decay into quarks and charged leptons, the so-called invisi-

ble width, $\Gamma_{inv} = \Gamma_{tot} - \Gamma_{vis} = 498 \pm 4.2$ MeV, should be due to the decay into $\nu\bar{\nu}$ pairs. Taking into account that the partial width of Z^0 decay into one $\nu\bar{\nu}$ pair $\Gamma_{\nu\bar{\nu}} = 166.9$ MeV one finds the number of the light active neutrino species [5]:

$$N_\nu = \frac{\Gamma_{inv}}{\Gamma_{\nu\bar{\nu}}} = 2.994 \pm 0.012 \tag{1.1}$$

in a very good agreement with the existence of the three neutrino flavours. There are also indirect limits on the number of light ($m < 1$ MeV) neutrino species (including possible electroweak singlet, i.e. "sterile" neutrinos ν_s) coming from big bang nucleosynthesis. The number of neutrino species in equilibrium with the rest of the universe at the nucleosynthesis epoch is

$$N_\nu < 3.3 \tag{1.2}$$

though this limit is less reliable than the laboratory one (1.1), and probably four neutrino species can still be tolerated [6]. In view of (1.1), the additional neutrino species, if exist, must be a sterile neutrino ν_s.

1.3 Neutrino mixing

The recent atmospheric neutrino data from SuperKamiokade, MACRO and Soudan-2 and the data on solar neutrinos from SuperKamiokande and SNO provide strong evidence for neutrino oscillations which can take place only if neutrinos are massive and neutrino mixing is present.[2]

According to the neutrino mixing hypothesis [7, 11] neutrino masses are different from zero and fields of massive neutrinos ν_i enter into the CC and the NC Lagrangians

$$\mathcal{L}_I^{CC} = -\frac{g}{2\sqrt{2}} j_\alpha^{CC} W^\alpha + \text{h.c.} \qquad \mathcal{L}_I^{NC} = -\frac{g}{2\cos\theta_W} j_\alpha^{NC} Z^\alpha \tag{1.3}$$

where g is the electroweak interaction constant, θ_W is the Weinberg angle, W^α and Z^α are the fields of $W^\pm$ and Z^0 vector bosons and j_α^{CC} and j_α^{NC} are the leptonic charged and neutral currents.

[2] The atmospheric neutrino data are consistent with $\Delta m^2 = m_3^2 - m_2^2 = 2.5 \cdot 10^{-3}$ eV^2 and large mixing.

The massive neutrinos enter in the Eq. 1.3 in the mixed form (L and R in the index mean left-handed and right-handed, respectively)

$$\nu_{lL} = \sum_i U_{li}\nu_{iL} \tag{1.4}$$

where ν_l is a flavour field, ν_i is the field of a neutrino with mass m_i and U is the unitary mixing matrix, also known as the Maki-Nakagawa-Sakata (MNS) matrix [11], the leptonic analogue of the CKM matrix [5] for the quark sector. Eq. 1.4 leads to a violation of lepton numbers, but usually not of the total lepton number. If neutrino masses are different from zero, there is a neutrino mass term in the total Lagrangian. The structure of the mass term depends on the mechanism of neutrino mass generation. Only left-handed neutrino fields ν_{lL} enter into the Lagrangian of the weak interaction (Eq. 1.3). In the case of massive neutrinos, both ν_{lL} and singlet ν_{lR} fields can enter in the neutrino mass term. If ν_{lL} and ν_{lR} enter in such a form that the total lepton number L is conserved, the fields of massive neutrinos are four-component Dirac fields and neutrino ν_i and antineutrino $\bar{\nu}_i$ have opposite lepton numbers. The corresponding mass term is called the Dirac mass term. The number of the massive neutrinos in the case of the standard Dirac mass term is equal to the number of neutrinos. The Dirac mass term could be generated by the Standard Higgs mechanism with a Higgs doublet.

If the lepton number is not conserved, only left-handed components ν_{lL} can enter into the neutrino mass term. The corresponding mass term is called the Majorana mass term. It is a product of left-handed components ν_{lL} and right- handed components $(\nu_{lL})^c$, determined by the relation $(\nu_{lL})^c = C\bar{\nu}_{lL}^T$ where C is the matrix of the charge conjugation that satisfies the conditions $C\gamma_\alpha^T C^{-1} = -\gamma_\alpha$ and $C^T = -C$.

In the case of the Majorana mass term, the fields ν_i in Eq. 1.4 are two-component Majorana fields that satisfy the condition

$$\nu_i = \nu_i^c \tag{1.5}$$

The Eq. 1.5 means that neutrinos and antineutrinos, quanta of the Majorana field ν_i, are identical particles. The number of the massive neutrinos in the case of the Majorana mass term is equal to three. The Majorana mass term requires a mechanism beyond the Standard Model for neutrino mass generation with Higgs triplets.

In the most general case both ν_{lL} and ν_{lR} fields enter into the mass term and there are no conserved lepton numbers (the Dirac and Majorana mass term). As the lepton numbers are not conserved, there is no possibility to distinguish neutrinos and antineutrinos and fields of neutrinos with definite masses ν_i in the case of the Dirac and Majorana mass term are two-component Majorana fields. If three left-handed fields ν_{lL} and three right-handed fields ν_{lR} enter into the mass term, the number of massive Majorana neutrinos is equal to 6. For the mixing, we have

$$\nu_{lL} = \sum_{i=1}^{6} U_{li}\nu_{iL} \qquad (l = e, \mu, \tau)$$

and

$$(\nu_{lR})^c = \sum_{i=1}^{6} U_{li}\nu_{iL}$$

where U is the 6x6 unitary matrix and the fields ν_i satisfy the Eq. 1.5.

In the framework of the Dirac and Majorana mass terms, there is a mechanism of neutrino mass generation, the so called *see-saw mechanism* [12]. This mechanism is based on the assumption that the lepton number is violated by the right-handed Majorana mass term at the scale M ($\sim$ 300 GeV), which is much larger than the electroweak scale ($M_{EW} \simeq 80 \div 90$ GeV). In the see-saw case, in the mass spectrum of Majorana particles there are three light masses m_k (masses of neutrinos) and three heavy masses $M_k \simeq M$ (k = 1, 2, 3). Neutrino masses are connected with the masses of the heavy Majorana particles by the see-saw relation

$$m_k \simeq \frac{(m_k^f)^2}{M_k} \ll m_k^f$$

where m_k^f is the mass of lepton or quark in k-family. The see-saw mechanism connects the smallness of neutrino masses with respect to the masses of all other fundamental fermions with a new physics at a large energy scale.

The fields ν_{lR} do not enter into the Lagrangian of the standard electroweak interaction and are called *sterile*. The nature and the number of sterile fields depend on models. There could be singlet right-handed neutrino fields and also SUSY fields, and so on. Thus, in the most general case for the mixing

we have

$$\nu_{lL} = \sum_{i=1}^{3+n_s} U_{li}\nu_{iL} \qquad ; \nu_{sL} = \sum_{i=1}^{3+n_s} U_{si}\nu_{iL}$$

where n_s is the number of sterile fields and U is a $(3+n_s)\times(3+n_s)$ unitary matrix.

1.4 Neutrino oscillations

Neutrino oscillations are a quantum mechanical process where one type of neutrino changes into another type of neutrino due to different mass eigenstate combinations. For the phenomenon to take place, there needs to be mass eigenstates of different masses, and the 3-flavor types need to be different combinations of these mass eigenstates.

As an example consider the two flavor mixing of the ν_μ and ν_τ neutrinos in terms of neutrino mass eigenstates ν_2, ν_3 ,and the mixing angle θ:

$$\begin{pmatrix} \nu_\mu \\ \nu_\tau \end{pmatrix} = \begin{pmatrix} \cos\theta & \sin\theta \\ -\sin\theta & \cos\theta \end{pmatrix} \begin{pmatrix} \nu_2 \\ \nu_3 \end{pmatrix} \tag{1.6}$$

If we assume at $t = 0$, the neutrino is created as a muon neutrino ν_μ, then

$$|\psi(0)\rangle = |\nu(0)\rangle = -\sin\theta|\nu_2\rangle + \cos\theta|\nu_3\rangle \tag{1.7}$$

At a later time t, the two mass states will have propagated with different phases leading to a ν_e/ν_μ mixture:

$$\begin{aligned} |\psi(t)\rangle &= -\sin\theta e^{-iE_2t}|\nu_2\rangle + \cos\theta e^{-iE_3t}|\nu_3\rangle \\ &= (\cos^2\theta e^{-iE_2t} + \sin^2 e^{-iE_3t})|\nu_\mu\rangle \\ &\quad \sin\theta\cos\theta(e^{-iE_3t} - e^{-iE_2t})|\nu_\tau\rangle \end{aligned} \tag{1.8}$$

The oscillation probability for $\nu_\mu \to \nu_\tau$ is then given by

$$P_{osc} = |\langle\nu_e|\psi(t)\rangle|^2 = \frac{1}{2}\sin^2 2\theta\,[1 - \cos(E_3 - E_2)t] \tag{1.9}$$

For small masses, $E_2 = p + m_2^2/2p$ and $E_3 = p + m_3^2/2p$ and $(t/p) = L/E$, yielding:

$$\begin{aligned} P_{osc} &= \tfrac{1}{2}\sin^2 2\theta \left(1 \cos\left(\tfrac{(m_3^2 - m_2^2)L}{E}\right)\right) \\ &= \sin^2 2\theta \sin^2\left(1.27\Delta m_{23}^2(eV^2)\tfrac{L(\mathrm{m})}{E(\mathrm{GeV})}\right). \end{aligned} \tag{1.10}$$

The three generation mixing formalism uses a matrix similar to the quark CKM matrix called the MNS (Maki-Nakagawa-Sakata) matrix:

$$\begin{pmatrix} \nu_e \\ \nu_\mu \\ \nu_\tau \end{pmatrix} = U_{MNS} \begin{pmatrix} \nu_1 \\ \nu_2 \\ \nu_3 \end{pmatrix} \tag{1.11}$$

where U_{MNS} can be written as:

$$\begin{pmatrix} c_{12}c_{13} & s_{12}c_{13} & s_{13}e^{-i\delta} \\ -s_{12}c_{23} - c_{12}s_{23}s_{13}e^{i\delta} & c_{12}c_{23} - s_{12}s_{23}s_{13}e^{i\delta} & s_{23}c_{13} \\ s_{12}s_{23} - c_{12}s_{23}s_{13}e^{i\delta} & -c_{12}s_{23} - s_{12}c_{23}s_{13}e^{i\delta} & c_{23}c_{13} \end{pmatrix} \tag{1.12}$$

where c and s refer to the sines and cosines of the three mixing angles, θ_{12}, θ_{23}, θ_{13}; and δ is a complex phase associated with CP violation. With three generations, there are three Δm_{12}^2, Δm_{23}^2, and Δm_{13}^2, but only two are independent.

In the case of Majorana neutrino it is:

$$\begin{pmatrix} c_{12}c_{13} & s_{12}c_{13}e^{-i\delta_{12}} & s_{13}e^{-i\delta_{13}} \\ -s_{12}c_{23}e^{i\delta_{12}} - c_{12}s_{23}s_{13}e^{i(\delta_{13}+\delta_{23})} & c_{12}c_{23} - s_{12}s_{23}s_{13}e^{i(\delta_{23}+\delta_{13}-\delta_{12})} & s_{23}c_{13}e^{-i\delta_{23}} \\ s_{12}s_{23}e^{i(\delta_{13}+\delta_{23})} - c_{12}s_{23}s_{13}e^{i(\delta_{13}+\delta_{23})} & -c_{12}s_{23}e^{i\delta_{23}} - s_{12}c_{23}s_{13}e^{i(\delta_{13}-\delta_{12})} & c_{23}c_{13} \end{pmatrix} \tag{1.13}$$

It is not usually appreciated that for each Δm_{ij}^2 value, there can be oscillations among all the neutrino flavors, but with different combinations of mixing angles. For example, oscillations corresponding to the Δm_{23}^2 term include:

$$\begin{aligned} P(\nu_\mu \to \nu_\tau) &= \cos^4\theta_{13}\sin^2 2\theta_{23}\sin^2(1.27\Delta m_{23}^2 L/E) \\ P(\nu_\mu \to \nu_e) &= \sin^2\theta_{23}\sin^2 2\theta_{13}\sin^2(1.27\Delta m_{23}^2 L/E) \\ P(\nu_e \to \nu_\mu) &= \cos^2\theta_{23}\sin^2 2\theta_{13}\sin^2(1.27\Delta m_{23}^2 L/E) \end{aligned}$$

The measurements of CP violation in neutrino oscillations has been put forward as a prime future goal for the field, since it may give us a key to the source of neutrino mass and may also be important for understanding the baryon-antibaryon asymmetry in the universe. But seeing CP violating effects in neutrino oscillations is going to be very difficult. The reason is that one can only observe these effects through an experiment that is sensitive to oscillations involving at least three different types of neutrinos. One possibility is comparing the probability for $\nu_\mu \to \nu_e$ versus $\overline{\nu}_\mu \to \overline{\nu}_e$ oscillations.

$$P(\nu_\mu \to \nu_e) - P(\overline{\nu}_\mu \to \overline{\nu}_e) = 4\mathrm{Im}(U_{\mu 1}U_{e1}^* U_{\mu 3}^* U_{e3})(S_{12} + s_{23} + s_{31}) \quad (1.14)$$

where U_{ij} are the elements of the MNS matrix ($4\mathrm{Im}(U_{\mu 1}U_{e1}^* U_{\mu 3}^* U_{e3}) = 16 c_{12}c_{13}^2 c_{23} s_{12} s_{13} s_{23}(\sin\delta)$), and $s_{ij} = \sin \Delta m_{ij}^2 L/2E$). (Note: in this formula the s_{ij} terms are not squared but add linearly.) To have sensitivity to this CP violating difference, the combination of mixing angles must be finite and all the terms (s_{12}, s_{23}, s_{31}) must not be small (or effectively one would have two component oscillations). For example, if $s_{12} \approx 0$ then $s_{23} \approx s_{31}$ and the sum $s_{12} + s_{23} + s_{31} \approx 0$. This means that an experiment must be sensitive to the lowest Δm^2 value, which currently would be associated with solar neutrino oscillations.

1.5 Neutrino oscillations in matter

Travelling through matter, neutrinos of all flavours can have neutral-current interactions with the protons, neutrons and electrons of the medium. However only electron neutrinos can interact with the electrons, through a coherent forward scattering via a W boson exchange. The consequence of this asymmetry between neutrino flavours is known as the Mikheyev-Smirnov-Wolfenstein (MSW) effect [13, 14].

At low neutrino energies, for electron, muon and tau neutrinos traversing an electrically neutral and unpolarized medium, the matter-induced potentials are given by:

$$\begin{aligned} V_e &= \sqrt{2}G_F \quad (N_e - N_n/2) \\ V_\nu = V_\tau &= -\sqrt{2}G_F \quad N_n/2 \end{aligned} \quad (1.15)$$

Where G_F is the Fermi constant, N_e and N_n are the electron and the neutron densities in the medium, respectively. For antineutrinos the potentials

have opposite signs. The weak potential in matter produces a phase shift that can modify the neutrino oscillation probability if the oscillating neutrinos have different interactions with matter. Therefore the matter effect could allow to discriminate between different oscillation channels.

According to Eq. 1.15, matter effects in the Earth could be important for $\nu_\mu \leftrightarrow \nu_e$ and for $\nu_\mu \leftrightarrow \nu_{sterile}$ oscillations, while for $\nu_\mu \leftrightarrow \nu_\tau$ oscillations there is no matter effect.

In the simplest case of constant matter density and two-flavour oscillation, for example μ and e, the mass ($|\nu_1^M\rangle$ and $|\nu_2^M\rangle$) and flavour ($|\nu_e\rangle$ and $|\nu_\mu\rangle$) states are connected by a two-dimensional rotation. The relation between the two bases is given by:

$$\begin{array}{rcrr} |\nu_1^M\rangle & = & \cos\theta_M|\nu_e\rangle & +\sin\theta_M|\nu_\mu\rangle \\ |\nu_2^M\rangle & = & -\sin\theta_M|\nu_e\rangle & +\cos\theta_M|\nu_\mu\rangle \end{array} \tag{1.16}$$

where θ_M is the mixing angle in matter, given by [12]:

$$\sin^2 2\theta_M = \frac{(\frac{\Delta m^2}{2E})^2 \sin^2 2\theta}{(\frac{\Delta m^2}{2E}\cos 2^\theta + \sqrt{2}G_F N_e)^2 + (\frac{\Delta m^2}{2E})^2 \sin^2 2\theta} \tag{1.17}$$

The oscillation probability is of the same form as in Eq. 1.10, where the vacuum parameters are now replaced by those in matter. From Eq. 1.17 it follows that, regardless of the smallness of the mixing angle in vacuum, the mixing angle in matter can be large. In particular, maximal mixing can be achieved if the so-called MSW resonance condition is satisfied:

$$\sqrt{2}G_F N_e = \frac{\Delta m^2}{2E}\cos 2\theta \tag{1.18}$$

Since $N_e > 0$ Eq. 1.18 is fulfilled only if $\Delta m^2 \cos\theta > 0$. Once a convention on the phase has been chosen, Eq. 1.18 implies that resonant oscillation enhancement is possible only for one particular sign of Δm^2. This means that, for a given sign of Δm^2, matter effects cannot enhance neutrino and antineutrino oscillations at the same time: if neutrino oscillations are enhanced, antineutrino oscillations will be suppressed, and viceversa.

An interesting case to consider is the so-called adiabatic approximation for matter density monotonically decreasing along the neutrino path. Let us consider the case of two-flavour neutrino mixing (for example between ν_e and ν_μ, useful to describe neutrino oscillations in the Sun).

Electron neutrinos produced in the core of the Sun, where the density is above that corresponding to the MSW resonance, initially see a mixing angle $\theta_{core} \approx \pi/2$. From Eq. 1.16, at production point. a neutrino born as a ν_e, would essentially coincide with one of the matter eigenstates ν_2^M. The adiabaticity condition, that requires a slowly changing matter distribution, guarantees that the neutrino system can gradually adjust to the changing density of the environment and that it doesn't make transitions to the other matter eigenstate. As ν_2^M propagates through the mantle, it encounters regions of smaller densities: the effective mixing angle decreases and the strength of the mixing increases, until the resonance condition is fulfilled and maximal mixing is reached. As the neutrino travels further, the mixing angle becomes smaller and smaller, approaching the value of the mixing angle in vacuum, θ. If θ is small, the ν_e component of ν_2^M is small at the final point and ν_2^M is mainly composed of ν_μ. The survival and the oscillation probabilities for electron neutrinos are given by:

$$P(\nu_e \to \nu_e) = \sin^2\theta \qquad P(\nu_e \to \nu_\mu) = \cos^2\theta$$

Thus, in the range of validity of the adiabatic approximation for small values of the mixing angle in vacuum, if the depth of the traversed matter is large enough, the probability of finding the neutrino in the flavour state ν_e, when it gets outside the Sun is tiny and a complete conversion of ν_e to ν_μ is possible.

1.6 Neutrino oscillation phenomenology

There are two types of possible neutrino oscillation experiments, appearance and disappearance.

For an appearance search, an experiment looks for the anomalous appearance of ν_e or ν_τ in a relatively pure ν_μ beam and studies this as a function of distance, L, and energy, E. In a disappearance experiment, one looks for a change in the beam ν flux as a function of L and E.

This type of experiment relies on knowing accurately the neutrino flux and interaction cross sections. The range of values for the parameters, Δm^2 and $\sin^2 2\theta$, sets the demands on the search experiment. The mixing angle $\sin^2 2\theta$ sets the size of oscillation effects and thus the needed statistical sample. The Δm^2 value sets the distance to energy ratio needed for the neutrinos to oscillate with an oscillation length given by $L_{osc} = \pi E/(1.27\Delta m^2)$.

Results from oscillation experiments are typically displayed on a two dimensional plot of Δm^2 versus $\sin^2 2\theta$ assuming a two component mixing formula. If an experiment sees an oscillation signal with a probability given by $P_{osc} = P_{signal} + \delta P_{signal}$, then, within some confidence level, a region in the (Δm^2, $\sin^2 2\theta$) plane is allowed. If, on the other hand, an experiment sees no signal and limits the probability of a specific oscillation channel to be $P_{osc} < P$ at 90% CL, then an excluded region is displayed in the (Δm^2, $\sin^2 2\theta$) plane.

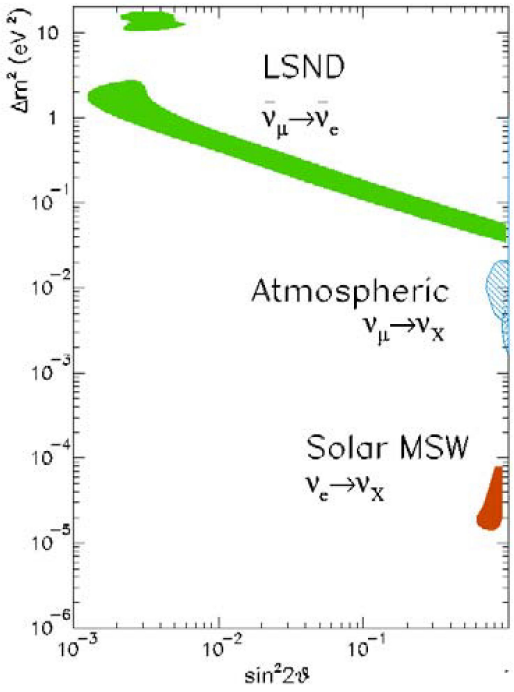

Figure 1.1: Summary of oscillation signals from current experimental results.

The current experimental situation is displayed in Fig. 1.1. This plot shows three signal regions associated with solar, atmospheric, and LSND oscillation experiments. There have also been many negative searches that exclude many parts of the bidimensional plot.

Chapter 2

Experimental status

2.1 Direct measurements of neutrino mass

A variety of techniques have been used to search directly for neutrino mass effects in the weak decay of particles and nuclei. The most sensitive searches have been associated with electron neutrinos. Here, the tritium decay process

$$^3H \rightarrow ^3 He + e^- + \overline{\nu}_e$$

is investigated near the kinematic endpoint of the outgoing electron spectrum.

Muon neutrino mass can be probed by precision studies of the muon decay spectrum from pion decays:

$$\pi \rightarrow \mu + \nu$$

Experiments have used both π decay at rest, where the pion mass dominates the uncertainty; and π decay in flight, where the resolution in measuring $p_\pi - p_\mu$ limits the sensitivity.

High multiplicity tau lepton decays provide a "laboratory" for direct tau neutrino mass investigations. Tau lepton decays are measured near the edge of the allowed kinematic range for tau decays in the processes

$$\begin{aligned} \tau^- &\rightarrow 2\pi^-\pi^+\nu_\tau \\ \tau^- &\rightarrow 3\pi^-2\pi^+(\pi^0)\nu_\tau \end{aligned}$$

Fits are made to the scaled visible energy and scaled invariant mass looking for an excess of events near the kinematic boundary.

No indication of neutrino mass has been seen; the experiments yield the following upper limits [5][15, 17]:

$$m_{\nu_1} < 2.5 \text{ eV at } 95\% \text{ c.l. (Troitsk)}\,; < 2.2 \text{ eV at } 95\% \text{ c.l. (Mainz)}$$
$$m_{\nu_2} < 170 \text{ keV at } 90\% \text{ c.l. (PSI; } \pi^+ \to \mu^+ + \nu_\mu)$$
$$m_{\nu_3} < 15.5 \text{ MeV at } 95\% \text{ c.l. (ALEPH, CLEO, OPAL; } \tau \text{ decays)}$$

Here ν_1, ν_2 and ν_3 are assumed to be the primary mass components of ν_e, ν_μ and ν_τ, respectively. However, since we know that at least one mixing angle in the lepton sector is large, these limits may need a re-interpretation. In particular, the upper bound on m_{ν_3} may in fact be more stringent than the one quoted above.

2.2 The solar neutrino problem

According to the Solar Standard Model (SSM), all the solar energy is produced in a series of thermonuclear reactions and decay at he center of the sun (Fig. 2.1).

Neutrinos escape quickly from the sun, while the emitted photons suffer an enormous number of interactions and reach the surface of the sun in about one million years.

An important fraction of the energy of the sun is emitted in the form of ν_e energies from 0.1 to 14 MeV (Fig. 2.2).

Combining the neutrino energy with the large sun-to-earth distance ($1.5 \cdot 10^{11}$ m), gives sensitivity to Δm^2 value below 10^{10} eV^2.

Solar neutrino studies offer a unique tool to probe for neutrino oscillations at very small Δm^2.

Most of the emitted neutrinos come from the $p+p \to d+e^+ + \nu_e$ reaction, which yields ν_e's with energies $0 < E_{\nu_e} < 0.42$ MeV; they have interaction cross-sections of $\sim 10^{-45}$ cm^2. The highest energy neutrinos, coming from ^{8}B, have energies $0 < E_{\nu_e} < 14.06$ MeV and cross-sections $\sim 3 \times 10^{-43}$ cm^2. On Earth should arrive $\sim 7 \times 10^{10}$ ν_e cm^{-2} s^{-1}.

There are two types of solar neutrino experiments, the radiochemical experiments (Homestake, Sage, Gallex, GNO) and the scattering experiments (νe^-) (Super-Kamiokande and SNO). The Homestake experiment in the Homestake mine in Lead, South Dakota detects solar neutrinos through

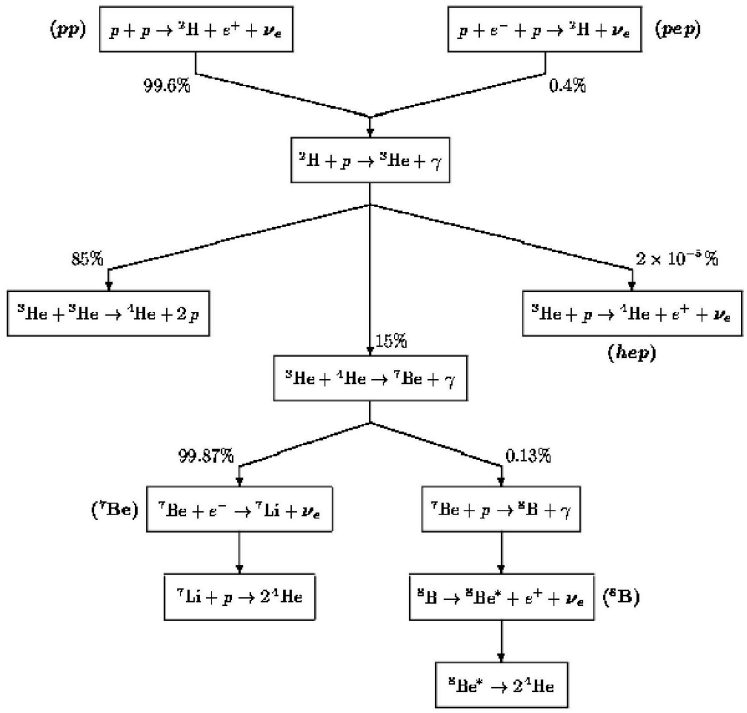

Figure 2.1: The solar processes with relative percentage probabilities for the various chains.

the process $\nu_e + {}^{37}Cl \rightarrow {}^{37}Ar + e^-$; this experiment is sensitive to solar neutrinos above 0.9 MeV (see Fig. 2.2). The gallium experiments, Sage, Gallex, GNO use the process $\nu_e + {}^{37}Ga \rightarrow {}^{37}Ge + e^-$, which has a much lower threshold allowing the experiment to detect the primary pp neutrinos with energies down to 0.2 MeV.

The Super-K experiment uses the elastic scattering process, $\nu + e^- \rightarrow \nu + e^-$, in a 22.5 kton fiducial mass water detector to measure the solar flux above the few MeV region. This process has good directional information and shows a clear angular peak pointing toward the sun. The Sudbury Neutrino Observatory (SNO) uses 1 kton of heavy water as a target. SNO detects ^{8}B solar neutrinos through the reactions:

$$\begin{array}{rcll} \nu_e + d & \rightarrow & p + p + e^- & \text{SNO CC} \\ \nu_x + d & \rightarrow & p + n + \nu_x & \text{SNO NC} \\ \nu_x + e^- & \rightarrow & \nu_x + e^- & \text{Super-K and SNO} \end{array}$$

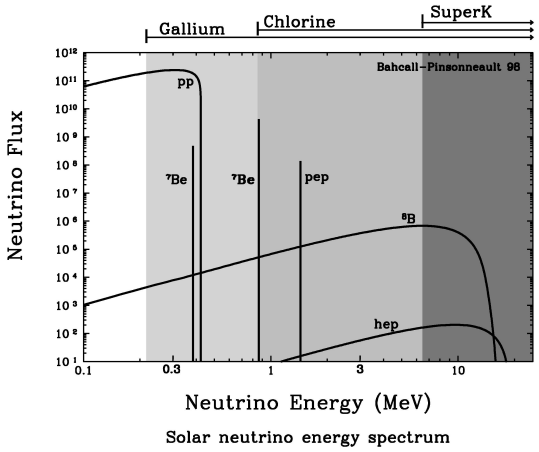

Figure 2.2: The energy spectrum of solar neutrinos produced by various processes in the sun. Also shown is the energy range covered by various experimental techniques.

The charged current reaction (CC) is sensitive only to ν_e, while the NC reaction is equally sensitive to all active neutrino flavours ($x = e, \mu, \tau$).

The elastic scattering reaction (ES) is sensitive to all flavours, but with reduced sensitivity to ν_μ and ν_τ. Sensitivity to the three reactions allows SNO to determine the electron and non-electron neutrino components of the solar flux.

The flux of ^{8}B neutrinos for $E_{eff} \geq 5$ MeV is (the 1st error is statistical, the 2nd systematical):

$$\phi_{CC} = 1.76^{+0.06+0.09}_{-0.05-0.09}, \quad \phi_{ES} = 2.39^{+0.24+0.12}_{-0.23-0.12}, \quad \phi_{NC} = 5.09^{+0.44+0.46}_{-0.43-0.43} \tag{2.1}$$

The fluxes of electron neutrinos, ϕ_e, and of ν_m+ν_t, $\phi_{\mu\tau}$, are:

$$\phi_e = 1.76^{+0.05+0.09}_{-0.05-0.09}, \quad \phi_{\mu\tau} = 3.41^{+0.45+0.48}_{-0.45-0.45} \tag{2.2}$$

The total flux $\phi_e + \phi_{\mu\tau}$ is that expected from the Standard Solar Model. Combining statistical and systematic uncertainties in quadrature, $\phi_{\mu\tau}$ is $3.41^{+0.66}_{-0.64}$, which is 5.3σ above zero, providing evidence for neutrino oscillations $\nu_e \rightarrow \nu_\mu, \nu_\tau$ with $\Delta m^2 \simeq 5.0 \times 10^{-5}$ and $\tan^2\theta \simeq 0.34$.

2.3 Atmospheric neutrino oscillation experiments

Atmospheric neutrinos are produced in the decay of secondary particles, mainly pions and kaons, created in the interactions of primary cosmic rays with the nuclei (N) of the Earth's atmosphere. The ratio of the numbers of muon to electron neutrinos is about

$$R = \frac{N_{\nu_\mu} + N_{\bar{\nu}_\mu}}{N_{\nu_e} + N_{\bar{\nu}_e}} = \simeq 2$$

The exact value of R can be affected by several effects, such as the primary energy spectrum and composition, the geomagnetic cut-off, the solar activity and the details of the model for the development of the hadronic shower. However, although the absolute neutrino are rather badly known (predictions from different calculations disagree by $\simeq 20\%$), the ratio R is known at $\simeq 5\%$. Neutrino oscillations could manifest as a discrepancy between the measured and the expected value of the ratio R.

Atmospheric neutrinos are well suited for the study of neutrino oscillations, since they have energies from a fraction of GeV up to more than 100 GeV and they travel distances L from few tens of km up to 13000 km; thus L/E_ν ranges from $\sim$ 1 km/GeV to $\sim 10^5$ km/GeV.

One may consider that there are two sources for a single detector: a near one (downgoing neutrinos) and a far one (upgoing neutrinos).

In the no-oscillation hypothesis, the zenith angle distribution must be up-down symmetric, assuming no other phenomena affecting the neutrino angular distribution relative to the local vertical direction. Conversely, any deviation from up-down symmetry could be interpreted as an indication for neutrino oscillations.

Several large underground detectors, located below a cover of 1-2 km of rocks, studied (and are studying) atmospheric neutrinos. The Soudan 2 [22], MACRO [23] and SuperKamiokande [24] detectors reported deficits in the ν_μ fluxes with respect to the Monte Carlo (MC) predictions and a distortion of the angular distributions; which may be explained in terms of $\nu_\mu \longleftrightarrow \nu_\tau$ oscillations.

Results from the Soudan 2 experiment

The Soudan 2 experiment uses a modular fine grained tracking and showering calorimeter of 963 t. It is located 2100 *m.w.e.* underground in the Soudan Gold mine in Minnesota. The bulk of the mass consists of 1.6 mm thick corrugated steel sheets interleaved with drift tubes. The detector is surrounded by an anticoincidence shield.

An event having a leading, non-scattering track with ionization dE/dx compatible with that from a muon is a candidate CC event of ν_μ flavour; an event yielding a relatively energetic shower is a candidate ν_e CC event. Multiprong events are not considered at present. Events without hits in the shield are called *Gold Events*, while events with two or more hits in the shield are called *Rock Events*.

After corrections for cosmic ray muon induced background, the Soudan 2 double ratio for the whole zenith angle range ($-1 \leq \cos\Theta \leq 1$) is $R' = (N_\mu/N_e)_{DATA}/(N_\mu/N_e)_{MC} = 0.68 \pm 0.11_{stat} \pm 0.06_{sys}$ which is consistent with muon neutrino oscillations.

The (L/E_ν) distributions for ν_e and ν_μ charged current events show the expected trend for $\nu_\mu \rightarrow \nu_\tau$ oscillation. The ν_e data agree with the no oscillation MC predictions, while the ν_μ data are lower; this is consistent with oscillations in the ν_μ channel and no oscillations for ν_e. The double peak structure arises from the acceptance of the apparatus.

The 90% C.L. allowed region in the $\sin^2 2\theta - \Delta m^2$ plane, computed using the Feldman-Cousins method [25] is shown in Fig. 2.5b, where it is compared with the allowed regions obtained by the SK and MACRO experiments.

Results from the MACRO experiment

The MACRO detector was located in the Gran Sasso Laboratory, at an average rock overburden of 3700 hg/cm^2 [23]. The detection elements were planes of streamer tubes for tracking and liquid scintillation counters

In the MC simulation of upthroughgoing muons, the neutrino flux computed by the Bartol group and the cross sections for the neutrino interactions calculated using the deep inelastic parton distribution [**?**] are used. For the low energy data, the simulations use the Bartol neutrino flux and the low energy neutrino cross sections [**?**].

• **Upthroughgoing muons ($E_\mu > 1$ GeV)** They come from interactions in the rock below the detector of ν_μ with $\langle E_\nu \rangle \sim 50$ GeV. The ratio of

the observed number of events to the expectation without oscillations in $-1 < \cos\Theta < 0$ is $R = 0.721 \pm 0.026_{stat} \pm 0.043_{sys} \pm 0.123_{th}$. Fig. 2.3a shows the zenith angle distribution of the measured flux of upthroughgoing muons; the MC expectation for no oscillations is indicated by the dashed line. The best fit to the number of events and to the shape of the zenith angle distribution, assuming $\nu_\mu \longleftrightarrow \nu_\tau$ oscillations, yields $\sin^2 2\theta = 1$ and $\Delta m^2 = 2.5 \cdot 10^{-3}$ eV^2 (solid line).

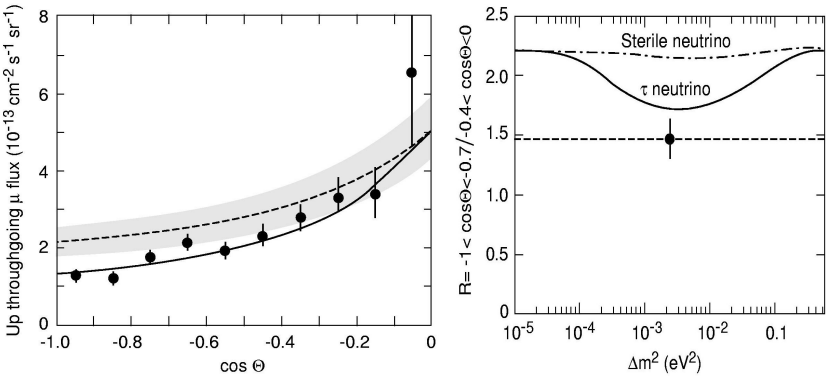

(a) (b)

Figure 2.3: (a) Zenith distribution of the upthroughgoing muons in MACRO. The data (black points) have error bars with statistical and systematic errors added in quadrature. The shaded region shows the theoretical scale error band of ±17% on the normalization of the Bartol flux for no oscillations. The solid line is the fit to an oscillated flux which yields maximal mixing and $\Delta m^2 = 2.5 \cdot 10^{-3}$ eV^2. (b) Ratio of events with $-1 < \cos\Theta < -0.7$ to events with $-0.4 < \cos\Theta < 0$ as a function of Δm^2 for maximal mixing. The black point with error bar is the measured value, the solid line is the prediction for $\nu_\mu \longleftrightarrow \nu_\tau$ oscillations, the dashed-dotted line is the prediction for $\nu_\mu \longleftrightarrow \nu_{sterile}$ oscillations.

The 90% C.L. allowed region in the $\sin^2 2\theta - \Delta m^2$ plane, computed using the Feldman-Cousins method [25] is shown in Fig. 2.5b, where it is compared with those obtained by the SuperKamiokande and Soudan 2 experiments.

• $\boldsymbol{\nu_\mu \longleftrightarrow \nu_\tau}$ **against** $\boldsymbol{\nu_\mu \longleftrightarrow \nu_{sterile}}$ Matter effects due to the difference between the weak interaction effective potential for muon neutrinos with respect to sterile neutrinos, which have null potential, yield different total

number and different zenith distributions of upgoing muons. In Fig. 2.3b the measured ratio between the events with $-1 < \cos\Theta < -0.7$ and the events with $-0.4 < \cos\Theta < 0$ is shown [23]. MACRO measured 305 events with $-1 < \cos\Theta < -0.7$ and 206 events with $-0.4 < \cos\Theta < 0$; the ratio is $R = 1.48 \pm 0.13_{stat} \pm 0.10_{sys}$. For $\Delta m^2 = 2.5 \cdot 10^{-3}$ eV^2 and maximal mixing, the minimum expected value of the ratio for $\nu_\mu \longleftrightarrow \nu_\tau$ is $R_\tau = 1.72$ and for $\nu_\mu \longleftrightarrow \nu_{sterile}$ is $R_{sterile} = 2.16$. One concludes that $\nu_\mu \longleftrightarrow \nu_{sterile}$ oscillations (with any mixing) are excluded at 99% C.L. compared to the $\nu_\mu \longleftrightarrow \nu_\tau$ channel with maximal mixing and $\Delta m^2 = 2.5 \cdot 10^{-3}$ eV^2.

• **Low energy events** The low energy data show a uniform deficit of the measured number of events over the whole angular distribution with respect to the predictions; the data are in good agreement with the predictions based on $\nu_\mu \longleftrightarrow \nu_\tau$ oscillations with the parameters obtained from the upthrough-going muon sample.

Results from the SuperKamiokande experiment

SuperKamiokande [24] (SK) is a large cylindrical water Cherenkov detector containing 50 kt of water; it is seen by inner-facing phototubes. The detector is located in the Kamioka mine, Japan, under 2700 *m.w.e.*

Atmospheric neutrinos are detected in SK by measuring the Cherenkov light generated by the charged particles produced in the neutrino CC interactions with the water nuclei. Thanks to the high PMT coverage, the experiment is characterised by a good light yield ($\sim$ 8 photo-electrons per MeV) and can detect events of energies as low as $\sim$ 5 MeV.

Fully contained events can be subdivided into two subsets, the so-called *sub-GeV* and *multi-GeV* events, with energies below and above 1.33 GeV, respectively. In SK jargon FC events include only single-ring events, while *multi-ring* ones (MRING) are treated as a separate category. Another sub-sample, defined as the *partially contained* events (PC), is represented by those CC interactions where the vertex is still within the fiducial volume, but at least a primary charged particle, typically the muon, exits the detector without releasing all of its energy. For these events the energy resolution is worse than for FC interactions. *Upward-going muons* (UPMU), produced by neutrinos coming from below and interacting in the rock, are further subdivided into *stopping muons* ($\langle E_\nu \rangle \sim 7$ GeV) and *throughgoing muons* ($\langle E_\nu \rangle \sim 70 \div 80$ GeV), according to whether or not they stop in the detector.

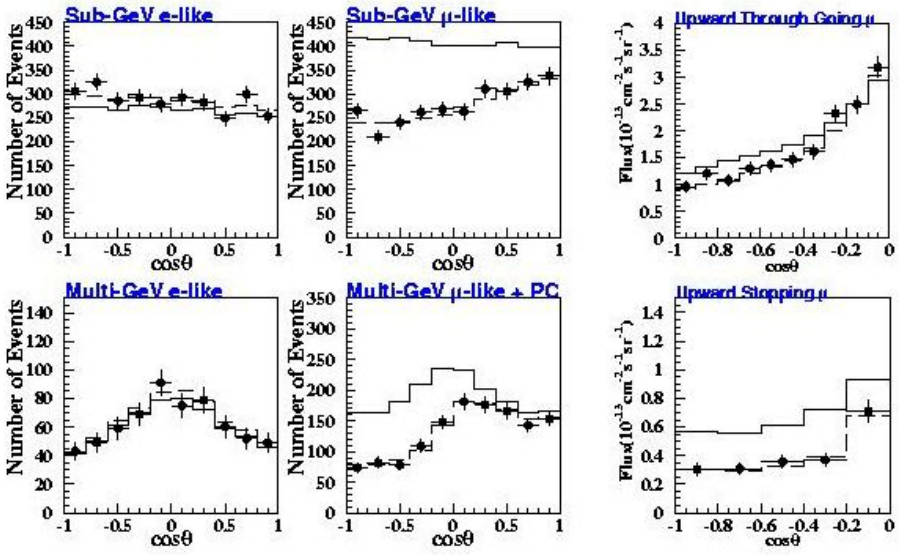

Figure 2.4: Zenith distributions for SK data (black points) for e-like and μ-like sub-GeV and multi-GeV events and for throughgoing and stopping muons. The solid lines are the no oscillation MC predictions, the dashed lines refer to $\nu_\mu \longleftrightarrow \nu_\tau$ oscillations with maximal mixing and $\Delta m^2 = 2.5 \cdot 10^{-3}$ eV^2.

The samples defined above explore different ranges of neutrino energies [**?**].

Particle identification in SuperKamiokande is performed using likelihood functions to parametrize the sharpness of the Cherenkov rings, which are more diffused for electrons than for muons. The algorithms are able to discriminate the two flavours with high purity (of the order of 98% for single track events). The zenith angle distributions for e-like and μ-like sub-GeV and multi-GeV events are shown in Fig. 2.4. The electron-like events are in agreement with the MC predictions in absence of oscillations, while the muon data are lower than the no oscillation expectations. Moreover, the μ-like data exhibit an up/down asymmetry in zenith angle, while no significant asymmetry is observed in the e-like data [24].

The recent value for the double ratio R' reported by SK, based on 1289 days of data, is $0.638^{+0.017}_{-0.017} \pm 0.050$ for the sub-GeV sample and $0.675^{+0.034}_{-0.032} \pm 0.080$ for the multi-GeV sample (both FC and PC). The ratio between observed and expected numbers of e-like and μ-like events as a function of L/E_ν

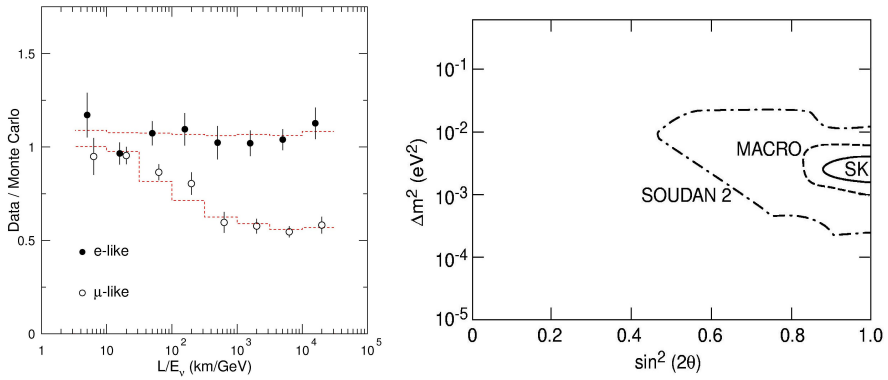

(a) (b)

Figure 2.5: (a) SK ratios between observed and expected numbers of e-like and μ-like events as a function of L/E_ν. (b) 90% C.L. allowed region contours for $\nu_\mu \longleftrightarrow \nu_\tau$ oscillations obtained by the SuperKamiokande, MACRO and Soudan 2 experiments.

is shown in Fig. 2.5a. The ratio e-like events/MC do not depend from L/E_ν while μ-like events/MC show a dependence on L/E_ν consistent with the oscillation hypothesis. Interpreting the muon-like event deficit as the result of $\nu_\mu \longleftrightarrow \nu_\tau$ oscillations in the two-flavour mixing scheme, SuperKamiokande computes an allowed domain for the oscillation parameters [24], see Fig. 2.5b. The events are binned in a multi-dimensional space defined by particle type, energy and zenith angle, plus a set of parameters to account for systematic uncertainties. The best fit using FC, PC, UPMU and MRING events [24] corresponds to maximal mixing and $\Delta m^2 = 2.5 \cdot 10^{-3}$ eV^2, Fig. 2.5b.

SK reported also data on upthroughgoing muons, which agree with the predictions of an oscillated flux with the above parameters.

- **$\nu_\mu \longleftrightarrow \nu_\tau$ against $\nu_\mu \longleftrightarrow \nu_{sterile}$**

If the observed deficit of ν_μ were due to $\nu_\mu \longleftrightarrow \nu_{sterile}$ oscillations, then the number of events produced via neutral current (NC) interaction for upgoing neutrinos should also be reduced. Moreover, in the case of $\nu_\mu \longleftrightarrow \nu_{sterile}$ oscillations, matter effects will suppress oscillations in the high energy ($E_\nu > 15$ GeV) region. The following data samples were used to search for these effects: (a) NC enriched sample, (b) the high-energy ($E > 5$ GeV) PC sample and (c) upthroughgoing muons. The excluded regions obtained by

a combined ((a),(b)and(c)) analysis and by the analysis of 1-ring-FC show that $\nu_\mu \longleftrightarrow \nu_{sterile}$ oscillations are disfavored with respect to $\nu_\mu \longleftrightarrow \nu_\tau$ oscillations at a C.L. of 99% [24].

All muon data are in agreement with the hypothesis of two flavour $\nu_\mu \longleftrightarrow \nu_\tau$ oscillations, with maximal mixing and $\Delta m^2 \sim 2.5 \cdot 10^{-3}$ eV^2. The hypothesis of $\nu_\mu \longleftrightarrow \nu_{sterile}$ oscillations is disfavoured at 99% C.L. for any mixing. The 90% C.L. contours of Soudan 2, MACRO and SuperKamiokande overlap, see Fig. 2.5b.

2.4 Long-baseline oscillation experiments

Long-baseline oscillation experiments can be used to check the atmospheric results with better control of systematics, using a well-understood accelerator-produced neutrino beam. They also hold the promise of doing more detailed quantitative measurements of the oscillation parameters, and seeing directly the oscillatory behavior in energy and distance expected from oscillations versus other explanations. With high statistics and good control of systematics, these experiments can also address flavor issues: checking the existence of any $\nu_\mu \rightarrow \nu_{sterile}$ component; directly observing ν_τ events; and looking for the sub-dominant $\nu_\mu \rightarrow \nu_e$ oscillation. With accelerator-produced neutrino beams in the few GeV energy range, the distance to a far detector must be at least hundreds of km.

Using the 12 GeV KEK proton synchrotron in Japan, the K2K experiment has set up a low energy neutrino beam, $\langle E_\nu \rangle = 1.4$ GeV, directed towards the Super-K detector 250 km away. The experiment also has near detectors at a 100 m distance for monitoring the beam and for use in comparing to the rates in Super-K detector. With about half of their expected data, the experiment has seen a significant deficit of interactions in Super-K relative to the near detectors [18], observing 56 events with an expectation of 80.6 ± 8.0 events with no oscillations and 52.0 events for $\Delta m^2 = 3 \cdot 10^{-3}$ eV^2. The deficit is mainly in the region with energy below 1 GeV , is consistent with oscillations with $\Delta m^2 \approx 10^{-3}$ eV^2 , and rules out the no oscillation hypothesis at 97% CL.

MINOS will have a 5.4 kton detector located in the Soudan mine in northern Minnesota. A neutrino beam (NuMI - Neutrinos from the Main Injector) using 120 GeV protons from the Fermilab Main Injector is produced

using an 800 m long decay pipe excavated in the rock below the Fermilab site and pointing down at a angle of 3.3 degrees towards Minnesota. There is also a 1 kton near detector for beam monitoring and comparison. The far (and near) detector are composed of 8 m diameter, 1 inch thick steel plates interspersed with solid scintillator planes composed of 4 cm wide long strips. The detector is 31 m long, composed of 486 layers, and magnetized with a toroidal magnetic field averaging 1.5 Tesla. The horn focusing system for the neutrino beam is flexible and can provide beams with mean energies between about 3 and 20 GeV.

MINOS is well set up to investigate ν_μ oscillations in the atmospheric Δm^2 region. The main technique would be a disappearance measurement comparing the observed ν_μ CC rate with that derived from the near detector. With a low energy beam configuration, the experiment expects to see ~ 700 CC events/yr in the far detector, giving sensitivity to $\Delta m^2 > 10^{-3}$ eV^2 and measurement capabilities for the oscillation parameters Δm^2 to the 10-20% level and $\sin^2 2\theta$ to 0.10. With this sample, the MINOS experiment will completely cover the Super-K atmospheric allowed region to 3.5σ. In addition, MINOS can search for a $\nu_\mu \rightarrow \nu_{sterile}$ component by measuring the CC/NC rate in the near and far detector. For $\nu_\mu \rightarrow \nu_\tau$, the CC production of τ's will look like NC events 80% of the time so the CC/NC ratio will go down relative to no oscillations. On the other hand, for $\nu_\mu \rightarrow \nu_{sterile}$ oscillations, both the CC and NC will be reduced by the same factor keeping the ratio constant.

CERN is also planning a long-baseline program (CNGS - CERN to Gran Sasso) based on two appearance experiments, OPERA and ICARUS. The experiments are to be housed in the Gran Sasso Laboratory, which is located 732 km from CERN. The neutrino beam will be produced using 400 GeV protons from the CERN SPS with secondary pions and kaons focused with a magnetic horn into a 900 m decay pipe. The expected spectrum is of higher energy than NuMI and optimized to detect the appearance of ν_τ events. Since there are almost no intrinsic ν_τs in the beam, a near detector is not planned and an oscillation signal can be confirmed with only a few events.

The OPERA experiment will be explained with more details in the Chap. 3. The other CNGS experiment is ICARUS, which is to use a 5 ktons of liquid argon instrumented as time projection chambers. If successful, this experiment will be a true electronic bubble chamber with excellent detection and identification properties for all species of neutrino events.

Both ICARUS and OPERA as designed should have sensitivity over the full MACRO and Super-K allowed region, decreasing in the lower $\Delta m^2 = 10^{-3}$ region.

2.5 Oscillation experiments at high Δm^2

Using the 800 MeV proton beam from the LANSCE accelerator, the LSND (Liquid Scintillation Neutrino Detector) observed an excess of $\overline{\nu}_e$ events in the beam starting without this component. The beam was produced from stopping π^+ made from interactions of the 800 MeV protons in the beam stop. (Almost all π^- are captured and do not decay.) The π^+ decay chain produced ν_μ, ν_e, and $\overline{\nu}_\mu$ neutrinos, but no $\overline{\nu}_e$ neutrinos. The claimed oscillation signal was then associated with an excess of $\overline{\nu}_e$ events tentatively from $\overline{\nu}_\mu \rightarrow \overline{\nu}_e$ oscillations:

$$\begin{array}{lll} \pi \rightarrow \mu^+ & \nu_\mu & \\ & \hookrightarrow e^+\nu_e & \overline{\nu}\mu \\ & & \hookrightarrow \overline{\nu}_e + p \rightarrow^+ + n \quad \text{if osc.} \end{array}$$

The LSND detector has 167 tons of liquid scintillator in a cylindrical tank viewed by 1280 8-inch photomultiplier tubes on the outer surface looking inward, and is located 30 m from the beam stop. $\overline{\nu}_\mu \rightarrow \overline{\nu}_e$ oscillations are probed for $\overline{\nu}_\mu$ energies between 20 and 55 MeV. The final LSND results have been published, and indicate an excess of $87.9 \pm 22.4 \pm 6.0$ $\overline{\nu}_e$ events corresponding to a 3.3σ $0.264 \pm 0.067 \pm 0.045$ % oscillation probability [20].

The KARMEN II experiment has also investigated this region of oscillation parameter space although with less sensitivity than LSND. KARMEN uses a pulsed 800 MeV proton beam from the Rutherford ISIS accelerator. The beam is again a beam-stop pion decay at rest beam located 17.6 m from the KARMEN detector. The detector used 56 tons of liquid scintillator contained in 512 modules that were Gd doped to have better neutron capture e.ciency. Overall, the KARMEN II experiment probes the upper Δm^2 part of the LSND signal range. The data sample is ten times smaller than LSND due to lower neutrino flux and less detector mass; the detector is located closer to the neutrino source. For their final results, KARMEN II observed no excess of $\overline{\nu}_e$ events.

A joint analysis of the LSND and KARMEN II results, found that that the two experiments are incompatible at the 36% level [21].

The MiniBooNE experiment is designed to make a definitive investigation of $\nu_\mu \rightarrow \nu_e$ oscillations in the LSND signal region. The experiment uses 8 GeV protons from the Fermilab booster synchrotron to produce a wide-band neutrino beam with a mean energy of about 1 GeV. A spherical detector, 12 m in diameter, is located 500 m away. The detector is filled with 800 tons of mineral oil and instrumented with $\sim$ 1280 8-inch phototubes on the surface looking inward.

The MiniBooNE beam is a very pure ν_μ beam with only a small contamination of ν_e from K_{e3} and μ decay. With two years of running, MiniBooNE expects to record hundreds of thousands of ν_μ CC events over a background of a few thousand ν_e and mis-identified events. The distance and energy are matched to the LSND signal region with an $L/E \sim 1$ m/MeV and, if the LSND signal is true, MiniBooNE should see hundreds to thousands of excess events.

Chapter 3

The OPERA Experiment

3.1 Introduction

OPERA is a long baseline experiment proposed for the direct search of ν_τ's appearance in an almost pure ν_μ beam (the CNGS neutrino beam). It will be located at the Gran Sasso Laboratory, in the middle of Italy, at a distance of 732 km from the CERN SPS where muon neutrinos will be produced. The beam energy has been tuned above the τ lepton production threshold and in the oscillation parameter region indicated by the atmospheric neutrino experiments.

The discovery potential of OPERA originates from the observation of a ν_τ signal with low background. The direct observation of $\nu_\mu \leftrightarrow \nu_\tau$ appearance will constitute a milestone in the study of neutrino oscillations.

The detector design is based on a massive lead/nuclear emulsion target. Nuclear emulsions are used as high resolution tracking devices, for the direct observation of the decay of the τ leptons produced in ν_τ charged current (CC) interactions. Magnetised iron spectrometers measure charge and momentum of muons. Electronic detectors locate the events in the emulsions (Target Trackers).

Moreover a veto detector system is required to flag events from neutrino interactions in the rocks surrounding the OPERA detector.

The OPERA experiment is designed starting from the Emulsion Cloud Chamber (ECC) concept, which combines in one cell the high precision tracking capabilities of nuclear emulsions and the large target mass given by the lead plates. By piling-up a series of cells in a sandwich-like structure one

obtains a brick, which constitutes the detector element appropriate for the assembly of more massive planar structures (walls). A wall and its related electronic tracker planes constitute a module. A supermodule is made of a target section, which is a sequence of modules, and of a downstream muon spectrometer. The final detector baseline will consist of two supermodules, for a total mass of $\sim$ 1.8 kt.

3.2 The CNGS neutrino beam

The original CNGS reference neutrino beam from the CERN SPS to the Gran Sasso is described in [26]. In November 2000 a new version of the CNGS beam was released, which gives $\sim$8% more ν_μCC events and $\sim$2% more ν_τCC events.

A schematic overview of the CNGS neutrino beam is shown in Fig. 3.1. SPS protons hit a graphite target made of a series of rods, for an overall target length of 2 m, producing secondary pions and kaons. The target rod diameter is 4 mm so that the proton beam is well contained within the target.

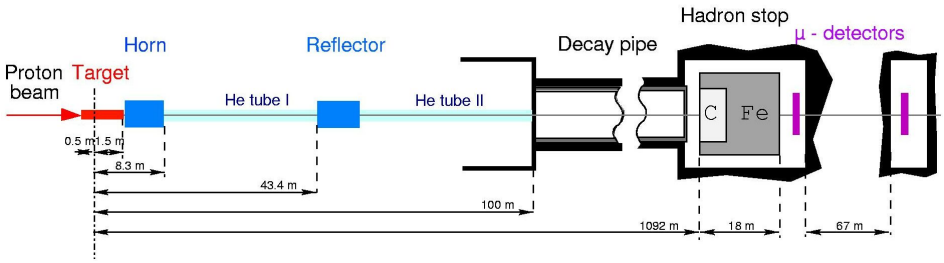

Figure 3.1: Layout of the CNGS neutrino beam. The coordinate origin is the focus of the proton beam.

The first coaxial lens, the horn, starts at 1.7 m from the focus of the proton beam. The second one, the reflector, is 43.4 m downstream of the focus.

Helium tubes are placed in the free spaces of the target chamber in order to reduce the interaction probability for secondary hadrons. A first tube is located between the horn and reflector, while a second one fills the gap between the reflector and the decay tunnel placed downstream.

Pions and kaons focused by the optics are then directed towards the decay tunnel to produce the neutrino beam. The typical π decay length (2.2

km at 40 GeV/c) makes a long decay tunnel justified. Given the angular distribution of the parent mesons, the longer the decay tunnel the larger must its diameter be. A tunnel of 2.45 m diameter and 1000 m length has been chosen for the CNGS. A massive iron hadron stopper is situated at the exit of the decay tunnel.

The signals induced by muons (from meson decays) in two arrays of silicon detectors placed in the hadron stopper are used for the online monitoring and the tuning of the beam (steering of the proton beam on target, horn and reflector alignment, etc.). The separation of the two arrays, equivalent to 25 m of iron, allows a rough measurement of the muon energy spectrum and of the beam angular distribution.

The SPS proton beam intensity is one of the main ingredients needed to achieve the physics goal of our experiment. However, the CNGS target constraints have to be taken into account.

Two possible CNGS running modes are envisaged: the *shared mode*, in which both CNGS and fixed-target users are supplied with protons; the *dedicated mode*, in which the CNGS is the only user. By assuming a 400 GeV/c proton beam and 200 days of running per year, the expected number of pot is $4.5 \cdot 10^{19}/year$ in the shared mode and $7.6 \cdot 10^{19}/year$ in the dedicated mode [28].

The CNGS beam features are summarised in Tab. 3.1. They concern the numbers of neutrino CC interactions including deep-inelastics (DIS) and quasi-elastics plus resonances (QE). The expected rate of ν_τ CC interactions for $\sin^2 2\theta = 1$ and different values of Δm^2 are given in Tab. 3.2.

ν_μ (m^{-2}/pot)	$7.45 \cdot 10^{-9}$
ν_τ CC events/pot/kton	$5.44 \cdot 10^{-17}$
$\langle E \rangle_{\nu_\mu}$	17
ν_e/ν_μ	0.8%
$\bar{\nu}_\mu/\nu_\mu$	2.0%
$\bar{\nu}_e/\nu_\mu$	0.05%

Table 3.1: Nominal features of the CNGS reference beam [28].

OPERA expects about 32000 neutrino interactions (including all neutrino flavours and NC events) in a five year run with a $\sim$ 2 kton detector mass. This correponds to about 30 events per day with shared beam operation.

Δm^2	ν_τ CC interactions/kton/year
$1 \cdot 10^{-3}$ eV^2	2.48
$3.5 \cdot 10^{-3}$ eV^2	30.4
$5 \cdot 10^{-3}$ eV^2	62.0

Table 3.2: Number of ν_τ CC interactions at Gran Sasso per kton and per year (shared mode). The expectations for different values of Δm^2 eV^2 and for $\sin^2(2\theta) = 1$ are given [28].

An increase of the the CNGS neutrino flux and a fine-tuning of the beam spectra to match the characteristics of the Gran Sasso experiments will certainly be beneficial for the $\nu_\mu \leftrightarrow \nu_\tau$ appearance programme of the CNGS project; in particular an increase of the beam intensity by a factor 1.5 could be achieved at moderate cost.

3.3 Detector structure and operation

The module and supermodule dimensions are governed by the efficient use of the space in the underground hall. The beam size is not an issue, as its RMS value at Gran Sasso is about 800 m [26]. This would justify the maximal transverse dimensions of the modules, compatibly with the need for sufficient lateral space in the underground hall for services and brick handling. One has then to provide large surface electronic detectors and iron magnets. These considerations favour a transverse target dimensions of about 6 - 7m. The transverse shape of the target is nearly square and matches with cross section of the muon spectrometer.

A schematic view of the OPERA detector is shown in Fig. 3.2.

3.3.1 Target

The ECC cell is shown in Fig. 3.3. It is composed of a 1 mm thick lead plate followed by a pair of emulsion layers each about 42 μm thick coated on both sides of a 200 μm plastic base. A charged particle produces two track segments in each emulsion layers. The number of grains (15-20) in 40 μm is adequate for the reconstruction of track segments by means of automatic scanning devices.

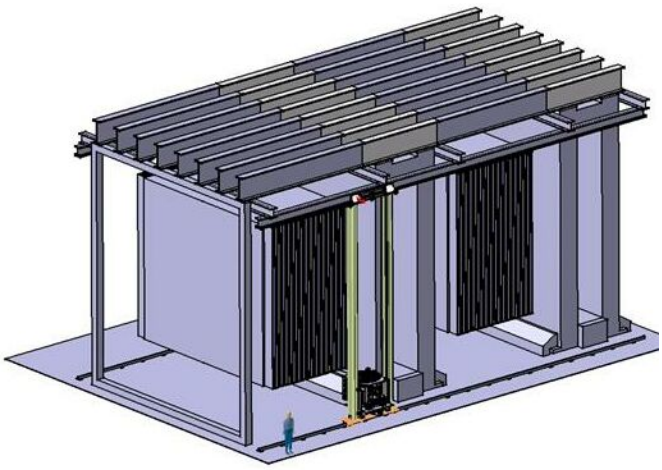

Figure 3.2: Schematic view of the OPERA detector.

Each brick has transverse dimensions of $10.2 \cdot 12.9\ cm^2$ It consists of 56 cells with a total thickness of about 7.6 cm (10 X_0) and a weight of 8.3 kg.

The dimensions of the bricks are determined by conflicting requirements: the mass of the bricks selected and removed for analysis should represent a small fraction of the total target mass; on the other hand, the brick transverse dimensions should be substantially larger than the uncertainties on the interaction vertex position predicted by the electronic trackers.

The brick thickness in units of radiation lengths is large enough to allow electron identification through their electromagnetic showering and momentum measurement by multiple coulomb scattering following tracks in consecutive cells. An efficient electron identification requires about 3 - 4 X_0 and the multiple scattering requires $\sim 5\ X_0$. With a 10 X_0 brick thickness, for half of the events such measurements can be done within the same brick where the interaction took place, without the need to follow tracks into downstream bricks.

Downstream of a brick a Changeable Sheet (CS) will be placed to interface each individual brick with the closest downstream target tracker plane. The purposes of these sheets are twofold. They allow a reduction of the scanning load with respect to the original brick proposal. There, both a Special Sheet

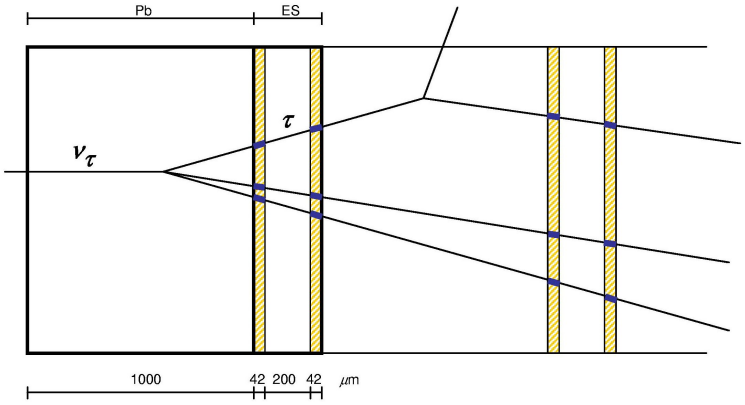

Figure 3.3: Schematic structure of an ECC cell in the OPERA experiment. The τ decay kink is reconstructed in space by using four track segments in the emulsion films.

and a Veto Sheet where assumed in order to locate ν vertex and to align bricks with cosmic rays. Moreover, the use of CSs will increase the brick finding efficiency, since they will help to reduce the ambiguities related to back-scattered tracks.

A target supermodule consists of 31 modules, each made of a wall of 3328 bricks followed by two planes of electronic trackers. The module dimensions are $\sim$ 12 cm in thickness and $\sim$ 6.75 m side to side. The dead space between bricks is ($\sim$ 4 mm) and the clearance between consecutive brick walls is 3.6 cm, in order to accommodate the electronic trackers. This makes the total length of one supermodule target about 370 cm.

A supermodule comprises 103168 bricks for a mass of $\sim$ 815 t of lead. Table 3.3 lists the features of a target supermodule.

3.3.2 Electronic detectors in the target modules

Electronic detectors placed downstream of each emulsion brick wall are used to select the brick (to be removed for analysis) where the neutrino interaction took place and to guide the scanning, by defining the region of the films to be scanned. The confirmation of the fired brick will be made by the CS

Dimensions	$\sim$ 6.71(H) x 6.75(W) x 3.75(L) m^3
ECC thickness (mm)	1.3
Number of emulsions films/brick	56 + 1 CS
Brick x-section (cm^2)	10.2 x 12.7
Brick thickness (cm)	7.6 (packing not included)
Brick thickness (X_0)	10
Brick weight (kg)	7.9 (lead) + 0.4 (films) = 8.3
Module thickness (cm)	12
Number of modules/superm.	31
Number of bricks/superm.	103168
Emulsions films surface/superm. (m^2)	$\sim$75000
Target superm. weight (ton)	815 (lead) + 41 (films) = 856

Table 3.3: Design features of the target section of a supermodule.

scanning, so a moderate spatial resolution can be tolerated, which allows to reduce the cost of the electronic trackers covering a large surface. For this purpose, plastic scintillator strips read out by wavelengthshifting (WLS) fibres have been chosen. They will be also used to sample the energy of hadronic showers and to contribute to the identification and reconstruction of penetrating tracks.

Each brick wall is followed by two electronic tracker planes (with strips oriented along the X and Y axis, respectively). The planes are squares of $\sim$ 6.7 m edge-to-edge and contain 256 scintillator strips. Each group of 64 strips constitutes an independent unit, read out on each side by a 64-pixel photodetector, such that 8 photodetectors are required for each tracker plane. No multiplexing scheme is foreseen.

The scintillator strip Target Trackers are 2.6 cm wide and 1 cm thick. Simulations have shown that a transverse segmentation below this value does not significantly improve the physics performance, in particular the brick finding efficiency. Their energy resolution is what expected from a calorimetric sampling, about $0.65/\sqrt{E(GeV)} + 0.16$; During the run, muons generated in the interaction of CNGS neutrinos in the cavern rock (rock muons), cosmics rays muons, radioactive sources and light injection systems will be used to calibrate the system.

The selection of the brick containing the neutrino interaction vertex is performed by combining different algorithms based on the observed trans-

verse and longitudinal event profiles as well as on the presence of individual reconstructed tracks. As an illustration, Fig. 3.4 shows a simulated ν_τ event with a muonic decay for one of the two projections transverse to the beam direction.

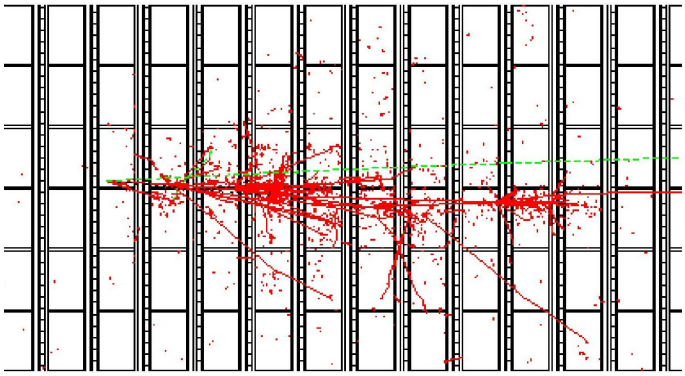

Figure 3.4: Display of a simulated $\tau \rightarrow \mu$ event in the OPERA target. The beam comes from the left of the figure. The primary vertex occurs in the third brick wall. Each wall of bricks is followed by the target tracker planes. These planes are oriented along the X and Y directions, perpendicular to the beam. The muon track corresponds to the longest track escaping on the right of the figure.

3.3.3 Muon spectrometers

The main goals of the spectrometers are the muon momentum and charge measurements. Each muon spectrometer consists of a dipolar magnet made of two iron walls interleaved by pairs of high resolution trackers. Each wall is made of 12 iron plates 5 cm thick. The iron is magnetised by a current of about 1200 A circulating in the top and bottom copper coils. The magnetic flux density in the tracking region is 1.55 T with vertical field lines of opposite directions in the two magnet walls. The transverse useful dimensions of the magnets are 8.75 m (horizontal) and 8 m (vertical) providing adequate geometrical acceptance also for muons originating in the upstream target volume.

The high resolution trackers, denoted as Precision Trackers, consist of vertical drift tube planes with an intrinsic resolution of 0.3 mm in the bend-

ing direction. Allowing for some misalignment, an overall resolution on each measured coordinate of 0.5 mm has been assumed in the following. The two tracker planes housed between the two magnet walls provide an angular measurement of the track with a 100 cm lever arm. The lever arm for the external trackers is 50 cm>This design leads to a momentum resolution better than 30% in the relevant kinematical domain.

The so-called Inner Trackers are inserted between the magnet iron plates. They are made of RPC detectors. On each face of the chambers, the induced pulses are collected by 3 cm wide pickup copper strips in the horizontal and vertical directions.

The Inner Trackers allow a coarse tracking inside the magnet to identify muons and ease track matching between the Precision Trackers. They also provide a measurement of the tail of the hadronic energy leaking from the target and of the range of muons which stop in the iron.

Fig. 3.4 shows a simulated ν_μ CC event occurring in the target section of a supermodule. The reconstruction of the event by the electronic detectors allows the identification of the vertex brick.

3.4 Physics performances

3.4.1 τ detection

The signal of the occurrence of $\nu_\mu \leftrightarrow \nu_\tau$ oscillations is the CC interaction of ν_τ's in the detector target ($\nu_\tau N \rightarrow \tau^- X$), through the decay topologies of its decay modes into an electron, or a muon or a single charged hadron:

$$\begin{aligned} \tau^- &\rightarrow e^- \nu_\tau \overline{\nu}_e \\ \tau^- &\rightarrow \mu^- \nu_\tau \overline{\nu}_\mu \\ \tau^- &\rightarrow h^- \nu_\tau (n\pi^0) \end{aligned}$$

Despite its distinctive topology the multi-prong channels of the τ has not yet been considered for the present estimate of the OPERA sensitivity, due to the less favourable signal to noise ratio.

Measurements of the branching ratio (BR) of the three single-prong decay modes give 17.8%, 17.7% and 49.5% for the electronic, muonic and hadronic

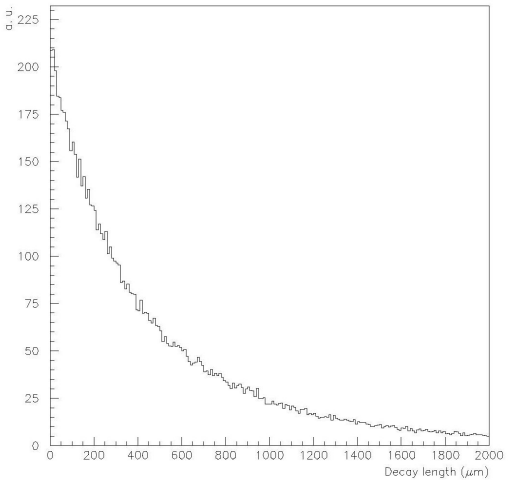

Figure 3.5: τ decay length distribution.

channel, respectively. For the typical τ energies expected with the CNGS beam one obtains the decay length distribution shown in Fig. 3.5.

If a τ is produced in a lead plate it will decay either in the same plate (short decays) or further downstream (long decays). For long decays, the τ is detected by measuring the angle between the charged decay daughter and the parent τ direction. Fig. 3.6 shows the distribution of the τ decay kink angle for the electron channel. For this measurement the directions of the tracks before and after the kink are reconstructed (in space) by means of the pair of emulsion films sandwiching the lead plate where the decay vertex occurred (Fig. 3.3). The τ can also decay in one of the films downstream of the vertex plate (e.g. in its plastic base). Even then, the kink angle can be reconstructed, albeit with a lower angular resolution, from the track segments in the emulsion layers on either side of the base. A fraction of the short decays is detectable by measuring a significant impact parameter (IP) of the daughter track with respect to the tracks originating from the primary vertex.

The detection of the τ decay into an electron benefits from the dense brick structure given by the compact cell design, which allows the electron identification through its showering in the downstream cells (Fig. 3.7).

For the muonic decay mode the presence of the penetrating (often isolated) muon track allows an easier event vertex finding. The potential back-

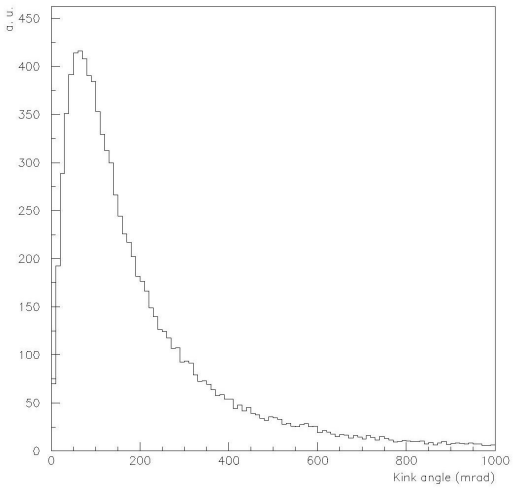

Figure 3.6: τ kink angle distribution for the $\tau \rightarrow e$ decay mode.

ground from large angle scattering of muons produced in ν_μ CC interactions can be reduced to a tolerable level by applying cuts on the kink angle and on the transverse muon momentum at the decay vertex.

Hadronic decay modes have the largest branching ratio but are affected by background due to hadron reinteractions. One of the primary hadrons, in fact, can interact in the first lead plates and, if the main lepton of this interaction are not detected in the emulsion, it may simulate the charged single-prong decay of the τ . Kinematical cuts can be used to reduce this background.

An important tool for background rejection is the determination of the transverse momentum of the daughter particle with respect to the direction of the τ track candidate. For electronic τ decays the ECC technique is well suited to identify electrons and to determine their energy by measuring the density of track segments associated to their showering in the brick. For charged hadrons and muons, the momentum is deduced from the measurement of the multiple scattering in the lead plates. As discussed in the following, the muon momentum is also measured by the electronic detectors in a large fraction of the cases.

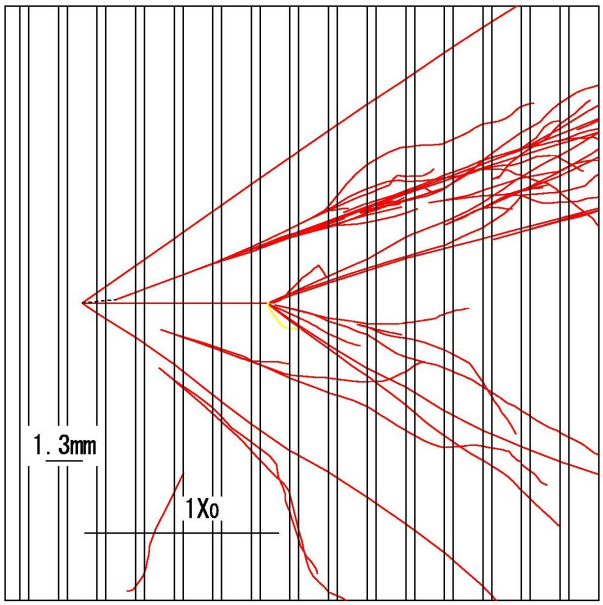

Figure 3.7: Simulated ν_τ event with τ decaying into an electron.

3.5 Efficiencies, background and sensitivity of the experiment

The signal detection efficiency of OPERA has been estimated on the basis of tests and simulations. The latter have been tuned with data obtained in emulsion experiments such as CHORUS and DONUT.

All single-prong τ decay modes are used to search for the so-called long τ decays. These are events in which the τ track is long enough to exit the lead plate where the primary vertex occurs. Short decays (in which the τ track is contained within the vertex plate) are considered for the $\tau \rightarrow e$ channel.

Long decay candidates are selected by detecting a kink topology and short decays by exploiting an impact parameter method. Kinematical cuts are applied to both samples in order to enhance the signal to background ratio.

The $\tau \rightarrow e$ decay mode is identified by the distinctive energy loss of the daughter electron in the lead/emulsion brick structure. The main background to this channel is given by charm production in ν_μ CC interactions undergoing electronic decay and with the primary muon escaping detection.

Muonic τ decays are characterised by an identified muon originating from the τ track kink. For these events the main background is constituted by large angle muon scattering in the lead plates.

Hadronic decay candidates are defined as those events in which the kink daughter particle is not identified either as an electron or a muon. In this case, charm production with subsequent hadronic decay and hadronic reinteractions in lead give a similar contribution to the background.

A summary of the τ detection efficiency in the three decay channels is given in Table 3, while the background contribution is given in Table 4. Table 5 summarises the expected numbers of background and τ events for different values of Δm^2 and full mixing, under the assumption of five years of running in the CNGS beam, operated in shared mode.

Assuming $\Delta m^2 = 2.5 \times 10^{-3}$ and full mixing, the probability to observe the number of events required to obtain a 4σ significance, is 97%.

Table 3: Summary of the τ detection efficiency ($\times$ BR) for different τ decay modes, topologies (long and short) and type of events (DIS and QE). The Proposal efficiencies are given within brackets.

Decay mode	DIS long (%)	QE long (%)	DIS short (%)	Total (%)
$\tau \to e^-$	2.7(3.0)	2.3(2.6)	1.2(1.3)	3.4(3.7)
$\tau \to \mu^-$	2.4(2.7)	2.5(2.8)	0.7(-)	2.8(2.7)
$\tau \to h^-$	2.8(2.2)	3.5(2.8)	-	2.9(2.3)
Total	8.0(8.0)	8.3(8.3)	1.9(1.3)	9.1(8.7)

Table 4: Expected background for the different channels. The numbers are normalised to 10^6 ν_μCC DIS events.

	$\tau \to e$	$\tau \to \mu$	$\tau \to h$	Total	Error
Long: charm	6.3	1.3	6.3	13.9	±15%
Long: ν_eCC and π^0	0.2	-	-	0.2	±10%
Long: μ scatt.	-	4.5	-	4.5	±50%
Long: had. reint.	-	-	4.5	4.5	±50%
Long: had. reint. CC	-	2.6	-	2.6	±50%
Long: had. reint. NC	-	4.4	-	5.0	±50%
Long total	6.5	12.8	10.8	30.1	-
Short: charm	1.0	0.5	(1.3)	1.5	±15%
Short: ν_eCC and π^0	0.1	-	-	0.1	±10%
Short: μ scatt.	-	1.1	-	1.1	±50%
Short: had. reint.	-	-	(6.1)	(6.1)	
Short Total	1.1	1.6	-	2.7	
Total	7.6	14.4	10.8	32.8	

Table 5: Expected numbers of τ and background events in OPERA after five years of data taking ($2.25 \times 10^{20} pot$). Signal events are given for full mixing and for three values of Δm^2: the present best fit from Super-Kamiokande and the two 90% CL limits. Overall, 23 events would be observed for the value indicated by Super-Kamiokande at the time of the CNGS approval [6] ($\Delta m^2 = 3.5 \times 10^{-3}\text{eV}^2$,$\sin^2 2\theta = 1$).

τ decay mode	Signal $(1.6 \times 10^{-3} eV^2)$	Signal $(2.5 \times 10^{-3} eV^2)$	Signal $(4.0 \times 10^{-3} eV^2)$	BG
e^- long	1.4	3.4	8.6	0.15
μ^- long	1.3	3.2	8.1	0.29
h^- long	1.6	3.7	9.4	0.23
e^- short	0.4	1.0	2.5	0.03
μ^- short	0.2	0.5	1.3	0.04
Total	4.9	11.8	30.0	0.74

Chapter 4

Nuclear Emulsions

Nuclear emulsion detectors provide three-dimensional spatial information on particle tracks, with excellent space resolution (of the order of 1 μm), as well as high hit density (300 hits/mm) along tracks. They are, therefore, ideal for the unambiguous detection of short-lived particles. This is crucial to attain the required sensitivity in the OPERA experiment.

4.1 Basic properties of emulsions

Nuclear emulsions are made of micro-crystals of silver halides (usually bromides AgBr) suspended in a gelatin composed by organic materials (Fig. 4.1). Despite their *low-tech* origin, emulsions remain the most sensitive detector with the highest space resolution: the passage of charged particles can become visible through a chemical amplification of the atomic-scale perturbations induced by energy losses of ionizing particles.

Nuclear emulsions are fundamentally the same as general purpose photographic emulsions, but have several distinguishing features: the silver halide crystals are very uniform in size and sensitivity, that is the capability to detect tracks with good efficiency; the silver to gelatin ratio is much higher than in a conventional emulsion; the thickness is larger.

The linear dimension of the crystals range from 0.1 μm to 1 μm. The size of the microcrystals for in the OPERA emulsions is $\sim$ 0.2 μm and is well controlled by the current industrial technologies developed for photographic films (Fig. 4.2).

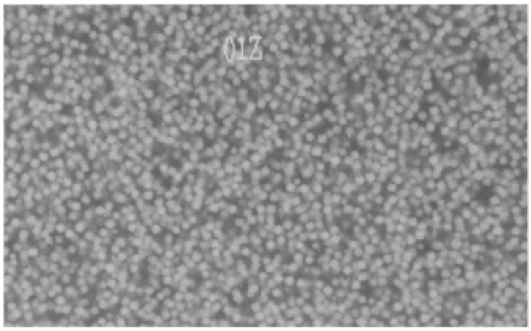

Figure 4.1: Micro-photograph of the crystals distributed in an emulsion layer of the OPERA experiment. Micro crystals can be recognised as white grains.

4.2 The photographic processes

A characteristics of silver halides is that, if they are opportunely sensibilized, the energy released by ionizing particles to the crystals, produces a latent image which is almost stable in time.

A developing agent reduces the AgBr to metallic Ag more rapidly than in the not irradiated crystals.

Therefore, when an emulsion is developed, all the crystals containing a latent image center are reduced to metallic silver. The other crystals are removed by fixing, and the result is a series of dark silver grains of about of 0.6 μm size, which can by observed by microscopes. The paths of an ionizing particle is visible as a sequence of these grains.

4.2.1 Formation of the latent image

When a silver halide crystal absorbs light or an ionising radiation, it has the effect of liberating mobile electrons and a positive hole $(AgBr)^+$. This can move through the crystal lattice, because of capture and release of electrons from adjacent bromine ion, while the electrons are trapped by impurities for example S used for sensibilization.

It is important for latent image formation that a significant proportion of electrons and positive holes are trapped separately, otherwise they could recombine and regenerate halide ions. The silver halide crystal contains free (interstitial) silver ions, which can move through the lattice. When an inter-

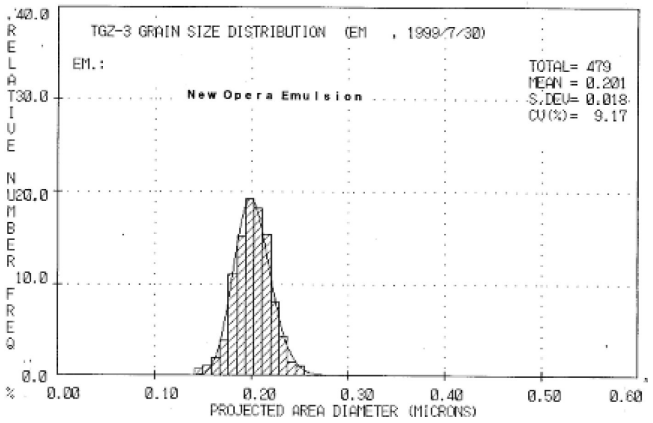

Figure 4.2: Crystal diameter distribution of the Fuji emulsions which will be produced for the OPERA experiment.

stitial silver ion encounters a trapped electron, the charges are neutralised and an atom of metallic silver is formed. In this way a stable nucleus of four or more atoms of silver can be built up. The site is then known as a latent image center, and the entire crystal may be reduced to metallic silver on development.

The formation and preservation of the "latent image" depends on external conditions such as: temperature, humidity, pressure. As temperature and humidity increase, the sensitivity decreases and the "latent image" is less stable (Fading). The fading can be artificially induced in order to erase the image of unwanted tracks accumulated before the exposition (Refresh). The sensitivity of refreshed emulsion films shows no degradation.

4.2.2 Development

Photographic development is the process by which the latent image contained in an emulsion is made visible by the reduction of silver ions in the silver halide crystal to metallic silver.

For developing nuclear emulsions, a developer is chosen which reduces completely those crystals containing a latent image center, while leaving unchanged those not containing a center. The development time used for processing should be sufficient for those crystals with a latent image center to be reduced completely, but not so long that unexposed crystals are devel-

oped. In practice, a certain number of crystals will be developed even though they do not contain a latent image center. These grains, when developed, constitute what is known as fog or background.

Developing agents may be divided into two main groups, depending on the source of silver ions for reduction. In practice, most developers give a combination of the two sorts of development.

The first group is known as physical developing agents: in these, silver ions are provided from the solution in the form of a soluble complex. They are deposited on the latent image center and are reduced to metallic silver. This produces spherical particles, the precise shape of which is affected by pH.

The second group is the chemical developing agents. The choice between a physical developer and a chemical developer will largely depend on the grain structure required in the processed image. In chemical development, silver ions are provided from the silver halide crystal containing the latent image center. The action of a chemical developer produces a mass of filaments bearing little resemblance to the original crystal. If silver halide solvents such as sulphite are present in a chemical developer, an opportunity exists for some physical development to occur. In this case, the filaments in the processed plate will be shorter and thicker.

Chemical development, like many other chemical reactions, is dependent on temperature. In general, development occurs more rapidly at higher temperatures - below 10°C development virtually stops. For this reason it is important to keep the processing temperature constant during development, otherwise it will not be possible to assess the correct development time.

4.2.3 Fixation

The purpose of fixation is to remove all the residual silver halide, leaving the metallic silver to form the image. If the silver halide was left in the emulsion, it would slowly go brown and degrade the image. The fixing agents most widely used are sodium or ammonium thiosulphate, which form thiosulphate complexes with the silver halide. Silver thiosulphate is soluble in water and so may be removed from the emulsion by washing.

It is important to use a fixer which has not been exhausted when processing nuclear emulsions, otherwise some silver halide will remain in the emulsion. To ensure that it is all removed a fixing time should be used which

is twice the time it takes for the emulsion to clear.

After fixation, the emulsion must be washed very thoroughly, to remove all the silver thiosulphate complexes in the emulsion. If any do remain, they will eventually break down, forming silver sulphide which is brown and will obscure the image.

4.3 Processed emulsion

4.3.1 The "fog"

Random developed grains constituting "fog" are found in emulsion because there are always a few grains of the large number that develop as quickly as the track grains.

The number of fog grains that develop, increases linearly with the time of development, until about twice the period required for a track; if this time is extended still more, the density of fog starts to rise more rapidly. Fog produced by visible light is limited to the surface, only a thin layer of which is penetrated by the light.

Another type of fog consists of a very large number of grains so tiny as to be visible with the highest resolution: it is generally attributed to colloidal silver and has been observed to increase as the sulfite content of the developer is increased.[1]

4.3.2 Track visibility

Fog is an especially serious problem when one is making a study for which it is essential to see minimum ionizing traacks. In order to see the minimum ionizing particle in an emulsion, it needs almost 30 developed grains every 100 μm of path (Grain Density) and the accidentally developed grains concentration should be < 5 in 1000 μm^3 (Fog Density).

If the depth of field of the objective is lowered by using a larger numerical aperture, the thickness of the emulsion which is seen in focus is reduced, and correspondingly a higher ratio of fog density can be tolerated because a smaller proportion of the fog grains will be in focus. The track visibility is reduced if it is inclined, and especially if it scatters.

[1] If serious it can be easily removed by a clearing solution

4.3.3 Shrinkage factor

After processing, an emulsion will occupy less volume than before unless some material is added to replace the silver halide dissolved by the fixer. If the emulsion plate is mounted on a glass or plastic base, the most conspicuous evidence of this effect is a reduction of the thickness of the emulsion layer.

For any quantitative measurements of tracks density, ranges, and angles in the emulsion, it is important to measure the precise original thickness.

The *shrinkage factor* is the ratio of the thickness of emulsion at the time of exposure divided by its thickness at the time of scanning.

Both gelatin and glycerin are hygroscopic so that the actual equilibrium thickness (and also the index of refraction) depends on the ambient humidity. Normal processed emulsion changes its thickness with the ambient humidity in a way that is given roughly, when the humidity is near 60%, by:

$$\frac{\Delta t}{t} = \frac{RH^2}{3 \cdot 10^4}$$

where t is the nominal thickness, Δt is the increase from the dry thickness and RH is the relative humidity in per cent.

To know whether or not the emulsion is in equilibrium with the atmospheric water, repeated weighings will reveal loss or gain of water.

4.3.4 Distortions

Ideally, the processing of an emulsion should lead to a uniform contraction in thickness – in the z-direction – leaving unchanged the x,y coordinates of any points. In practice, distortions occur which limit the precision of measurements on tracks. Distortions can vary from one region of the emulsion sheet to another, but in well-processing conditions they do not change rapidly in passing over distances of the order of a centimeter.

The simplest form of general distortion is a uniform shear: straight tracks remain rectilinear but their direction and length change by an amount which depends on the magnitude and direction of the shear.

A more serious source of error is due to differential shear of the emulsion in which both the magnitude and direction of the shear change with depth. Such distortion changes the tracks of an energetic particle from a line into a curve.

In the case of emulsions mounted on a glass or plastic base, the points on tracks are assumed to be unaltered by the processing [34]. The lateral displacement in the x and y can be expressed by the distortion vector $\mathbf{k}$ (distortion are chiefly of the quadratic type):

$$\mathbf{k} = \mathbf{k_1}\frac{z}{s} + \mathbf{k_2}(\frac{z}{s})^2 + ...$$

where s is the thickness of the unprocessed emulsion and z is the distance from the displaced point to the base in the unprocessed plate, $\mathbf{k_1}$ and $\mathbf{k_2}$ are in general vectors having different directions (Fig: 4.3).

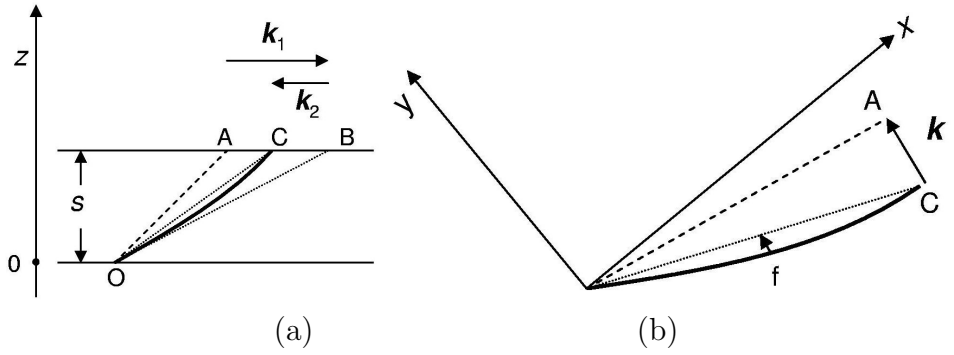

Figure 4.3: (a) Distortion scheme in an emulsion layer; OA is the track in absence of distortions, OB is the track with only linear distortion, OC is the track with total distortion; Horizontal projection of the distortions.

Since in the free surface of the emulsion (the surface between emulsion and air, where $z = s$) the direction of a track usually remains unchanged

$$\left.\frac{d\mathbf{k}}{dz}\right|_{z=s} = \frac{\mathbf{k_1}}{s} + \frac{2\mathbf{k_2}}{s} = 0$$

it is possible to find a relation between $\mathbf{k_1}$ and $\mathbf{k_2}$:

$$\mathbf{k_1} = -2\mathbf{k_2}$$

The horizontal projection of the track, as observed by an optical microscope, is shown in Fig. 4.3. It is mathematically simple to demonstrate that the distortion vector can be measured by multiplying by 4 the distance f from the middle point of the tracks to its sagitta $\mathbf{k} = 4\mathbf{f}$.

This kind of distortion changes an originally straight track into a parabolic form and is referred to *C-shaped* distortion. Less frequently and more especially near the processed edge of the emulsion, the tracks may be bent into an *S-shape*. A third type of distortion is known as *chopping* and results in violent changes in direction of the track, and lateral and longitudinal displacements of many microns

4.4 OPERA Emulsion films

The total area of emulsion films in the OPERA detector is $\sim$ 176000 m^2 arranged in $\sim$11 millions of 10x11 cm^2 plates composed of a pair of $\sim$ 40 μm thick emulsion layers, as described in chapter 3. This corresponds to 18 m^3 of dried emulsion gel.[2]

The emulsions used for the past experiments, were poured by hand following standard procedures developed in many years of experience. The same procedure applied to OPERA would be prohibitively time consuming. To overcome this problem, a R&D project has been carried out by Nagoya University and the Fuji Film company to establish the process of automatic coating of nuclear emulsion films. After several tests, it is confirmed that the OPERA emulsion film can be produced by commercial photographic film production lines. The required amount of films needed for the experiment will be produced within two years. Fig. 4.4 shows the cross sectional view of the newly developed machine-coated emulsion film.

As opposed to hand-made films, the thickness can be precisely controlled as in the case of commercial color films. The measure of the film emulsion layer thickness after development shows a distribution with $sigma \sim 1.3\mu$m.

As shown in Fig. 4.4, each film has a protective gelatin layer of 1 μm thickness on the sensitive layers. This prevents the occurrence of black or gray patterns on the emulsion surface. These patterns, frequently emerging in the case of hand-poured plates, are due to silver chemically deposited

[2]For comparison, the amount of emulsion handled for CHORUS is equivalent to a surface of 500 m^2 and to a 0.4 m^3 total volume of dried emulsion.

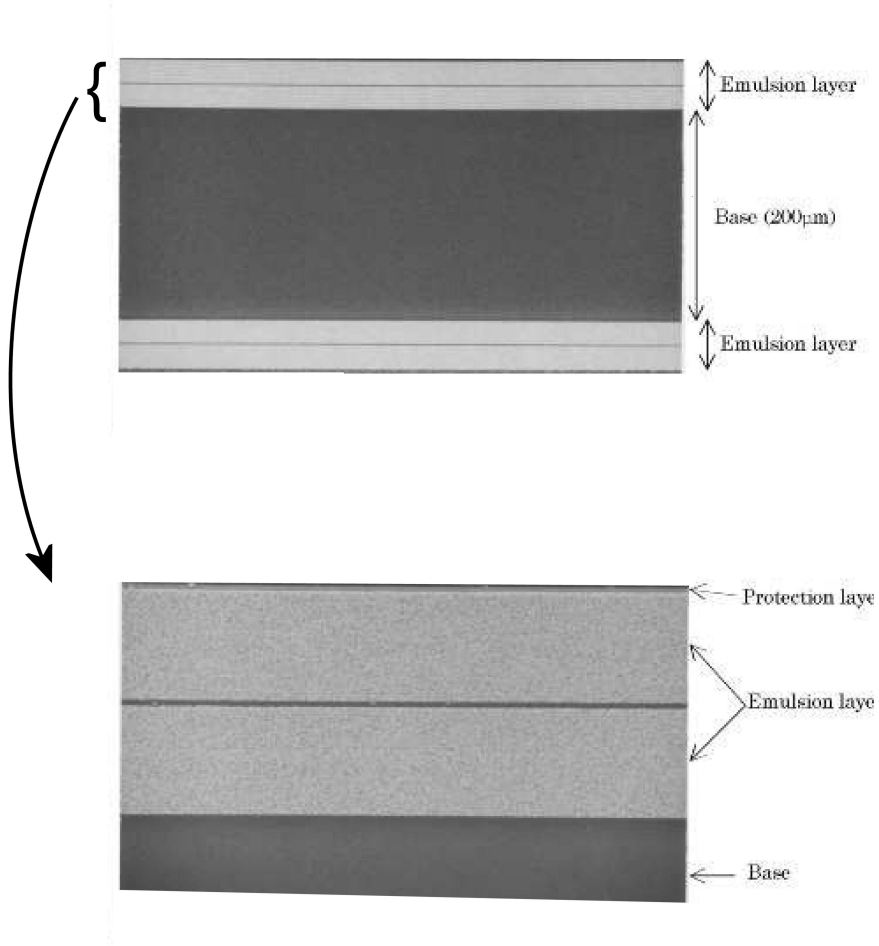

Figure 4.4: Top: photograph of the cross section of a machine-coated emulsion film. The picture was taken with an electron microscope. Diluted emulsion layers of 42 μm thickness are coated on both sides of a 200 μm thick triacetate base. Bottom: enlarged view of the top emulsion layer. A thin ($\approx$ 1 μm) protective film (gelatin) is placed over the emulsion layer at the same time of coating.

during the development. The removal of these stains had been the most time-consuming task in the emulsion preprocessing for the experiments performed so far. By means of the protective coating, surface cleaning is not needed anymore and the preprocessing procedure becomes compatible with the daily handling of thousands of emulsion films, as in the case of OPERA.

In addition, the presence of this protective layer allows direct contact with the lead plates. Without this protection, one would have to insert thin insulator sheets in order to avoid chemical reactions between the lead plates and the silver halides contained in the emulsion.

For automatic coating some dilution of the gel is required. Under normal conditions, the grain density, defined as the number of grains per 100 μm along the particle trajectory, decreases almost linearly with the dilution factor although part of the sensitivity loss may be regained in the development phase. This problem has been solved by increasing the sensitivity of each crystal using the technology of crystal growth developed for standard photographic films.

As shown in Fig. 4.2, the crystal diameter distribution in the emulsion layer is rather uniform around 0.20 μm. The currently achieved grain density of the machine-coated emulsion films is 30 grains/100 μm even in the case of a factor of two dilution.

The so-called emulsion fog is due to accidental grains randomly distributed in the emulsion volume (Fig. 4.5). They constitute a background which has to be kept at the level of ≤ 5 fog /1000 μm^3. This can be achieved by applying a moderate development to the emulsion films, still keeping a sufficient sensitivity of $\sim$ 30 grains/100 μm, as shown in Fig. 4.6.

The intrinsic position resolution of the emulsion films can also be investigated by measuring the position residuals of the centre of each grain with respect to a fitted straight line. The result is shown in Fig. 4.7. The measured resolution of $\sigma \sim 0.06$ μm can be compared with the expected value of 0.058 μm ~ 0.2 μm$/\sqrt{12}$, where 0.2 μm is the diameter of the original crystal. This result implies that the crystal uniformly grows under development up to a grain with diameter of ~ 0.6 μm.

The physics properties of the emulsion layer are the following: density ρ = 2.40 g/cm^3, average atomic number $< A >= 18.2$, average atomic charge $< Z >= 8.9$, radiation length $X_0 = 5.5$ cm, $(\frac{dE}{dx})_{mip} = 1.55$ MeV/g/cm^2 or 37 keV/100 μm, nuclear collision length $\lambda_T = 33$ cm and nuclear interaction length $\lambda_I = 51$ cm.

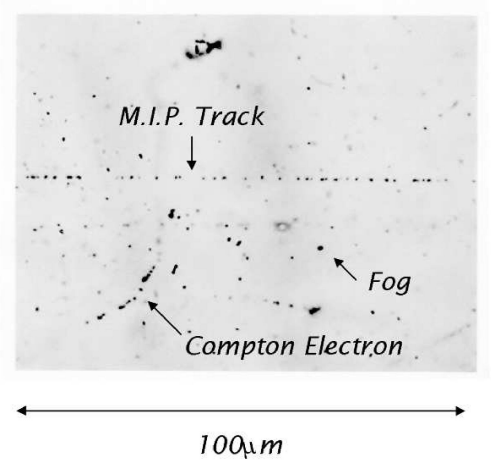

Figure 4.5: Photograph of a minimum ionising particle (mip) recorded in an emulsion layer. The grain density is defined as the number of grains per 100 μm track; the fog density as the number of fog grains per 1000 μm^3,

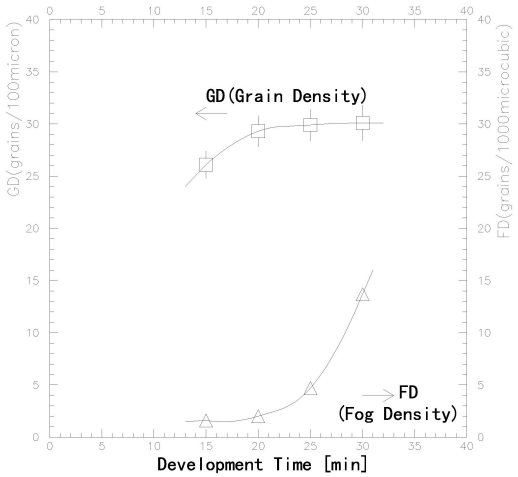

Figure 4.6: Time dependence of the developed grain density and fog density. Conditions are: amidol developer at 20C. A development time from 20 to 25 minutes gives satisfactory results.

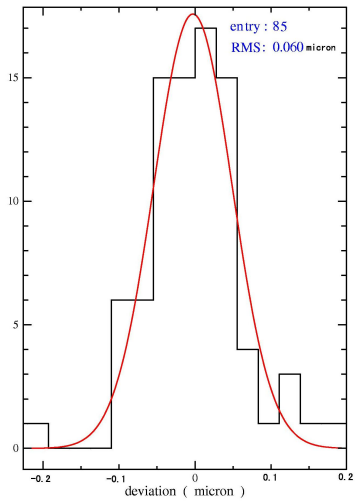

Figure 4.7: Position residuals of the grain center with respect to a fitting straight line.

The base material of the films is cellulose triacetate (TAC), which is one of the commonly used base materials for photographic films. Its physics properties are: density $\rho = 1.28$ g/cm^3, optical index n = 1.48, radiation length $X_0 = 31$ cm, nuclear collision length $\lambda_T = 47$ cm and nuclear interaction length $\lambda_I = 67$ cm.

Emulsion film distortions have also been investigated. As shown before distortion is a phenomenon which shifts the position of the recorded trajectories in the emulsion layer because of stresses accumulated in the gelatin layer. In hand-made emulsion plates, shifts of several μm are frequently observed, caused by a disuniform drying at the plate production.

The distortion can affect the efficiency in connecting two micro tracks in the two emulsion layers of a film, however the base tracks constructed with connected micro tracks have positions and angles not affected by distortion. They are actually used in most of the analyses foreseen for OPERA.

Fig. 4.8 shows the typical distortion pattern in the central part of an emulsion film. The distortion effect is very much suppressed in industrial films down to ~ 0.4 μm. This result is due to the uniform drying process at the production and also to the careful development treatment specially devised for OPERA.

Usually the distortion becomes larger near the edge of the film. In the

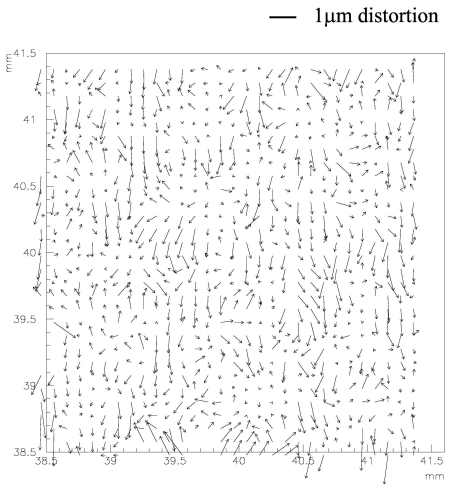

Figure 4.8: Measurement of the emulsion distortion at the centre of an emulsion film (from the OPERA proposal). The scanning area is ≈ 3 mm x 3 mm. The vectors indicate the distortion direction. The absolute value of the distortion is indicated by the length of the arrow.

case of OPERA emulsion films, the distortion is lower than ~ 1 μm up to 1 mm from the film edge. Only at about 100 μm from the edge the film is completely damaged, due to black stripes caused by the pressure applied at the film cutting.

The fading and aging features of the industrial emulsion films have been investigated. Fading is the loss of the latent image occurring prior to development. Aging is the degradation of the emulsion sensitivity during the exposure.

Fading is not a severe problem for this experiment, since we plan to extract the selected brick and develop the emulsions within one week after the event occurred. Within about one month, possible extra bricks required for further analysis (candidate events) are extracted and developed. Moreover, one can take advantage of the existence of some fading, which contributes to erase unwanted cosmic ray tracks accumulated during film production and transportation before the run, as described in the next Section. This feature is beneficial to suppress the degradation of the electron identification efficiency and obtain an adequate energy resolution for cascade showers. In

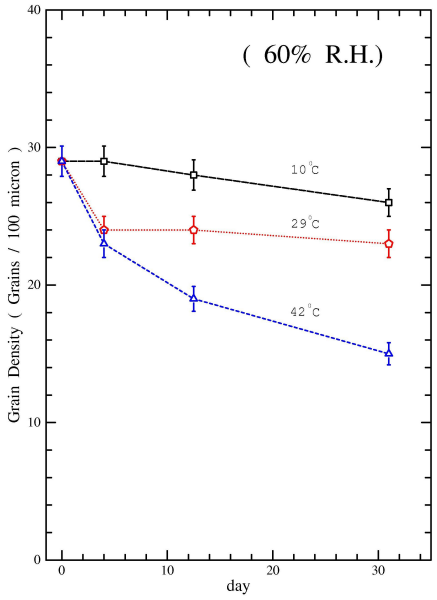

Figure 4.9: Example of fading. Each film is packed at 60% R.H. and 20°C. After a beam exposure, the samples have been stored at different temperatures. At 10°C the time needed to reduce the grain density to 25 grains/100 μm is estimated to be 1.5 to 2 months.

principle, the fading time constant depends on the environmental temperature, humidity and on the oxygen density. One example of these properties is shown in Fig. 4.9. According to the film producer, fading properties are well under control.

In order to check the features of the Fuji emulsion in maintaining their sensitivity with age, tests on sensitivity has been performed by exposing all plates of emulsions to an electron beam and by developing them soon after. The results are that even the oldest plates still show enough sensitivity, i.e. $\geq$ 25 grains/100 μm. The situation is even better for OPERA, since the natural temperature of the Gran Sasso hall is appreciably lower. Therefore, the OPERA emulsion sensitivity will be preserved over their (maximum) 7 years lifetime (i.e. 2 years for production and 5 years for exposure).

Chapter 5

The automatic system for emulsion scanning

5.1 Introduction

Nuclear emulsions have been used for more than 60 years in nuclear and particle physics and are connected to many major discoveries, as for example the pion decay in 1947, etc, ...

The amount of emulsion used in the early experiments was relatively small and the measurements were made manually: human observers operated the microscope by moving the stage, adjusting the focal plane of the objective, and examining a magnified image of tracks in nuclear emulsions through the eyepieces.

Later, the stage was motorized and the image made available also on a TV screen; often the stage control and the image analysis performed by the operator were assisted by a computer (semi-automatic systems).

Because of the limit in human resources for scanning and the intrinsic slowness of the data readout which made difficult the management of large masses, the use of nuclear emulsions has gradually decreased after the development of electronic detectors.

On the other hand, significant improvements in the emulsion technique and recent developments in computing and electronics for fast data acquisition, have given the possibility to plan and realize very large detector also based on emulsions: for example, the increased sensitivity, the packaging method, the industrial production, the scanning and measuring instrumen-

tation.

Automatic scanning allows for fast extraction of physical information from emulsion sheets, after they have been exposed to particle radiation. Not only does it make handling of large data sets possible, it also ensures that physics results can be produced shortly after the running of the experiment.

The pioneering work in automatic scanning has been done by the the University of Nagoya (Japan) and a first complete application of the automatic system was used for the CHORUS experiment data analysis in the '90s [36]; the so-called Track Selector has been designed to detect tracks with predicted angle in the field of view of a CCD camera.[1] The track recognization algorithm, based on tomographic images taken at different depth, is completely implemented on hardware: tracks are extracted by shifting horizontally the images to find coincidences.

European groups followed a different approach, initiated by the Salerno group for the CHORUS experiment [37], based on multi-track reconstruction regardless their slope. Guidelines of this project are the use of the state-of-art commercial products both for hardware and software and the flexibility of the software tracking algorithm, to obtain a system easy to be upgraded following the rapid technological progress.

In this chapter the basic principles of automatic readout of emulsion films and image processing are briefly explained and a prototype installed by the Bologna group for the OPERA experiment is described.

5.2 The principle of automatic scanning of emulsions

Conceptually, a microscope for automatic emulsion scanning consists of a computer driven mechanical stage, appropriate optical system, a photodetector -typically a CCD camera- and its associated readout as shown in Fig. 5.1.

During the acquisition, the emulsion is scanned view by view by the camera and the images are sent to the frame grabber hosted in a computer, which also controls the light intensity and the stages displacements. In particular the readout is performed by moving the best focus plane of the objective

[1] The system uses a grabber board connected to a CCD Camera (512 x 512 pixel at 120 Hz frame rate) and a Fast Programmable Gate Array (FPGA) for image processing and tracking. The area of the view is $\sim 150 \times 150\ \mu m^2$.

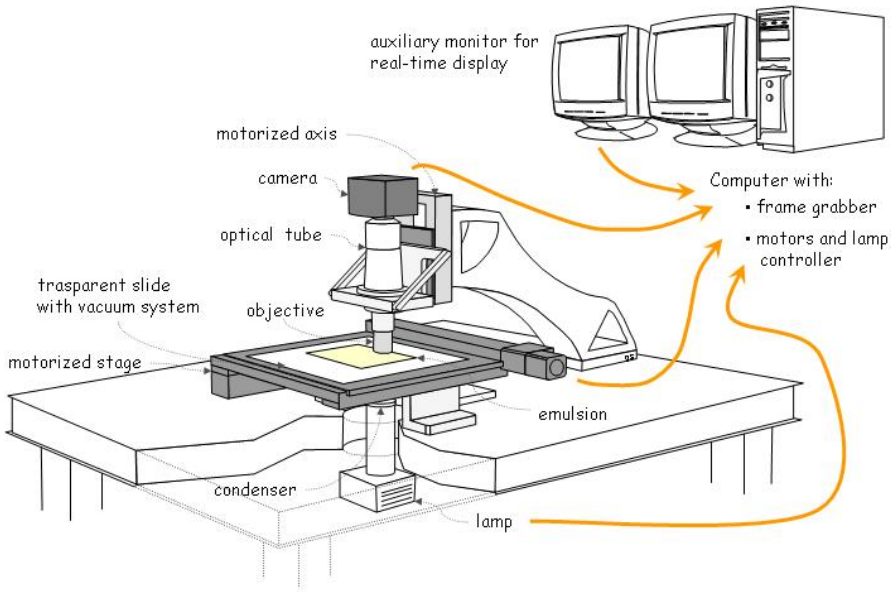

Figure 5.1: Layout of the components of a typical automatic scanning system for nuclear emulsion.

inside the emulsion layer with constant speed and, for each field of view, a series of successive vertical images is taken by the camera, (Fig. 5.2).

The vertical speed of the optical axis v is determined by the the frame rate of the camera fps, the thickness of emulsion S and the number of layer to be grabbed n:

$$v = \frac{S \cdot fps}{n}$$

The number of layers must be sufficiently high to allow good recognition of tracks and the distance between consecutive layers Δz is a critical parameter because it should be small enough to not lose grains but larger than the depth of view of the objective in order to not acquire the same grain in too much layers. Since the grain density of a minimum ionizing particle is about 30 grains per 100 μm in an unprocessed emulsion and the depth of view $\approx 0.5 \div 2$ μm, the number of layer must be chosen to have a layers distance of:

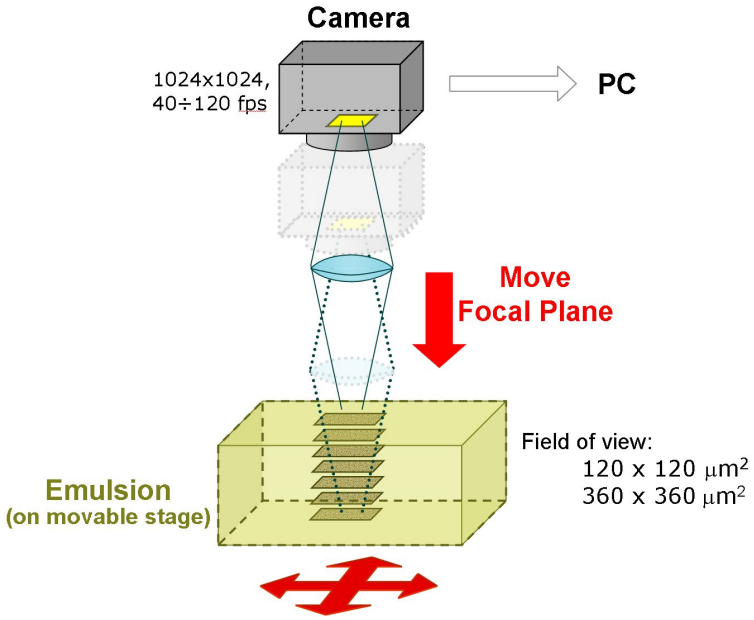

Figure 5.2: The readout: for each field of view several tomographic images of the emulsion are taken by moving the optical axis.

$$\Delta z = S/n \approx 2 \div 3 \quad \mu\text{m}$$

For example, if $S = 40$ μm, $n = 16$ layers and $fps = 40$ frames per second, then the vertical speed is $v = 100$ μm/s and the distance between consecutive layers is $\Delta z = 2.5$ μm.

Grains belonging to different layers are then searched to form a straight line (Fig. 7.13).

5.3 Image handling

The image is digitized and converted to a gray scale of usually 256 levels (0 = black, 255 = white), Fig. 5.4. Digital images are analyzed for the recognition of the dark spots (*clusters*) in the image: some of these spots are track grains of the emulsion; most clusters are spurious grains, not belonging to tracks but physical existing in the emulsion (the so-called fog grains); some clusters

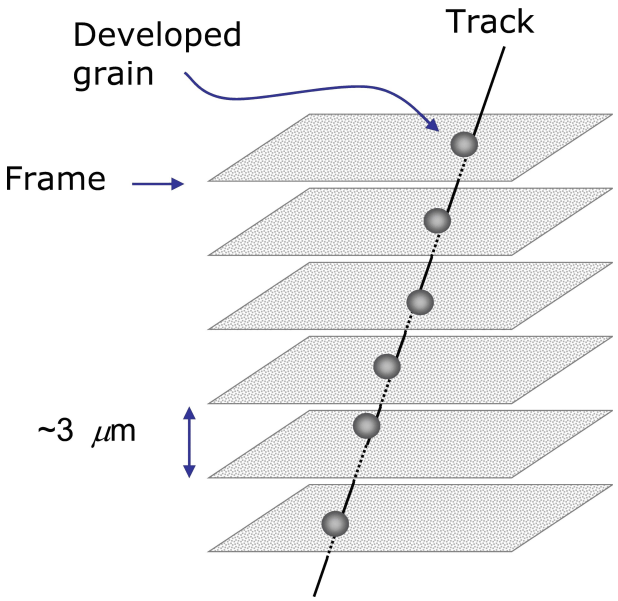

Figure 5.3: The track is found by connected grains in each layers.

come from noise in the electronic signal.

Often the image of the emulsion is not very clear due to shadows caused by grains that are not in the focus plane or to scratches and dirt. Hence, a **convolution** filter is used to enhance the contrast between focused grains and background. An example is a 3×3 high pass filter kernel:

-1	-1	-1
-1	9	-1
-1	-1	-1

Convolution is a local operation: the output value v_{ij} of the pixel at a specific coordinate is a weighted sum of the input values of the neighborhood pixels, the weights w_{lk} are given by the filter kernel; for a 3x3 kernel:

$$v'_{ij} = \sum_{l=-1}^{+1} \sum_{k=-1}^{+1} w_{lk} v(i-l)(j-k)$$

Then a well-chosen **threshold** is applied to extract the dark spots that are candidate to become grains; the pixels are divided in two classes: the ones

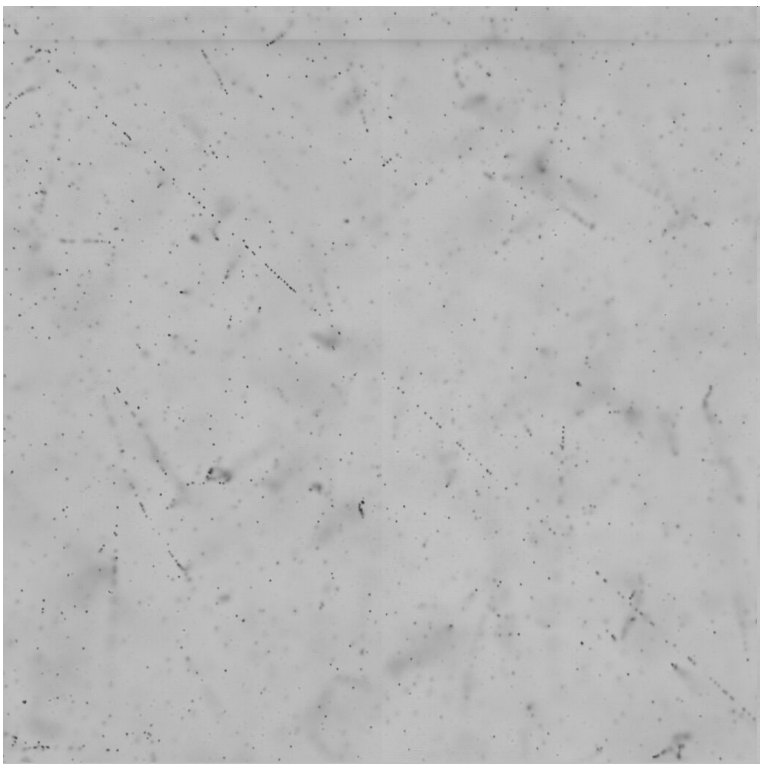

Figure 5.4: An image showing a typical emulsion view; a magnification of 50x is applied, the image sensor size is 1024×1024 pixels and the field of view 244×244 μm^2.

with the filter response above threshold, whose values in binarized image are set to 0, are the "white" pixels, and the ones with filter response below the threshold whose values are set to 1, are the "black" pixels.

In Fig. 5.5 and Fig. 5.7 the results of the processing of the grains and of a large area of the image are shown.

The last step of image processing is the **clustering**: the image is scanned row by row. Each sequence of black pixels found is called "segment" and stored in memory; this process is the most time-consuming, because it has to deal with huge amount of data. After a row has been scanned, the segments are compared with the segments in the previous row and adjacent segments are merged into a cluster. If two or more clusters come in contact, they are also merged. Finally, position, area and shape of clusters are given as results.

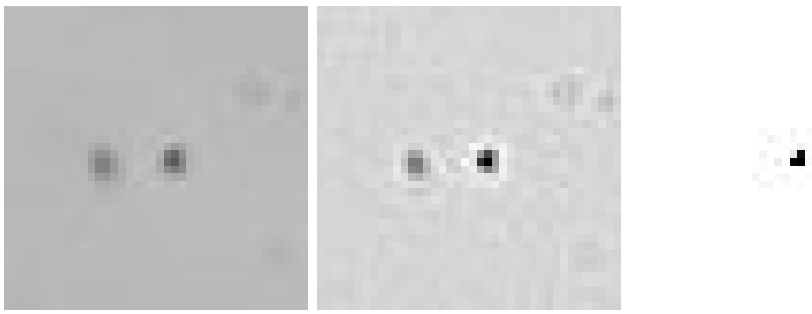

Figure 5.5: Image processing steps of an image with two grain at different focus. The first picture shows the grabbed image, the second the effect of the high pass 3×3 filter and the last the effect of the threshold. The second image has been scaled to have a 256 gray levels image and to be properly displayed.

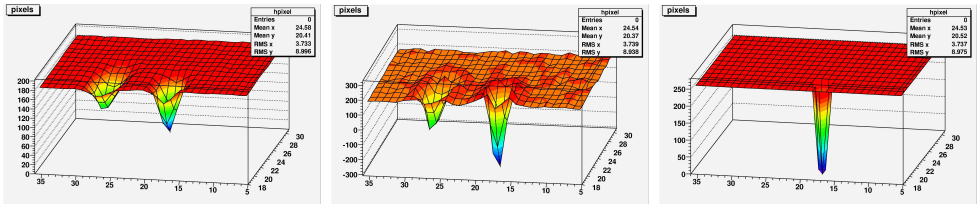

Figure 5.6: The three histograms show the effect of image processing in the gray levels distribution of the upper images. The effect of convolution extends the value outside the region where an image can be correctly displayed (0-255), so the threshold can be also negative.

Depending on the illumination and the processing parameters, small clusters, i.e. composed by only 1 pixel, can be discarded since they are mostly due to the noise in the camera signal.

5.4 Track Recognition

The following step consists in combining grains from different layers to recognize geometrical alignments. The tracking efficiency can be affected by distortions of the track, then the algorithm must take into account this phe-

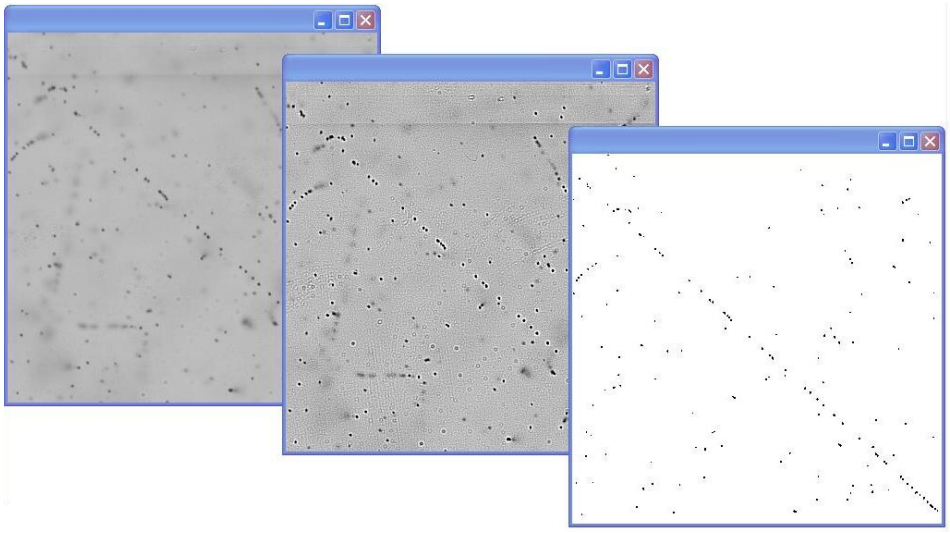

Figure 5.7: Image processing on a large area of the image: grabbed image, high pass filter and threshold.

nomenon.[2]

The field of view is subdivided in cells about 20 μm wide. Local alignments of grains are then detected within each cell and across boundaries of neighbouring cells.

The search starts from a combination of all the grains in two distant layers and then requires some aligned grains in the inner layers (**track startup**), Fig. 5.8; the requested alignment tolerance and the layers to use in this phase are depends on the feature of the emulsions and on the quality of the track to be searched for.

When such an alignment is found, the computer looks for more aligned grains in the cell of the next layers which is predicted by the track fitting, (**track following**). The following phase stops when one or more empty layers are found.

While a track is being built, it may cross some already existing track. In

[2]The tracks should be straight; but due to the developing process, straight tracks are turned into parabolas: the point lying at the interface between the emulsion and its support remains in its original position, and the slope of each track at its exit point in air is left unchanged. In any case, since the OPERA emulsion are very thin, distortions vector could be small and the effect not dramatic.

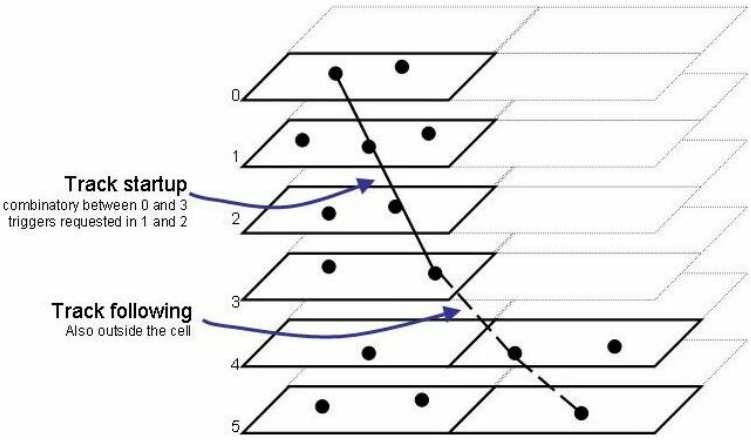

Figure 5.8: The tracking algorithm. Track startup takes place only in a cell stack to reduce computing time. Track following phase is allowed to change cell stack.

this case, if the tracks share three consecutive grains, they are joined together in a single entity.

When a track stops both in the upward and downward directions, the number of points collected is compared with a minimum threshold (for example 8 points), required to store the track in the final data array.

5.5 Track Postprocessing

After all the tracks in a field have been recognized, they must be corrected for geometrical distortion.

The tracks that pass the whole thickness of the emulsion layer are used to estimate the distortion vector, which is then used to correct the positions of the grains of all the tracks in the current field. This correction relies on the assumption that the slope at the exit point is the original one [42], Fig.5.9. Sometimes this is not exactly true, and gives rise to some systematic deviation of the computed slopes from the real values. However, this kind measurement error is not unrecoverable, and also an off-line correction is possible. Another requirement is that the point lying at the interface between the emulsion and its support remains in its original position.

As already stated, emulsions shrink during the developing process. So,

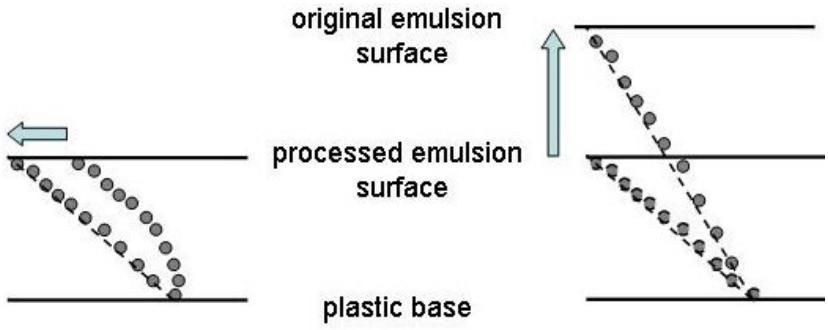

Figure 5.9: Distortion corrections applied to the reconstructed tracks.

when they are scanned, the thickness is usually less than of the original one. The reconstructed tracks are then "expanded".

Finally, for each tracks some global parameters are calculated: slope, intercept with the emulsion base, standard deviation of the grains to the fitting line

The process described above is repeated for each of the two sides of the emulsion. When this process is over all the tracks in the scanning field are reconstructed without any selection in slope so that the whole information present in the emulsion is stored and available for the analysis.

5.6 The prototype in Bologna

A photograph of the prototype installed by the Bologna group is shown in Fig. 5.10.

Since precision optical measurements depend on reliable position stability, the microscope is mounted on a Mellios Griot high quality breadboard which provides a virtually rigid and vibration-free working surface that hold the components in a fixed relative position.

The legs supporting the tabletop includes an air suspension mechanisms to reduce vibrations. The tabletop is stiff but light. Stiffness ensures that the tabletop has few mechanical resonance's and internal dampers built into the tabletop suppresses remaining vibrations, particularly from shock and movement generated on the table surface.

A Micos MS-8 scan table with 20.5x20.5 cm^2 range on horizontal directions is mounted on the tabletop. The stage horizontal coordinates are read

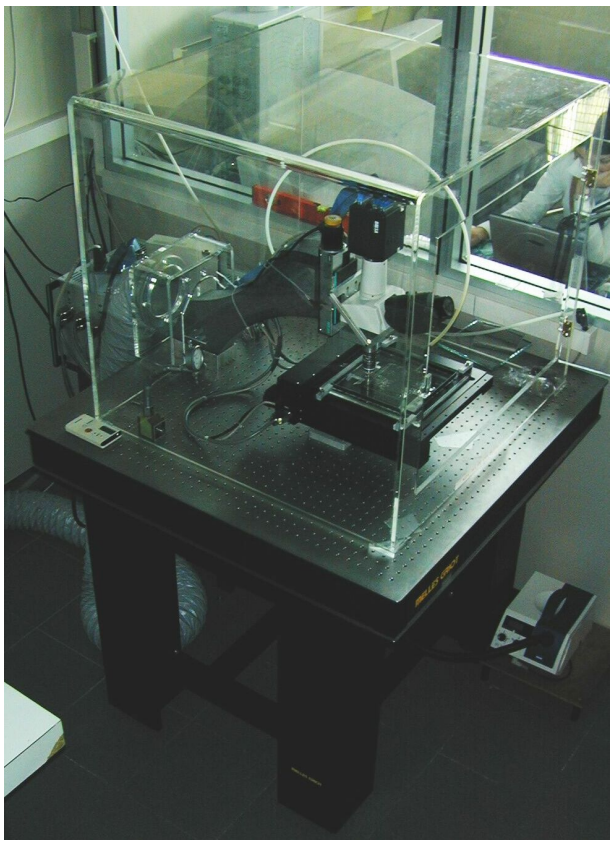

Figure 5.10: The prototype of automatic scanning system for emulsion realized in the Bologna laboratory.

out by two linear encoders with an accuracy of 0.1 μm. The limit switches are integrated in the scan table.

The vertical linear stage is mounted on a granite arm as shown in Fig. 5.11. The model is a Micos MT-85 stage. The vertical position is read out by integrated linear encoder with an accuracy of 0.1 μm. The limit switches are integrated in the stage, but the lower one has been modified and substitute with an optical switch based on a photodiode to have a better precision and to avoid that the objective scratches the emulsion. It can also be tuned depending on the thickness of emulsion.

A vacuum pump helps on keeping the emulsion sheets flat on the stage glass.

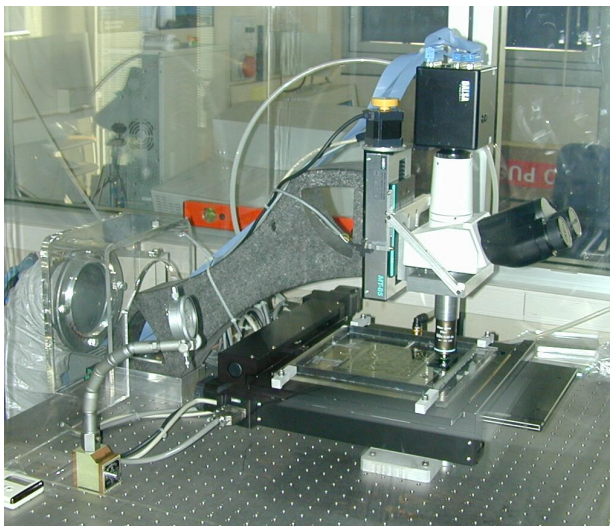

Figure 5.11: Mechanics and optics mounted on the tabletop.

Both vertical stage and scan table are equipped with the steppers motors model NanoStep RFK Series 5-Phase Microstepping Systems produced by Vexta. Stepper motors are excellent for precise positioning control; some of the typical disadvantages of stepper motors in comparison with servo motors are negligible because of the usage of microstepping units and feedback with linear encoders (closed-loop).

The stage controller is a FlexMotion board provided by National Instruments and is inserted into the host PC.

Optics is composed by the objective, trinocular and the mounting tube from Nikon manufacturer. Because this part of the microscope is the core of the system, the requirements and the set-up are detailed described in the next chapter.

A high-resolution CCD camera (model Dalsa CAD-4) is mounted on the end of the optical tube on the microscope. Its frame rate is 40 Hz and the CCD sensor is 1024x1024 pixels. Images acquired by the camera are sent to a frame grabber, hosted in the DAQ PC.

The frame grabber and vision processor is a Matrox Genesis with1 Digital Signal Processor (DSP). This board is equipped with a Neighnorhood Operation Acceleration (NOA), a Matrox custom. Up to six board with 2 DSP and 2 NOA can work together to analyze the image. The grab port can acquire

from digital camera up to 1.28 Gbit/s. The system is capable of filtering, digitising and clustering one frame in less than 10 ms. The time needed to analyze a complete field (both emulsion sides) would be less than 300 ms. The tracking is performed in parallel to the main acquisition sequence.

The DAQ PC has an AMD Athlon processor running at 1500 MHz. An auxiliary monitor connected to the display memory of the frame grabber to see the image coming from the camera is also used.

Chapter 6

The set-up of the optical system

Of the greatest importance to this research program is the optical design and set-up: the features and the quality of the objective should match the requests of the scanning procedure; the alignment of light source, diaphragms and condenser must be good; the intensity and the color the light must should be adjusted to obtain the maximum contrast of the image, and so on.

6.1 The requirements for scanning emulsion sheets

6.1.1 Objective

Emulsion sheets have emulsion layers on both sides of a transparent plastic base whose is 200 μm. The thickness of the emulsion layer is $\sim$ 42 μm and can decrease after the processing (up to 30 μm).

Since the order of magnitude of the pixels size of megapixels cameras is about 10 μm and the the size of processed grains is about 0.8 μ, in order to have a resolution of a few pixels for each grains, the total *Linear Magnification* of the image should range from 40:1 to 60:1 (corresponding respectively to about 3.2 pixels/grain and 4.8 pixels/grain).

Several tomographic images of both the emulsion layers are taken by the automatic system. Hence, the *Working Distance* (WD) of the objective

should be at least 300 μm to see the back side of the emulsion.[1]

The thickness of emulsion sheet between the focus plane and the front lens of the objective is variable and depends on the height where we take the image: from 0 at the top surface of the emulsion to 280 μm at the bottom surface.[2]

Moreover the *Numerical Aperture* (NA) of the objective should be more higher than possible, as is explained below, and, since the spherical aberration[3] increases as the cube of NA, the variation of the intermediate medium, between objective and focus plane, which we can tolerate, is only ± 20 μm. For this reasons, the use of *dry* objectives is seriously compromised, because of the refractive index of the imaging medium should not be constant; hence, the choice of *oil-immersion objective* is forced.

Typical immersion oils have a refractive index of 1.51, so light rays passing through the emulsion sheet encounter a quite optically homogeneous medium because the refractive index of emulsion and plastic base are respectively: $n_{\text{emulsion}} = 1.51 - 1.52$ and $n_{\text{base}} = 1.48$; this is referred to *Homogeneous Immersion*[4] (HI).

Another important features to be considered is the longitudinal resolution or *Depth of Field* (DOF), which is the axial range through which an objective can be focused without any appreciable change in the image sharpness.

Inside the emulsion, in order to measure with high accuracy the distance z between grains and the surface and the horizontal coordinates x and y, the DOF should be as low as possible. This value at high numerical aperture is

[1] The Working Distance (WD) is the distance between the objective front lens and the best focus plane. If the objective is designed to work when the specimen is covered by a cover glass, the WD is the distance from the front lens and the cover glass. The WD decreases as the magnification increases.

[2] A *dry* objective is designed to minimize the aberrations considering a fixed thickness of air between the front lens and the best focus plane and, mostly, the standard thickness of the cover glass (0.17 μm with refractive index of 1.515)). When using high magnification dry objectives, cover glass thickness variations of a few micrometers result in dramatic image degradation due to wrongly corrected spherical aberration.

[3] The *transverse* component of the spherical aberration, that is the diameter of the circle of least confusion generated by the aberration.

[4] Other techniques with different liquid imaging media, such as water (n=1.33), glycerin (n=1.470), methylene iodide (n=1.740), ... are not suitable because of the high difference of the refractive index.

determined primarily by wave optics[5] and is given by the formula:

$$\mathrm{DOF} = \frac{n\lambda}{\mathrm{NA}^2}$$

where λ is the wavelength of illumination, n is the refractive index of the imaging medium, NA is the objective numerical aperture, that is the angle between the microscope optical axis and the direction of the most oblique light rays captures by the objective(angular aperture) multiplied by the refractive index of the intermediate medium: $\mathrm{NA} = n \sin\alpha$. When the numerical aperture of the condenser is not the same as the objective, the arithmetical mean should be used:

$$\mathrm{NA} = \frac{\mathrm{NA}_{obj} + \mathrm{NA}_{cond}}{2}$$

Notice that the DOF shrinks inversely with the square of the numerical aperture, so to reduce the DOF, objective with high NA should be used.

For example if $n = 1.515$, $\lambda = 550$ nm, NA= 0.9 then DOF$\approx$ 1.0 μm.

The last crucial point is the *Resolution* (R), that is defined as the smallest distance between two points on a specimen that can still be distinguished two separate entities and is given by:[6]

$$R = 0.61\lambda/\mathrm{NA}$$

Using the previous values of λ and NA, the optical resolution is $R = 0.42$ μm.

6.1.2 Substage condenser

It is critical that the condenser light cone be properly adjusted ti optimize the intensity and angle of light entering the objective front lens. The settings of the condenser's aperture diaphragm, along with the aperture of the objective, determines the *realized* numerical aperture of the microscope system, and, consequently, the resolving power.

[5] It derives from a *Rayleigh criterion*: the minimum resolved distance is when the optical path distance between the two waves (focused and not-focused) is equal to $\lambda/4$.

[6] The resolution can be expressed by another *Rayleigh criterion*: it is the radius of the circle of least confusion which is the image generated by the objective from a point-like source. When all the aberrations of the systems are corrected, it is the central disk (Airy disk) of the diffraction pattern of the point.

Commonly, only the NA of the objective is considered for calculations. In this case, the formulas are valid only if the numerical aperture of the condenser is (almost) equal to the one of the objective and the *Köhler illumination* is realized.[7]

Most commercial offers dry condenser with NA up to 0.90 and condenser for Homogeneous Immersion (to be used coupled with HI Objective) with NA up to 1.4, but an important consideration is the thickness of the microscope slide, which is crucial to the condenser as coverslip thickness is to the objective: a microscope slide of 1.20 mm is too thick to be used with most high numerical aperture condensers, that tend to have a very short working distance.

There is a mechanical limit: emulsion sheet are large (100 * 120 mm^2) and very thick (280 μm), so at the scanning stage, each film is tied onto the microscope stage with vacuum sucking. The system is realized on a plexiglass slide with 8 mm of thickness and n=1.515. So, it not possible with normal condenser to put the vertex of light cone produced by the condenser into the emulsion film. It needs a condenser with high Working Distance[8]

In our case, we need a condenser with a WD at least of 5.3 mm (which into plexiglass becomes $5.3 \cdot 1.515 = 8$ mm, plus the thickness of a standard slide of the 1 mm).

6.2 The design choice

The requirements of the system allow to exclude most of manufacturers and reduce the choice to the following objective:

Nikon CFI Plan Achromat 50x oil, NA 0.90, WD 0.4 μm, $f_{\text{obj}} = 4$ mm
,

[7]The Köhler illumination technique is recommended by all manufacturers because it can produce specimen illumination that is uniformly and free from glare, thus allowing the user to realize the microscope's full potential. The condenser is adjusted in order to project in the best focal plane of the objective, an image of the field-diaphragm. When the condenser is not in focus, due for examples to mechanical limits, only a fraction (the paraxial) of the emerging ray light could enter the objective front lens and realized numerical aperture decreases.

[8]in the case of condenser the Working Distance is usually the distance between the front lens of the condenser and the lower surface of 1 mm thickness slide.

which must be used in *infinity-corrected systems* (ICS). The objective is designed so that light emerging from the rear aperture is focused to infinity, and a second lens, known as *tube lens*, form the image at its focal plane ($f_{\text{tube lens}} = 200$ mm).

6.2.1 Magnifying Power

The Magnifying Power (M) produced by an infinity-corrected objective is calculated by dividing the reference focal length (tube length) by the focal length of the objective and is obtained using the formula:[9]

$$M = \frac{f_{\text{tube lens}}}{f_{\text{obj}}} = \frac{200}{4} = 50\text{x (nominal)}$$

where f_{obj} is the objective focal length and $f_{\text{tube lens}}$ is the tube lens focal length ($f_{\text{tube lens}} = 200$ mm for Nikon microscopes).

The magnification M can be also measured as ratio between the image sensor size and the field size of the image viewed by the sensor:

$$M = \frac{\text{sensor size}}{\text{field of view}} = \frac{12000 \quad \mu\text{m}}{244 \quad \mu\text{m}} \simeq 49.14$$

which is almost equal to the nominal one.

6.2.2 Other specifications of the objective

The numerical aperture of this objective is NA=0.9 which has a calculated depth of field DOF=1.0 μm and a resolution R=0.42 μm. The angular aperture in oil is 64.2 degrees.[10]

The working distance is WD=0.4 mm which is enough compared to the thickness of the emulsion. The requirement of a long working distance has

[9] Since the objective produces a flux of parallel light wavetrains imaged at infinity, the definition of Lateral Magnification (M) as ratio of segments between the image plane and object plane as used in finite optical system, is non-sense; so in the case of ICS it needs to use this formula suggested by E. Abbe which is a ratio of angles.

[10] That are theoretical values, but DOF, resolution and angular aperture depends also by the condenser numerical aperture; considering the actual system which use a condenser with NA=0.65, the realized values are DOF=1.6 μm and R=0.46 μm.

excluded objective with higher numerical aperture which are more advantageous in terms of DOF, resolution and brightness.

The immersion oil has a refractive index almost equal to the emulsion's one, and allows the objective to focus emulsion layers at different depth without a dramatic change in the refractive index.

Concerning the degree of correction of longitudinal chromatic aberration and field curvature, the objective is a Plan Achromat type which means that is corrected for axial chromatic aberration in two wavelength (red and blue) that are brought into the same focus; when focus us chosen in the red-blue region of the spectrum, images will have a residual of a green halo. The objective is also flat-filed corrected that yields flat images.

In this type of objective the chromatic difference of magnification or lateral chromatic aberrations is completely corrected inside the objective (Chrome Free Infinity, CFI).[11]

It is very important to stress that, using a *Chrome Free* objective permit to put the camera directly on the tube lens without intermediate lens to correct chromatical aberration.[12]

6.2.3 The Camera

The camera used is a DALSA CAD-4 with a monochromatic CCD sensor 1024x1024 pixel at 40 frame per second.

The sensor size is 12 x 12 mm^2 (the diagonal is 17 mm), which permits to exploit most of the intermediate image of the objective (the *field number*[13] of the objective is 22 mm) and the entire resolution of the objective.

[11] Many objectives, designed in according to the rules of G.B. Amici (1816) have a lateral chromatic in the front lens which cannot be corrected inside the the objective, so they need compensating eyepieces for the correction as suggested by Abbe (1886). In recent year, thanks to the technological progress in producing special glasses, modern microscope objectives have their correction for chromatic difference of magnification either build into the objectives themselves.

[12] Moreover, every air-glass surface interposed between the object and the sensor causes a little photometric leakage due to a fraction of reflected light and a little reduction of the contrast due to diffusion.

[13] The *filed-of-view number* of simply *field number* is the diameter of the viewfiled expressed in millimeters and measured at the intermediate image plane. The field of view of the specimen becomes the field number divided by the magnification of the objective.

The measured field of view (FOV) is:

$$FOV = 244 \quad \mu\text{m}$$

and the resolution of the sensor is

$$r = \frac{244 \quad \mu\text{m}}{1024 \quad \text{pixels}} = 0.239 \quad \mu\text{m/pixels}$$

which is almost an half as the objective one.

6.2.4 The condenser

As in the case of the objective, the choice of the condensers has been affected by the requirements on the working distance and by the commercial offers; the unique condenser, with the right working distance, is a Nikon Achromatic Condenser with only NA=0.65. In this case, the illumination cone is insufficient to provide the best performance of the objective. Since the condenser is not aplanatic the spherical aberrations is not corrected.

The condenser is mounted on a adjustable vertical stage for focusing.

6.2.5 Illumination

Due to the low numerical aperture of the condenser, the setup of illumination has to exploit it as better as possible:

- the iris diaphragm incorporated below the condenser is completely open;
- the focus of the condenser is put in the emulsion plane with high accuracy;
- a diffusive filter (frosted glass), located just below the condenser, is used.

The diameter of the diffuser should be bigger than the diameter of the iris diaphragm (otherwise it reduce the aperture of the cone light). Its best location is closed to the iris diaphragm because it is a plane optically conjugated to the rear focal plane of the objective and so, the irregular surface of the diffuser will not focused in the object plane.

The use of the diffuser gives the advantage of a more homogeneous of the light entering the condenser and therefore the intensity of light cone produced. In this case the effects of spherical aberration (the condenser is not aplanatic) are minimized.[14]

The presence of a diffuser does not allow to the (eventual) field diaphragm to be imaged in the object plane e therefore to realize a perfect Köeler illumination system, but a better exploitation of the condenser aperture has improved the axial resolution.

This setup has been obtained by comparing the quality of both the image of the object in the eyepiece and the image of the objective rear focal plane observed by the means of an auxiliary telescope.

6.2.6 The light source

The requirements for the light source are more simple because of the use of the diffuser: it only needs that the brightness is adapt and the diffuser is illuminated homogeneously. It avoid also a fine adjustment of the position, inclination, and so on.

Since it is useful remote controlling, we are using the Schott KL2500LCD light source with a 10 mm diameter fiber optics which is located 200 mm below the condenser. This system also has a revolver for interferential bandpass filters.

6.3 Tests of the quality of optics

6.3.1 Field curvature and geometrical distortions

The field curvature and the geometrical distortions are aberration of the focal plane and has been studied by using a grid pattern with 10 μm step (provided by Graticules Ltd). Moving the automated mechanical stage is possible to change the focus plane with a precision of 0.1 μm.

The difference of the objective distance from the specimen when respectively the center of the grid and the border are in focus is less than 0.5 μm: so the objective is essentially flat-field.

Geometrical distortions (pincushion or barrel) have not been observed.

[14]Since it is not aplanatic, oblique light rays emanating from the condenser are focused below than the paraxial light rays.

6.3.2 Chromatic aberrations

The evaluation of aberrations are conducted by utilizing specific test pattern targets (*star test*) consisting of an aluminum coated slide with a series of holes of different size. The observation is made usually under high light intensity.

Choosing an hole whose geometrical image is less the diffraction pattern and moving this hole in various points of the field of view, it is possible to see the defect of the pattern caused by aberrations.

Chromatic aberrations is the result of the inability of the lens to bring all of the color components of the light into a common focus. Since the camera is monochromatic, to properly detect this kind of effect, we have observed the image directly in the eyepieces.

Longitudinal chromatic

By observing an hole in the center of the field and moving the objective above and below of the best focal plane, it could appears some colored fringes. Not relevant effect of this type has been observed (even if the objective is not apochromatic).

Lateral chromatic

This defect is also known as *chromatic difference of magnification*. This aberration can be seen by comparing the color and the shape of hole at different distance from the center and observing colored fringes surrounding the image.

In this case, we have observed that even if all three main colors are brought to identical focal plane, the point images of details near the periphery of the field of view, have a difference in size of 1-2 μm.

To this effect, a green interferential filter has been put in the illumination system (550 nm).[15]

[15]Being the information stored in the emulsion, essentially a difference in the intensity of the light, the presence of a bandpass filter doesn't compromise the functionality. In fact the camera is monochromatic too.

6.3.3 Achromatic aberrations

Spherical

For a lens afflicted by spherical aberration, the diffraction image of a point source extends above and below the intermediate image plane into a three-dimensional patterns that expands and spreads out asymmetrically from the center along the optical axis. [16]

The choice to use a diffuser is due also to minimize residuals of spherical which have not been observed anymore.

Coma

Comatic aberrations are similar to spherical aberration, but they are mainly encounters with off-axis light fluxes and are most severe when the microscope is out of alignment; when coma occurs the image of a point (at the border of the field of view) is focused at sequentially differing heights producing a series of asymmetrical spot shapes of increasing size that result in a comet-like[17] shape to the diffraction pattern.

If coma appears at the center of the field, it means that same optical element is not aligned.

Also in this case, the effect has not been observed.

Astigmatism

The astigmatism is manifested by the off-axis image of a point appearing as a line or ellipse instead of a point. Moving the objective above and below the plane of the circle of least confusion, respectively a tangential or sagittal ellipse (or line) is in focus. In a perfectly centered system, this effect should be symmetric respect to the axis.[18]

We have observed an elongation of the diffraction pattern only in one side of the field, but its entity is very low (above 1 μm), and should not affect the measurements.

[16] The diffraction pattern must be longitudinally symmetric in particular the first two diffraction rings around the center of the image. Moreover, in presence of dramatic spherical aberration it is not a simple matter to determine which is the level that produces the best focus and the depth of field increases.

[17] Hence, the term coma.

[18] If present in the center, some elements are misaligned.

As summary, the objective quality has been tested and is suitable to the requirements. The objective can be considered *diffraction limited*.

Critical parameter in emulsion scanning are the depth of field (DOV=) and the resolution (R); once every causes of aberrations has been corrected or limited, it remains the limit imposed by diffraction and hence by the numerical aperture of objective and condenser. The theoretical values are:

$$\mathrm{DOV}_{th} = 1.6 \quad \mu\mathrm{m} \qquad R_{th} = 0.46 \quad \mu\mathrm{m}$$

but, since the image in the sensor of the camera is then digitized and processed, these values can increase. In particular the operation of convolution filter and threshold, during the acquisition, can give a final depth of field of:

$$\mathrm{DOV} \lesssim 3 \quad \mu\mathrm{m}$$

6.3.4 Condenser and diffuse light inside the optical tube

About the condenser, it has just been said that the presence of the diffuser and the green filter gives advantages, in term of correction of spherical and residual of chromatic.

By means of the auxiliary telescope is it possible to observe in the inner surface of the optical tube, the series of mechanical component from the rear focal plane of the objective to the sensor. Two sections were reflecting a little fraction of the light inside the tube;[19] so, the internal tube has been covered with a black absorbing foil.

6.4 Evaluation of the magnification error

The calibration of the system has been obtained by using same the 10μm grid pattern used for the evaluation of the field curvature. The measure has been made with the object in the best focal plane.

Because of the depth of field, points out-of-axis can be see under different angles, which cause different lateral magnifications; so, in the case of

[19] The reflected light rays can superimpose to the image and therefore decrease the contrast.

emulsion, the uncertainty in the longitudinal position of the grains inside the depth of field, produces also an error along the radial coordinate.

In our system, considering a grain at the margin of the field of view in a corner of the sensor. Since the distance from the center is FOV/$sqrt2 = 172$ μm and the objective focal length is $f_{obj} = 4$ mm, it is imaged under an angle which is $\alpha = \arctan(172/4000) \simeq 2.5$ degrees. If the longitudinal uncertaintly is DOV/2$\simeq$1.5 μm, the lateral magnification error is $1.5 \tan\alpha = 0.06$ μm can be considered negligible.

6.5 The alignment of the optical axis

A centering procedure is necessary in order avoid aberrations and systematics due to misalignments in the optical axis; especially in this case where the mechanical structure is composed by many components (stand, arm, light attachment, stages, ...).

By the means of the auxiliary telescope and viewing down the tube, the objective has been first centered; a frosted glass was used as diffuser just below the front lens of the objective and the visible circle of light (which is how appears the rear focal plane of the objective) was centered respect to the attachment of the tube. An error of ≈ 0.2 mm has been measured, but it's compatible with mechanical tolerances.

After removing objective, condenser and diffuser, the light source was centered and then, (once mounted) the condenser by moving the image of the light source with the condensers centering screws.

After the alignments, the parallelism of the following surfaces. were checked with an auto-collimating telescope:[20]

- upper and lower mount of the camera adapter;
- upper and lower surface of the trinocular tube;
- the upper surface of the arm;
- the objective mounting surface;

[20] An auto-collimating telescope has a reference metallic surface strictly perpendicular to its axis. By putting the telescope on one side and a mirror on the other side of the element to be checked, it is possible to measure the parallelism within $\lambda/4$.

- the surface of the stage.

The differences in parallelism are within 5' ($\simeq$ 1.5 mrad).

Chapter 7

Preliminary results

In this chapter the preliminary results on the prototype realized in Bologna Laboratory will be presented. The aim of the first measurements is to check the hardware set-up and to tune the software parameters on OPERA emulsions.

For this purpose, some emulsion sheets exposed at CERN were used.

The beam test data allowed also to make a preliminary analysis on angular resolution of the Bologna microscope.

7.1 The test beam setup

A test beam with emulsions was performed at CERN in July 2002 with several purposes; in particular for the microscopes tuning, for tests of refresh and for estimation of angular resolution.

A sample of 28 Fuji plates[1] were assembled manually together with 28 low quality emulsion plates, released for mechanical test, and with lead in a standard OPERA brick. Before the exposure, out of the sample, 8 plates were refreshed at 28 deg and 82% relative humidity.

The brick was exposed to a 7 GeV/c π^- beam, at 6 different angles versus the beam direction, namely 1, 7, 13, 19, 25 and 31 deg, by rotating the brick as shown in Fig. 7.1.

The beam exposure conditions were tuned and managed to spread in an almost uniform way the beam over the whole brick area, with a comfortable

[1] Batch E10-055 and E10-044 delivered at CERN at that time.

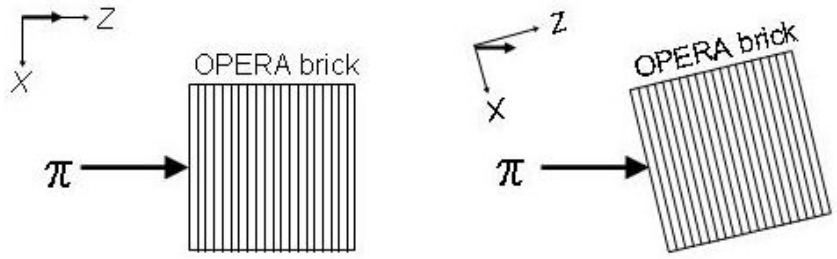

Figure 7.1: The brick has been exposed to a 7 GeV/c π-beam at different angles by rotating the brick respect to the beam axis.

beam flux, such that a nominal integrated flux could be collected in a few minutes exposure.

The number of triggers collected by a pair of scintillators 10x10 cm^2 mounted on the brick for monitor purpose, was about 75000 for each angle.

The choice to not have a peak at exactly 0 degree, is due to make easier to separate the beam tracks peak by fake tracks reconstructed during the readout.

The plates were labelled after exposure: 1 to 28 are 'good', 29 to 56 are 'mechanical' (upstream to downstream in the beam direction). Plates 3,6,9,12 were refreshed for 65 h; 17,20,23,26 for 41 h. A 2 cm grid of fiducial marks was printed on the plates.

Preliminary checks were made at CERN using a 45x dry objective: development was good, surfaces rarely presented small drops; the plate thickness was found a bit less than 40 micron on both sides. The density of beam tracks was rather uniform (indeed of the order of 10^3 cm^{-2} at 1 deg).

The refreshing procedure induced a visible reduction of the background (tracks outside the beam direction, in particular "vertical" tracks). No effect was noticed for the beam tracks, and the sensitivity (granularity) was found, at least by eye, unaffected by refreshing (as expected).

Then, the plate was shared within the collaboration laboratory. In particular the plates 24,25,26 (refreshed) and 27 were taken by Bologna.

7.2 DAQ software

The acquisition software has been developed in C and C++ under Windows 2000 operating system. The choice was due to the fact that most producers of hardware for data acquisition and automation support only Windows operating systems.

Some kinds of application were used in the initial trials:

- applications, developed for this thesis, to interface the motion board, the camera and the light source; these programs have been used to perform checks, for example measurements of the settling time of the stage, of the frame rate of the camera, of the displacement repeatability, and so on;
- test and configuration programs for small area acquisition (limited to one view);
- the SySal acquisition program;
- simple off-line applications for the reconstruction of the tracks.

7.3 The SySal acquisition software

The SySal system has been developed by the Salerno group for the CHORUS experiment and the re-arrangement for OPERA is in progress.

It has been written in MS Visual C++ with use of dlls, COM and ActiveX technologies. It includes many tools for acquisition, reconstruction and analysis.

The acquisition application has an object-oriented structure; the main code acts as framework for several modules, as shown in Fig. 7.2.

Each of these modules corresponds to a class interfaced and stored as an DLL file:

Genesis4 is the task which realizes the interface with the frame-grabber card and take care of the image processing steps (convolution, threshold, cluster finding,...).

FlexStage is interfaced with the microscope stage controller (FlexMotion). The FlexStage class also provides the operator with a tool to move the microscope in semi-automatic mode.

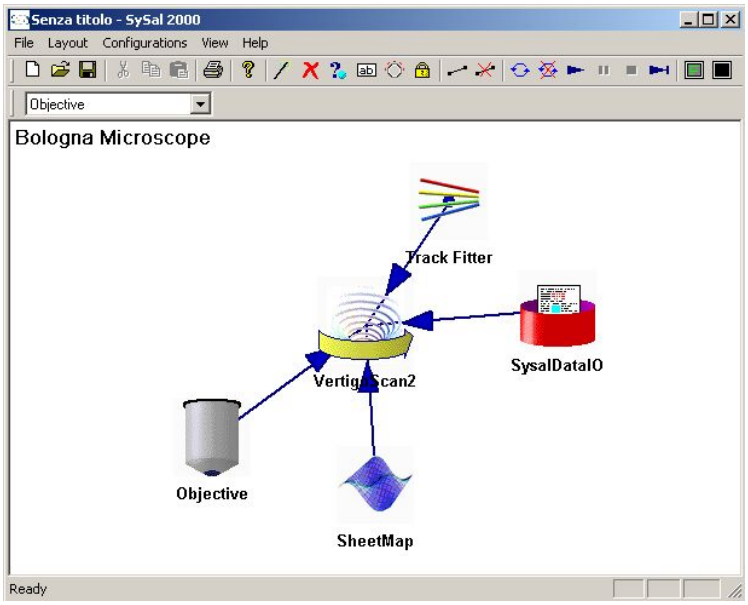

Figure 7.2: The SySal application windows. The system is divided in several modules.

Objective is the module where the parameters which depend on the particular choice of objective are stored.

SheetMap transforms coordinates and vectors from the current stage reference frame to the fiducial markers reference system.

SmartTracker is an object responsible for recognizing the particle tracks in a list of grains coming from several images.

TrackFitter contains all the procedures needed to correct the local distortion of the emulsion, to discard fake tracks on the basis of a quality analysis and to improve the reconstruction of the good ones.

SysalDataIO is used to read and write data to files.

VertigoScan is the scanning steering module which uses all other objects to perform the scanning.

The logical scheme of DAQ process, as described in Chap. 5, is the following:

- execute an optical tomography of the whole thickness of the emulsion;
- recognize the grains in emulsion image;
- detect the local alignments of the grains and reconstruct the particle tracks in the volume;
- correct the distortion of the tracks and extract their global geometrical parameters;
- store the tracks for further analysis.

After the acquisition, track segments in both sides of emulsion sheet are off-line linked across the plastic base to obtain the *base track*.

7.4 Quality tests of the scanning system

The quality of the measurement results depends on many critical parameters, in particular about processing and tracking, as explained in Chap 5. Also the illumination intensity is crucial: the number of clusters in each layer can decrease as the light increase.

The tuning of image processing and tracking is a very large time-consuming process, and in our case it has needed several months before start large area scanning; much of this work has been made by searching manually tracks in both side of emulsion sheet, changing some parameters and then checking the results at various level, from the grain density distribution, to the reconstructed tracks analysis.

In the following, some checks on basic operations performed on the system are described.

7.4.1 Mechanical tests

The mechanical motion in the measurement procedure, consists in a cyclic displacement of the z-axis of about 50 μm in order to grab images of the emulsion at different layers, followed by the change of the view (i.e. an horizontal displacement of an amount equal to the view size). During the change of view, the vertical stage return to the initial position.

Obviously, before starting the grab in the new view, the stage must be perfectly steady.

Tests have been performed to measure the displacement and settling time, under different conditions of velocity and acceleration. The aim is to fix the best motion parameters to minimize the total time of acquisition.

A typical plot for evaluation of displacement and settling time, is shown in Fig. 7.3. The stage moves to the final position and oscillates; the acquisition cannot start until oscillation width is within a tolerable value.

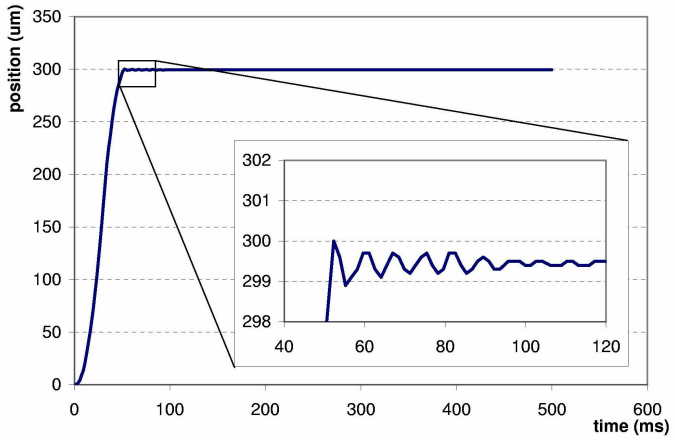

Figure 7.3: An example of evaluation of displacement and settling time.

The measurements of the displacement and settling time, within a tolerance of 0.15 μm, for both x and y axis is shown in Fig. 7.4; it is possible to change the field of view along the x axis in less than 60 ms. The difference between the two axis is due to the fact that the x axis is mechanically mounted on the y axis which inertia is, consequently, higher.

In Fig. 7.5 the tests of displacement and settling times in the best condition for both axis, are shown.

Other mechanical tests on the positioning precision has been performed, showing no particular deviations from the expected manufacturer performance.

7.4.2 Illumination checks

An histogram of the gray level distribution of the typical image is shown in Fig. 7.6. Note that the focused grains are in the range 50÷130, as shown

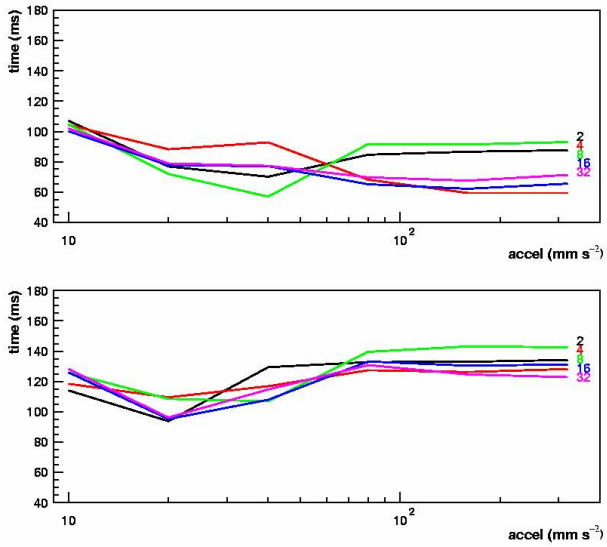

Figure 7.4: Measurements of the displacement and settling time (ms) of both x and y axis, versus the acceleration (mm/s^2) of the horizontal stage for different values of velocity from 2 to 32 mm/s.

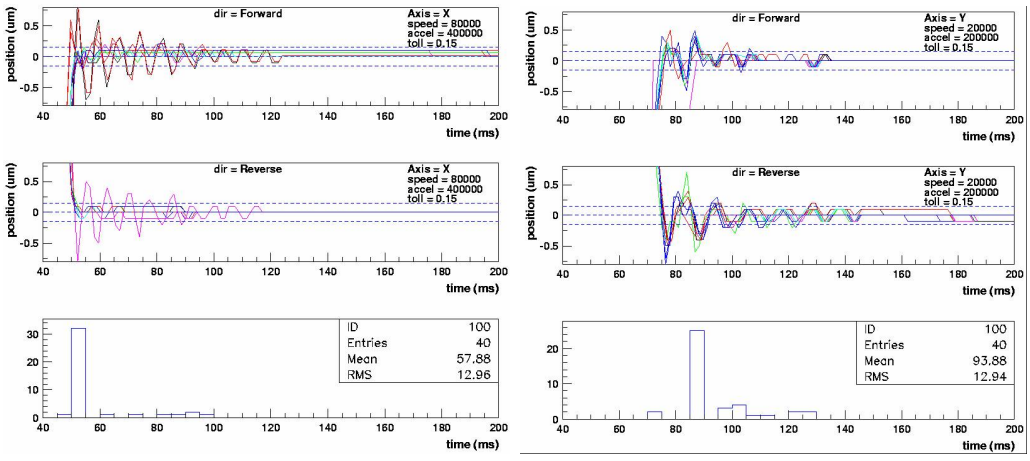

Figure 7.5: Tests of displacement and settling time for the x and y axis in the best conditions of velocity and acceleration.

In Fig. 7.7b and 7.7c which are the result of processing of the image in Fig. 7.7a, applying different cuts on gray levels.

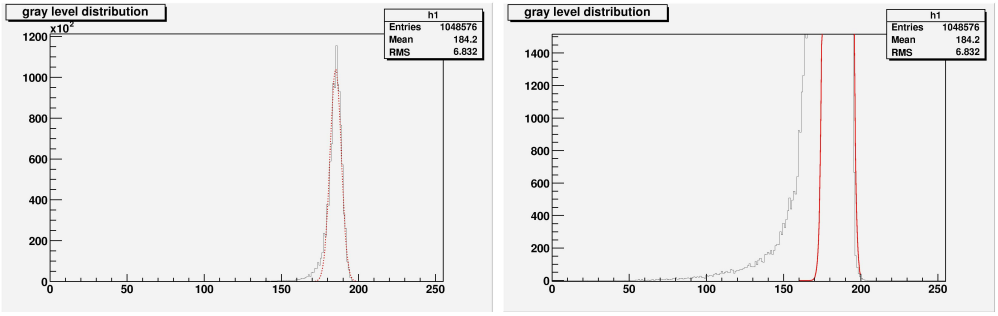

Figure 7.6: Gray level distribution; the grains pixels are in the left tale of the histogram. Focused grains are in the range 50÷130as shown in Fig. 7.7.

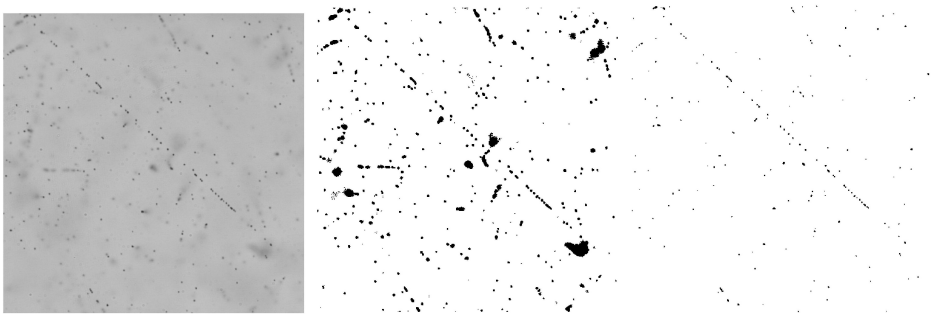

(a) (b) (c)

Figure 7.7: Effect of the threshold at different level: (a) unprocessed image; (b) threshold at 170, unfocused grains still remain; (c) threshold at 130, there are only focused grains.

A distribution of the number of cluster versus the light intensity (indicated as lamp temperature) is shown in Fig. 7.8.

The best value of the lamp adjustment has been choosen at about 3050 K, before the ramp toward image saturation.

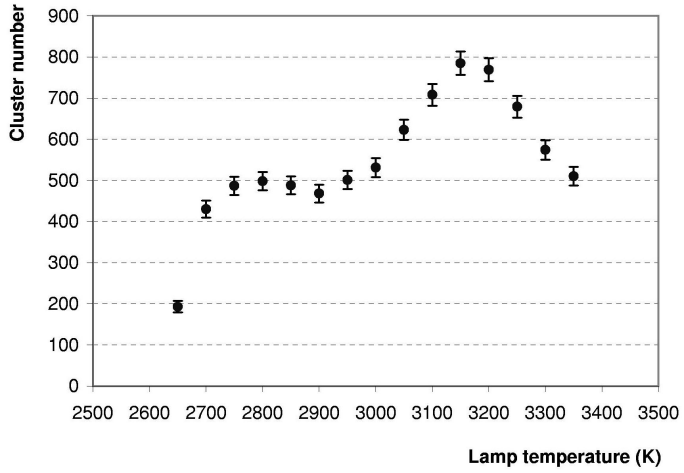

Figure 7.8: Number of clusters versus the light intensity.

7.4.3 Acquisition uniformity

Once segments (micro-tracks)[2] are reconstructed in the top and bottom sides of a sheet, the distribution of the clusters recognized to form these segments were examined to ensure the spatial uniformity of the acquisition. The cluster distributions as function of the acquired layer for the top and bottom sides, are reported in Fig. 7.9 [3] and Fig. 7.10 shows the x-y distributions of clusters of the micro-tracks in the field of view of the camera.

As the tracks recognition starts finding the grain alignments, separately on top and bottom sides, about 60 micro-track per view are obtained (i.e. $\sim$1000/mm^2).

Obviously, only a small fraction of these micro-tracks is belonging to true beam tracks, because of physical background, and bad associations of fog clusters, and so on.

The micro-track geometry is given by the DAQ application in the form:

$$\begin{cases} z = s_x x + q_x \\ z = s_y y + q_y \end{cases}$$

[2]Segments or micro-tracks refer to the tracks reconstructed in the top or bottom side of the emulsion plate. Linked tracks or base tracks refer to the track obtained by linking two micro-tracks across the plastic base.

[3]Note that the lack of grains in the middle of the emulsion due to the assembling of the films is clearly visible (see Fig.4.4).

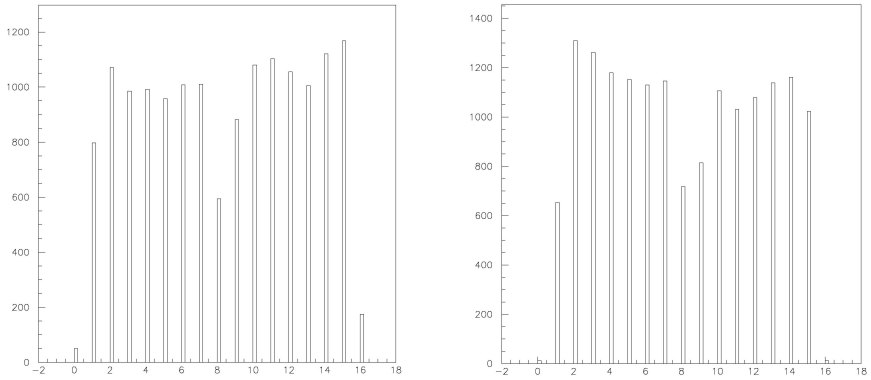

(top) (bottom)

Figure 7.9: Distribution of clusters used to reconstruct micro-tracks in the top and the bottom side of emulsion sheet, as function of the acquisition layer. Layers are interspaced of about 2 μm.

where the point (q_x,q_y) is the intercept between the track and the emulsion-base surface and (s_x,s_y) are the slopes.

The scatter plot of the slopes of micro-tracks is shown in Fig. 7.11. The scanned area is about 1.5 cm^2. Already at this level of analysis, higher densities in the beam coordinates are clearly visible.

7.4.4 Track reconstruction

Once micro-tracks have been found on both sides of the emulsion and their coordinates have been corrected for distortions and shrinkage, the on-line process stops. The next step is to try to connect micro-tracks across the plastic base to reconstruct a linked-track.

The track linking is performed by projecting a micro-track on the other side of the plastic base and searching for a micro-track within certain slope and position tolerances. The linked track is then reconstructed only with the intercepts of the microtracks with the base, as swhon in Fig. 7.12.

As example, Fig. 7.13 shows a micro-track with its points (a) and the linked track (b). The scatter plot of the slopes of linked track during a 1.5 cm^2 acquisition, is shown in Fig. 7.14, while Fig. 7.15 reports mean and width of beam peak tracks. The mean value of each peak corresponds

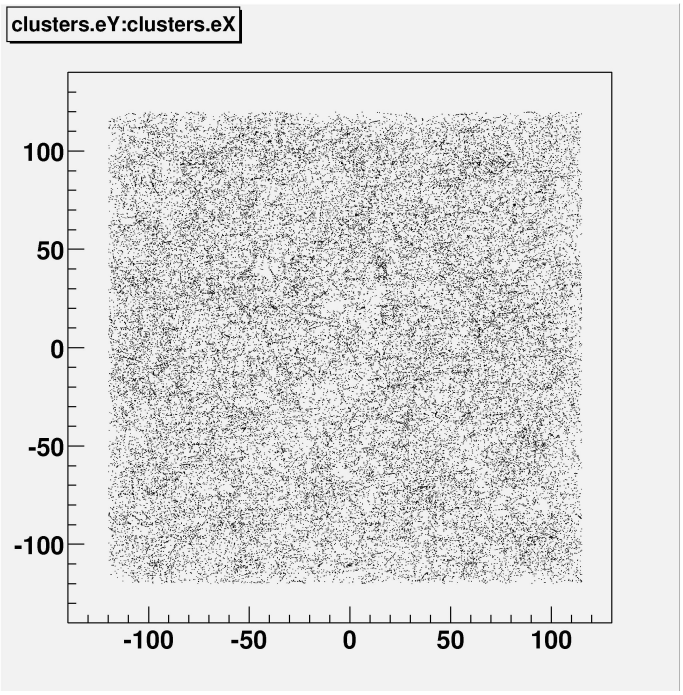

Figure 7.10: Distribution of clusters belonging to micro-tracks, in the field of view of the camera (240×240 μm^2).

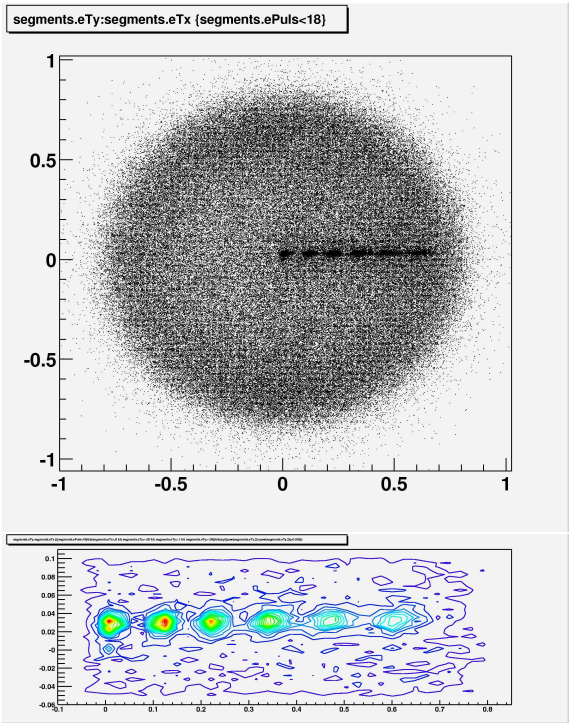

Figure 7.11: Scatter and contour plots of the slopes of micro-tracks (top side). The peaks corresponding to the beam are clearly visible.

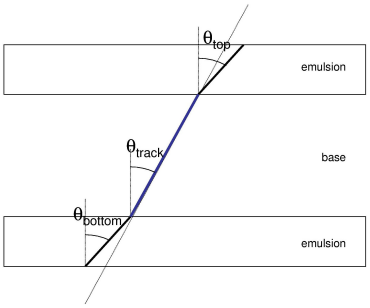

Figure 7.12: Micro-tracks connected through the base. The base track is evaluated from the intercept between micro-tracks and base.

very well to the expected value of the beam center angles; the increase of the standard deviations at higher angles is also expected as spreads due to multiple coulomb scattering.

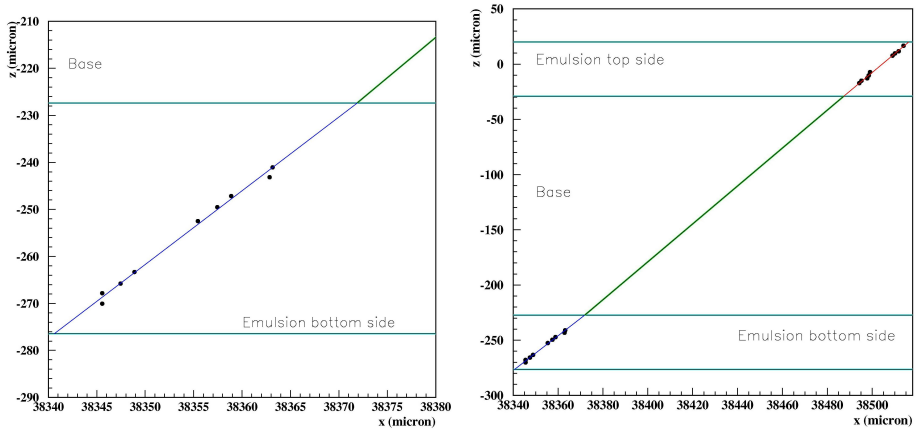

(a) (b)

Figure 7.13: Example of acquisition and linking of two micro-tracks in the OPERA emulsion plate. (a) details of acquired grains in the bottom side; (b) the entire event, showing the reconstructed base track.

To check the quality of the fits obtained and to ensure that systematics effects are negligible, plots of all the parameters of micro-tracks are carefully checked.

For example, in Fig. 7.16 the difference of the slopes of the micro-tracks which have been connected to form a linked track, are reported. Even if the angular spread between top and bottom slopes is large, the error of the intercept in a ~ 40 μm side, is of the order of $40\sigma/\sqrt{2} \simeq 1$ μm in the worst case; consequently, since the base thickness is 200 μm the uncertainty of the slope and position of linked track is lower than 5 mrad.

In Fig. 7.17 the number of points of linked tracks is shown ("pulse height"). The Fig. 7.18 shows the distribution of standard deviation of the grains from the reconstructed track of the beam peaks.

These are only the preliminary results of the first (small) area of emulsion, scanned with the Bologna automatic system. The next steps will be obviously to link more plates each other, to obtain the slope of track on the entire

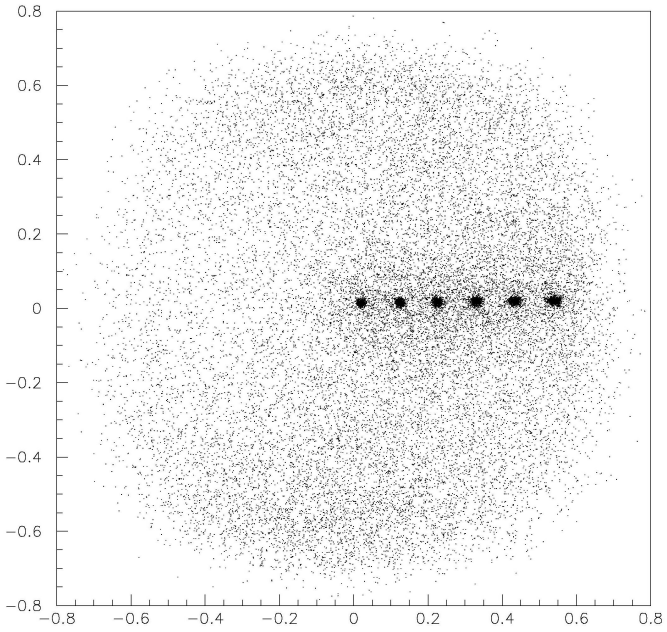

Figure 7.14: Scatter plot of the slopes of linked tracks.

measured path and to evaluate the efficiency of the tracks recognition in the plates.

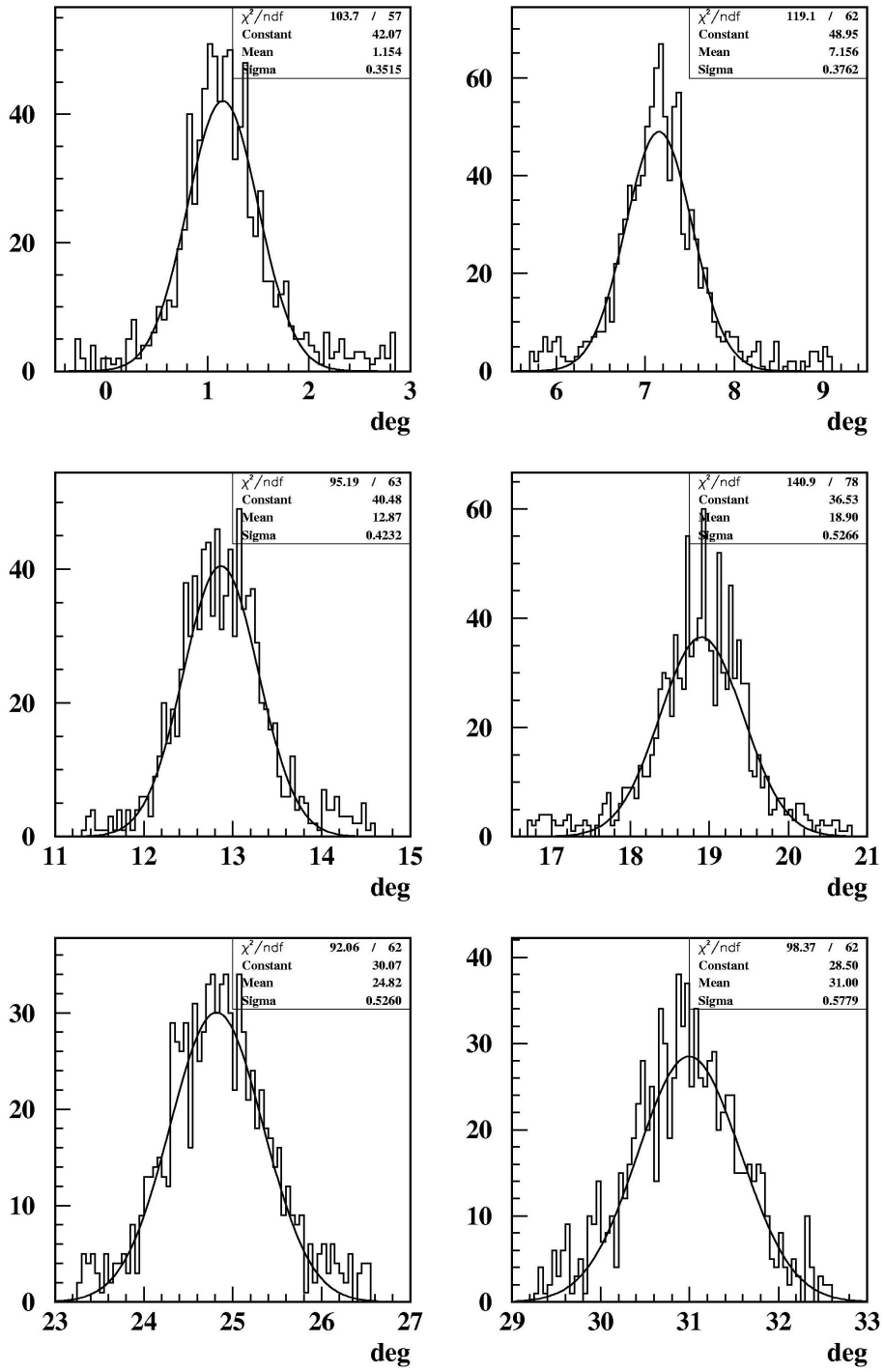

Figure 7.15: Distribution of the angles of linked tracks around the peaks of the test beam.

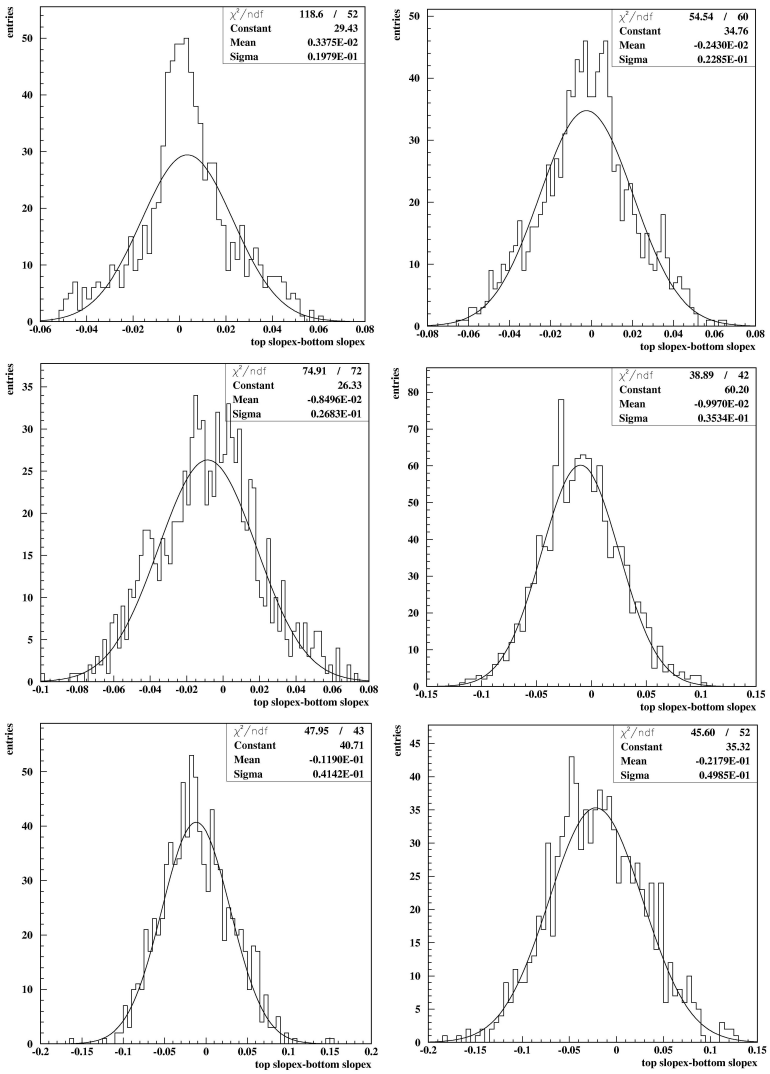

Figure 7.16: Differences top-bottom

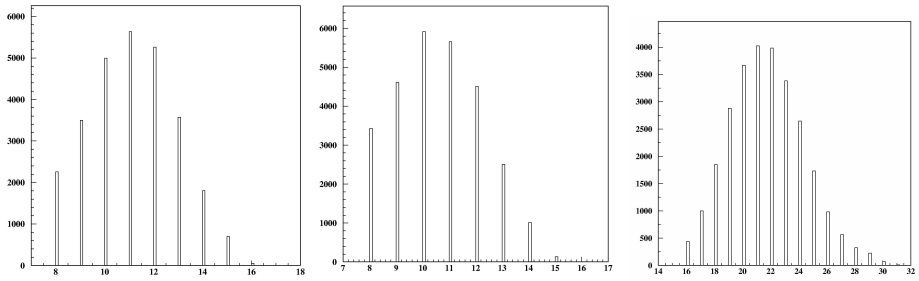

(a) (b) (c)

Figure 7.17: Pulse height distributions (i.e. the number of grains per track), (a) top side, (b) bottom side, (c) linked track.

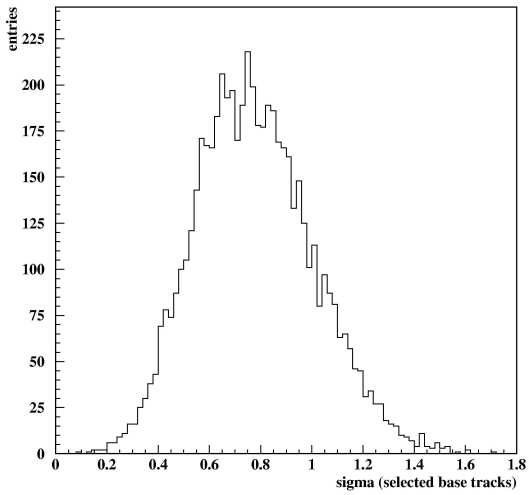

Figure 7.18: Standard deviations of the grain distance from the fitted track.

Conclusions

The OPERA experiment will extensively use nuclear emulsion sheets as high precision tracker detectors, to search for the ν_τ appearance in the ν_μ CNGS beam.

In order to manage the readout of large amount of emulsions, an R&D project is in progress within the collaboration to realize automatic scanning systems with the precision and scanning speed requested.

In this framework, a prototype of an automatic scanning system has been realized and installed in the Bologna Laboratory.

Many efforts have been made to ensure the accuracy of the hardware set-up and of the tuning of the optical system.

Several tests were made to determine the performance and accuracy of this automatic system. In particular several emulsion sheets were exposed to a 7 GeV π^- beam at the CERN SPS.

The results of the test are encouraging, and demonstrate that the main requirements have been obtained.

Bibliography

[1] W. Pauli, Fünf Arbeiten zum Ausschlieβungsprinzip und zum Neutrino, Texte zur Forschung Vol. 27, Wissenschaftliche Buchgesell Darmstadt 1977, W. Pauli, On the earlier and more recent history of neutrino (1957) in Neutrino Physics, ed. K. Winter, Cambridge University Press,1991

[2] F. Reines and C.L. Cowan, Nature 178 (1956) 446.

[3] G. Danby et al., Phys. Rew. Lett. 9 (1962) 36.

[4] S.L Glashow, Nucl phys. 22 (1961) 597 ; S. Weinberg, Phys. Rev. Lett. 19 (1967) 1264 ; A. Salam, Proc. of the 8^{th} Nobel Symposium on *Elementary particle theory, relativistic groups and analyticity* edited by N. Svartholm (1969)

[5] Particle Data Group, D.E. Groom et al., Eur. Phys. J. C15 (2000) 1.

[6] S. Sarkar, Rep. Prog. Phys.59 (1996) 1493; hep-ph/9602260.

[7] B. Pontecorvo, Zh. Eksp. Teor. Fiz. 33 (1957) 549; Zh. Eksp. Teor. Fiz. 34 (1958) 247; Zh. Eksp. Teor. Fiz. 53 (1967) 1717.

[8] G. Giacomelli et al., Atmospheric neutrino oscillations, Proc. of the 6 th School on Non Accelerator Astroparticle Physics, Trieste, Italy, 2001.

[9] D. Vignaud, Solar and supernovae neutrinos, Proc. of the 6 th School on Non Accelerator Astroparticle Physics, Trieste, Italy, 2001.

[10] The LEP Coll. (Aleph, Delphi, L3, OPAL), A combination of preliminary electroweak measurements and constraints on the Standard Model, CERN- EP/2000-153, (2000).

[11] Z. Maki, M. Nakagawa and S. Sakata, Progr. Theor. Phys. 28 (1962) 870.

[12] R.N. Mohapatra and G. Senjanovic, Phys. Rev. Lett. 44 (1980) 912.

[13] L. Wolfenstein, Phys Rev. D17 (1978) 2369; Phys. Rev. D20 (1979) 2634.

[14] S.P Mikheyev and A.Y. Smirnov, Sov. j. Nucl. Phys. 42 (1985) 913.

[15] Lobashev, V.M., Talk given at the *XIX Intern. Conf. on Neutrino Phys. and Astrophys. "Neutrino 2000"*, Sudbury, Canada, June 16 – 21, 2000. Tranparencies at http://nu2000.sno.laurentian.ca/

[16] Weinheimer, C., Talk given at *Neutrino 2000*, see ref.[15].

[17] Roney, J.M., Talk given at *Neutrino 2000*, see ref.[15].

[18] S.H. Ahn, et al., Phys. Lett. B 511, 178 (2001); J.E. Hill, et al.,hepex/ 0110034; C.K. Jung in Proceedings of the Lepton-Photon 2001 Conf.; (http://www.lp01.infn.it/proceedings/jung.pdf) .

[19] See MINOS web site at: http://www-numi.fnal.gov/forscientists.html and http://www-numi.fnal.gov/blessed/index.html

[20] A. Aguilar, et al., Phys. Rev. D 64, 112007 (2001).

[21] E.D. Church, et al.,hep-ex/0203023, March,2002.

[22] Soudan 2 Coll., W.W.M. Allison et al., *Phys. Lett.* B **391**, 491 (1997); *Phys. Lett.* B **449**, 137 (1999); W. Anthony Mann, hep-ex/0007031.

[23] MACRO Coll., S. Ahlen et al., *Phys. Lett.* B **357**, 481 (1995). M. Ambrosio et al., *Phys. Lett.* B **434**, 451 (1998); *Phys. Lett.* B **478**, 5 (2000).

[24] SuperKamiokande Coll., Y.Fukuda et al., *Phys. Rev. Lett.* **81**, 1562 (1998); *Phys. Lett.* B **433**, 9 (1998); *Phys. Rev. Lett.* **85**, 3999 (2000); *Nucl. Phys.* B *Proc. Suppl.* **91**, 127 (2001); T. Toshito, hep-ex/0105023 (2001).

[25] G.J. Feldman and R.D. Cousins, *Phys. Rev.* D **57**, 3873 (1998).

[26] G. Acquistapace et al., CERN 98-02, /AE-98/05, 19 May 1998.

[27] A. Ereditato et al., ICARUS-TIM-98/13, OPERA 980722-21.

[28] R. Bailey et al., CERN-SL/99-034 (DI); INFN/AE-99/05.

[29] H. Sobel (Super-Kamiokande Coll.), to appear on the Proc. of the XIX Int. Conf. on Neutrino Physics and Astrophysics, Sudbury, 2000.

[30] C. Walter (Super-Kamiokande Coll.), Proc. of the Int. Conf. HEP 99, Tampere, 1999; M. Nakahata, Proc. of the VI Int. Workshop on Topics in Astroparticle and Underground Physics, Paris, 1999.

[31] E. Ables et al., Fermilab Proposal P-875 (1995); NuMI-L-337 (1998); NuMI-L-375 (1998); htp://www.hep.anl.gov./NDK/Hyprtext/numi.html.

[32] C.F. Powell, P.H. Fowler and D.H. Perkins, The study of elementary particles by the photograohic method, Pergamon, New York, 1959.

[33] W.H. Barkas, Nuclear Research Emulsions, Academic Press, New York and London, 1963.

[34] A.J. Apostolakis and J.V.Major, Brit. J. Appl. Phys. 8 (1957) 9.

[35] B. Rossi, High energy particles, Prentice Hall, New Jersey (1952).

[36] S. Aoki et al. Nucl. Instr. And Meth. B51, (1990) 446.

[37] G. Rosa et al. Nucl. Instr. And Meth. A394, (1997) 357-367.

[38] G. Romano Emulsioni Nucleari Lab. Di Fisica II A.A. 1976-77, Ist. Di Fisica "G. Marconi", Univ. Roma.

[39] A. Beiser Nuclear Emulsion Technique Rev. Mod. Phys. 24, (1952) 273.

[40] C.F. Powell, P.H. Fowler and D. H. Perkins The Study of Elementary Particles by the Photographic Method Pergamon Press, New York 1959.

[41] W.H. Barkas Nuclear Research Emulsions, vol.I and II Academic Press, New York 1963

[42] Tsai-Chu Determination of Distortion Vector in Nuclear Emulsion il Nuovo Cimento, Vol. 5.5, (1957)1128.